Spring 1-1-2018

Effects of Active and Passive Spreading on Mixing and Reaction During Groundwater Remediation by Engineered Injection and Extraction

Lauren Reising Jane Reising
University of Colorado at Boulder, ljreising@gmail.com

Effects of Active and Passive Spreading on Mixing and Reaction During Groundwater Remediation by Engineered Injection and Extraction

by

Lauren Jane Reising

B.A., The University of California, Berkeley, 2008

M.S., The University of Colorado, Boulder, 2015

A thesis submitted to the

Faculty of the Graduate School of the

University of Colorado in partial fulfillment

of the requirements for the degree of

Doctor of Philosophy

Department of Civil, Environmental, and Architectural Engineering

2018

This thesis entitled:
Effects of Active and Passive Spreading on Mixing and Reaction During Groundwater
Remediation by Engineered Injection and Extraction
written by Lauren Jane Reising
has been approved for the Department of Civil, Environmental, and Architectural Engineering

_____

Prof. Roseanna M. Neupauer

_____

Prof. John P. Crimaldi

_____

Prof. David C. Mays

Date _____

The final copy of this thesis has been examined by the signatories, and we find that both the
content and the form meet acceptable presentation standards of scholarly work in the above
mentioned discipline.

Reising, Lauren Jane (Ph.D., Civil Engineering)

Effects of Active and Passive Spreading on Mixing and Reaction During Groundwater Remediation
    by Engineered Injection and Extraction

Thesis directed by Prof. Roseanna M. Neupauer

During in situ groundwater remediation, a chemical or biological amendment is introduced into the aquifer to degrade the groundwater contaminant. In this type of remediation, mixing of the amendment and the contaminated groundwater, through molecular diffusion and pore-scale dispersion, is necessary for reaction to occur. Since the length scale of dispersion is small compared to the size of the contaminant plume, reactions are limited to a relatively narrow region where the amendment and contaminant are close enough to mix. Spreading, defined as the reconfiguration of the plume shape due to spatially-varying velocity fields, increases the size of the region where reaction occurs and increases concentration gradients, both of which can lead to enhanced mixing and reaction. Spreading can occur passively by heterogeneity of hydraulic conductivity or actively by engineered injection and extraction (EIE), in which clean water is injected or extracted at an array of wells surrounding the contaminant plume. Several studies have shown that active spreading by EIE enhances contaminant degradation in homogeneous porous media compared to remediation without EIE. Furthermore, studies have also shown that combining EIE with passive spreading by heterogeneity can lead to even more degradation compared to EIE alone. In this study, we investigate the relationship between passive and active spreading to better understand their combined impact on mixing and reaction during EIE. Using various combinations of heterogeneity patterns (e.g., high and low hydraulic conductivity inclusions) and simple injection and extraction flow fields typical to EIE, we determine how the particular spreading of the amendment and contaminant plume under each heterogeneity/flow field combination controls the amount of mixing and reaction enhancement. We find that the injection and extraction flow fields can be designed to complement the topological features generated from specific heterogeneity structures,

thereby increasing the amount of mixing and reaction enhancement. Since the subsurface is inherently heterogeneous, insights gained from this research will provide crucial information for the optimal design of EIE systems in the field.

Acknowledgements

I would like to thank Roseanna Neupauer for her guidance over the past three years. She has always made myself and my research a priority. In the world of academia, where everyone is extremely busy, this is not a given and I am forever thankful to have such a dedicated mentor. She inspires me to be a better researcher and a better writer.

I would like to thank David Mays, John Crimaldi and Eric Roth for their advice, support, and meaningful contributions to this research. Their feedback in our monthly research meetings, especially in the beginning stages of my research, was crucial. Finally, I would like to thank Balaji Rajagopalan and Angela Bielefeldt for serving on my committee and for their valuable feedback on this research.

Contents

Tables

Table

Figures

Figure

Chapter 1

Introduction

1.1   Problem Statement and Motivation

Many communities around the world rely heavily on groundwater as a freshwater resource for drinking water and irrigation. Unfortunately, groundwater is often contaminated by chemicals from industry and agriculture and must be remediated before it is safe for use by humans. In the U.S., the cost to remediate all contaminated groundwater sites was recently estimated to be between $110 billion to $127 billion (National Research Council, 2013). Such a high cost indicates the vital need to develop effective groundwater remediation methods that are energy and cost efficient. One such groundwater remediation method is to treat the contaminated water in-situ by introducing a chemical or biological amendment into the aquifer to react with and degrade the contaminant. Treating the contaminated groundwater in-situ reduces the energy and cost required by conventional "pump and treat" methods by eliminating the need for extracting the contaminant, transporting it to the treatment facility, treating it to regulatory standards, and reinjecting it back to the aquifer.

Substantial progress has been made in the past 20 years in the development of technologies for remediation of contaminated groundwater; however, significant challenges remain. A remaining challenge of in-situ remediation is achieving high levels of mixing between the amendment and the contaminant, especially given certain site-specific characteristics. For example, aquifer heterogeneity impacts the transport of the contaminant and the injected treatment chemical and often limits the contact of these reactants, which can lead to poor performance during in situ remediation,

especially aquifers with zones of low permeability (Siegrist et al., 2012). In porous media, mixing, through molecular diffusion and pore-scale dispersion, is necessary for reaction (Kitanidis, 1994; Cirpka, 2002). Since the length scale of both pore-scale dispersion and molecular diffusion is small compared to the size of the contaminant plume, reactions are limited to a narrow region where the amendment and contaminant are close enough to mix. Therefore, mixing processes represent a limiting factor in the amount of possible contaminant degradation.

One process shown to enhance mixing in porous media is spreading, which is the reconfiguration of the plume due to spatially-varying velocity (Le Borgne et al., 2010). On the one hand, spreading can occur passively due to the variability in the hydraulic conductivity (and consequently, in the velocity field) of the aquifer (Kapoor and Kitanidis, 1996, 1998; Le Borgne et al., 2010, 2013; de Anna et al., 2014; Le Borgne et al., 2015). Active spreading, on the other hand, is created by spatial and temporal variations in groundwater flow forcings, such as time-varying point injections or extractions of water, that create spatially- and temporally-varying velocity fields (Tél et al., 2000; Stremler et al., 2004; Sposito, 2006; Bagtzoglou and Oates, 2007; Zhang et al., 2009; Trefry et al., 2012; Mays and Neupauer, 2012; Piscopo et al., 2013).

Many studies have shown that both passive and active spreading enhance mixing and reaction in porous media. However, studies investigating the local flow mechanisms of active and passive spreading that lead to increased mixing and reaction are limited. Such an understanding would make it possible to develop strategies to assist with optimizing EIE systems in the field. Therefore, the goal of this study is two-fold. First, identify local behaviors present in a variety of active spreading and passive spreading flows that enhance mixing and reaction in porous media. Second, identify passive and active spreading combinations that lead to additional mixing and reaction enhancement and those that lead to less. Insights gained from this research will provide crucial information for the optimal design of EIE systems in the field.

1.2   Background

1.2.1   Spreading, Mixing and Reaction in Porous Media

The relationship between spreading, mixing and reaction plays an essential role in a range of processes in geophysical flows (e.g., Tél et al., 2005; Weiss and Provenzale, 2008; Bauer et al., 2009; Dentz et al., 2011; Mays and Neupauer, 2012; Fu et al., 2015; Hidalgo et al., 2015; Finn and Thiffeault, 2011). Subsequently, it has been researched extensively, especially in the field of fluid mechanics where it is commonly referred to as "mechanical mixing" or "stirring" (Ottino et al., 1979; Ranz, 1979; Ou and Ranz, 1983a,b; Ottino, 1989; Clifford et al., 1998; Clifford, 1999; Villermaux and Rehab, 2000; Meunier and Villermaux, 2010; Paster et al., 2015). For flows without porous media, the diffusive mass flux, which depends on the molecular diffusion coefficient and the concentration gradient, drives mixing. Spreading stretches the solute plume, increasing the area available for mixing and reaction. Additionally, stretching increases concentration gradients (Ou and Ranz, 1983a). Together these two mechanisms lead to enhanced mixing and reaction.

The same concepts described above can be applied to spreading in porous media, with one notable difference. During transport through porous media at the Darcy scale, the mass flux that drives mixing is controlled by pore-scale dispersion in addition to molecular diffusion. Pore-scale dispersion (also referred to as mechanical dispersion) is the result of velocity differences within the pores and path differences due to the tortuosity of the pore network. The dispersion tensor, $\mathbf{D}$, is given by

$$
\begin{aligned}
D_{xx} &= \alpha_L \frac{v_x^2}{|\mathbf{v}|} + \alpha_T \frac{v_y^2}{|\mathbf{v}|}, \\
D_{xy} &= D_{yx} = (\alpha_L - \alpha_T) \frac{v_x v_y}{|\mathbf{v}|}, \\
D_{yy} &= \alpha_L \frac{v_y^2}{|\mathbf{v}|} + \alpha_T \frac{v_x^2}{|\mathbf{v}|},
\end{aligned}
\tag{1.1}
$$

where $\mathbf{v} = (v_x, v_y)$ is the groundwater velocity vector and α_L and α_T are the longitudinal and horizontal transverse dispersivities, respectively. Since the effects of pore-scale dispersion are greater in the direction of flow than parallel to flow, $\alpha_L > \alpha_T$. Therefore, in addition to the mechanisms

already mentioned for spreading in flow with no porous media, the orientation of the plume boundary with the local velocity direction will also affect the amount of mixing and reaction enhancement in porous media.

1.2.2   The Effects of Active Spreading on Mixing and Reaction

Investigation of the use of active spreading in porous media to enhance mixing and reaction during in-situ remediation began with the pulsed dipole (Tél et al., 2000; Stremler et al., 2004; Sposito, 2006; Bagtzoglou and Oates, 2007; Zhang et al., 2009; Trefry et al., 2012). While numerical studies showed that the pulsed dipole active spreading method enhanced mixing and reaction, there were limitations to its applicability in the field, including assumptions about the timing and orientation of re-injection of fluid particles that were not physically realistic in groundwater applications (Mays and Neupauer, 2012).

Alternatively, Mays and Neupauer (2012) developed a method, called engineered injection and extraction (EIE), that produced active spreading, while, at the same time, overcoming the limitations of the previous studies. The method consists of injecting a chemical or biological amendment into the contaminated groundwater and then implementing a sequence of injections and extractions of clean water at an array of wells surrounding the contaminant plume to create unsteady flow fields that stretch the interface between the amendment and contaminated groundwater. Piscopo et al. (2013) showed that EIE leads to enhanced reaction during in-situ remediation compared to passive in-situ remediation for both homogeneous and heterogeneous aquifers.

However, there are very few studies investigating the relationship between the global mixing/reaction behavior and transport at local scales during active spreading. One such study, performed by Le Borgne et al. (2014), investigated the impact of reaction front deformation under radial flow (the most simple active spreading flow field). They developed an approach based on a lamellar representation of fluid mixing that provides a direct link between local fluid deformation, the distribution of concentration gradients, and the reaction rate. Using this approach, they show that the temporal evolution of the reaction rate is determined by the flow topology and the

distribution of local velocity gradients which leads to an increase in the reaction that is orders of magnitude larger than in uniform flow.

However, since Le Borgne et al. (2014) studied radial flow, in which the plume boundary is everywhere transverse to the local flow direction, the effect of spreading via the orientation of the plume boundary with the local flow direction was not considered. EIE operations manipulate the interface between the contaminant plume and the amendment plume so that the local orientation of contaminant plume boundary relative to the local flow direction varies spatially and temporally. Therefore, to understand the link between the global mixing/reaction behavior and local transport behavior in these systems, it is necessary to include the effect of spreading via the orientation of the plume boundary with the local flow direction.

1.2.3 Effects of Passive Spreading on Mixing and Reaction

Natural variability in the hydraulic conductivity of the subsurface results in passive spreading. As a solute plume is transported through the subsurface, it is squeezed and stretched which leads to enhanced mixing and reaction. (Rajaram and Gelhar, 1993; Kapoor and Kitanidis, 1996, 1998; Fiori, 2001; Dentz and Carrera, 2007; Moroni et al., 2007; Rolle et al., 2009; Le Borgne et al., 2010; Chiogna et al., 2011; Cirpka et al., 2011; Dentz et al., 2011; de Barros et al., 2012; Villermaux, 2012; Le Borgne et al., 2013; de Barros et al., 2015; Dentz and de Barros, 2015; Le Borgne et al., 2015).

The relationship between the global mixing/reaction behavior and transport at local scales during passive spreading has been addressed in the literature in many different ways. For an instantaneous line source under uniform flow through porous media with moderate and strong heterogeneity, Le Borgne et al. (2010) saw that the total cumulative mixing at a given time increases with the degree of permeability field heterogeneity. This increase in mixing was partly due to incomplete mixing inside the plume, which generates concentration gradients in the transverse direction, and partly due to irregular spreading which influences the concentration gradients in the longitudinal direction.

Others have sought to link the local stretching of the plume caused by the heterogeneous hydraulic conductivity field to the overall mixing/reaction behavior. Bolster et al. (2011) studied two-dimensional linear shear flow for an instantaneous point source. They found that in shear flow, the plume extends in the direction transverse to the flow due to transverse dispersion. The shear action of the flow then leads to enhanced longitudinal spreading and mixing of the solute. They demonstrated that the dilution of the plume increases quadratically with time in contrast to a uniform flow, for which it increases linearly. Additionally, for a continuous source under uniform flow through heterogeneous porous media, de Barros et al. (2012) was able to link the local transport behavior to the global mixing behavior by showing that when the plume was traveling through high shear areas, it experienced an increase in dilution.

Others have investigated the effects of flow focusing on the global mixing/reaction behavior (Cirpka, 2005; Cirpka et al., 2011; Bauer et al., 2009; Cirpka, 2015; Ye et al., 2015). Werth et al. (2006) developed simple analytical expressions quantifying the extent to which mixing and reaction are enhanced when flow is focused through a high-permeability zone. They explained that flow focusing affects mixing in two ways. First, the distance required for a solute to cross a given number of streamlines decreases. Second, the increase in velocity in the high-permeability zone, compared to the surrounding aquifer, reduces the time available for mixing and reaction. They were able to demonstrate that, for a continuous source traveling through a high permeability zone, the first effect outweighs the latter, resulting in an enhancement of transverse mixing and reaction. Rolle et al. (2009); Ye et al. (2015) performed conservative and reactive laboratory experiments that supported the conclusions made by Werth et al. (2006).

1.3   Purpose and Scope

As noted in the previous section, studies investigating the relationship between the global mixing/reaction behavior and transport at local scales during active spreading are limited. Additionally, studies investigating the relationship between the global mixing/reaction behavior and transport at local scales during combined active and passive spreading are not present in the lit-

erature. Therefore, the goal of this study is to identify local behaviors present in a variety of active spreading only, passive spreading only and combined active and passive spreading flows that enhance mixing and reaction in porous media.

The research for this dissertation was conducted according to three research objectives. The first objective was to design and analyze three active spreading scenarios for use in a laboratory experiment performed by Eric Roth. The overall goal of the combined numerical and experimental study is to quantify the effects of different active spreading scenarios on mixing and reaction. In designing and evaluating the mixing and reactive behavior of each active spreading scenario, we identified local transport behaviors in the individual steps of the active spreading scenarios that resulted in increased mixing and reaction.

The second and third objectives were to analyze, in more detail, the local transport behaviors that lead to increased mixing and reaction in the active spreading scenarios evaluated in the first objective. This work involved analyzing the global and local mixing and reaction behavior of active spreading alone, passive spreading alone, and combined active and passive spreading to identify the local behaviors in each that lead to more or less mixing and reaction compared to uniform flow through homogeneous porous media. The second objective restricted its analysis to conservative mixing. The third objective was performed for reactive mixing in which we considered bimolecular, irreversible, fast reaction.

1.4 Organization of the Dissertation

This dissertation is structured as follows. Chapter 2 includes part of a journal article that is scheduled to be submitted to Water Resources Research. The content in this chapter is part of a larger combined experimental and numerical study to quantify the effects of different active spreading scenarios on mixing and reaction. The content presented in this chapter focuses on analyzing the mixing and reaction enhancement of the three active spreading scenarios used in the laboratory experiments. We showed that while the total amount of mixing and reaction between the three scenarios was similar, the rates of increase of the individual steps of each scenario were

distinct. We identified two behaviors that corresponded to increased rates of mixing and reaction: stretching of the contaminant plume boundary as well as having the orientation of the contaminant plume boundary perpendicular to the local flow direction. Enhancing mixing and reaction via stretching has been well studied (Ottino et al., 1979; Ranz, 1979; Ou and Ranz, 1983a,b; Ottino, 1989; Clifford et al., 1998; Clifford, 1999; Villermaux and Rehab, 2000; Meunier and Villermaux, 2010; Paster et al., 2015). However, the effect of the local orientation of the contaminant plume boundary relative to the local flow direction on mixing had not yet been considered in the literature. Further investigation of these behaviors on enhancing mixing and reaction is the goal of Chapters 3 and 4 of this dissertation.

Chapter 3 includes content for a journal article scheduled to be submitted in Water Resources Research. In this study, we investigate the relationship between spreading and mixing under non-uniform flow fields typical of EIE remediation systems (active spreading) in aquifers with simple heterogeneity patterns (passive spreading). Using global and local analysis, we identify the behaviors in active spreading alone and passive spreading alone that lead to more or less mixing when compared to uniform flow in a homogeneous aquifer. Furthermore, we show that when active spreading and passive spreading are combined, the behaviors identified for each alone can either complement one another, leading to increased mixing, or compete against one other, leading to decreased mixing.

Chapter 4 includes part of a journal article scheduled to be submitted in Water Resources Research. In this study, using a similar approach to Chapter 3, we consider the relationship between spreading and mixing-controlled reaction. Using the same active spreading scenarios from Chapter 3, we identify the behaviors in active spreading that lead to more or less reaction when compared to uniform flow in a homogeneous aquifer. We find that these behaviors are similar to those found in Chapter 3 for conservative mixing.

Chapter 5 provides conclusions and recommendations for future work.

Chapter 2

Investigating the effect of different active spreading scenarios on mixing and reaction

2.1 Introduction

The cost to remediate all contaminated groundwater sites in the U.S. was recently estimated to be between $110 billion to $127 billion (National Research Council, 2013), making the need to develop and improve effective groundwater remediation methods extremely important. One such cost and energy efficient groundwater remediation method is performed by treating the contaminated groundwater in-situ. For example, an amendment is introduced into the aquifer to react with and degrade the contaminant. While this type of groundwater remediation eliminates the high cost associated with removing the contaminant from the ground, it does have its own limitations.

Specifically, the amount of contaminant degradation achieved by this method is limited by the ability of the contaminant and amendment to mix. In porous media, mixing is controlled by local diffusive and pore-scale mass fluxes, which are proportional to the product of concentration gradient and either the molecular diffusion coefficient or the dispersion coefficient. Since the length scale of these mechanisms is small compared to the size of the contaminant plume, reactions are limited to a relatively narrow region where the amendment and contaminant are close enough to mix. Therefore, applying methods which enhance mixing in groundwater will increase the efficacy of in-situ remediation.

One process that is known to enhance mixing is spreading. Spreading is the reconfiguration of the plume shape due to the spatial and spatio-temporal fluctuations in a velocity field. Spreading

leads to enhanced mixing in two ways. First, the stretching of the plume boundary increases the area available for pore-scale dispersion and molecular diffusion. Second, by conservation of mass, elongating the plume boundary requires compression of the plume perpendicular to the boundary, which increases the concentration gradient (Ottino, 1989). Spreading in groundwater can be created by spatial and spatio-temporal variations in groundwater flow forcings, such as time-varying point injections or extractions of water, that create spatially and spatio-temporally varying velocity fields. This type of spreading is called active spreading.

Many researchers have used numerical investigations to study the effect of active spreading on enhancing in-situ remediation (Tél et al., 2000; Stremler et al., 2004; Sposito, 2006; Bagtzoglou and Oates, 2007; Zhang et al., 2009; Trefry et al., 2012; Mays and Neupauer, 2012; Piscopo et al., 2013). However, experimental studies of the effects of active spreading are limited. Zhang et al. (2009) performed solute transport experiments in a decimeter scale flow cell packed with sand to study the potential for enhanced mixing of solutes in porous media under active spreading scenarios. They used two colorless reactants that, once in contact, rapidly formed a colored product, which could be digitally imaged and quantified using florescence. The limitation of this technique is that, while they were able to quantify the amount of mass of the product, they were unable to image the concentration distribution of the reactants. Since, as mentioned above, mixing depends on the local concentration gradient, quantifying the concentration distribution of the reactants themselves, and not just the product, is essential to understanding the mixing and reaction behavior.

This paper presents the results of numerical simulations that complement an experimental investigation of solute transport and mixing. The experiment used laser-induced fluorescence to quantify solute transport and mixing in a quasi-two-dimensional flow apparatus containing Pyrex glass beads that were refractive index matched to the pore fluid, glycerin. This method allows for quantification of plume concentrations, averaged over a depth of approximately 10 bead diameters. Laboratory experiments were performed to quantify the effect of different active spreading scenarios on mixing and reaction, and then compared with corresponding numerical simulations.

The content presented in this chapter is only a portion of the overall study, specifically

focusing on the design of the three active spreading scenarios used in the experiments as well as numerical analysis on the mixing and reactive behavior of each scenario. The rest of the paper is organized as follows. Section 2 provides a description of the conceptual model. Section 3 explains the numerical methods. Section 4 presents the active spreading flow scenarios along with snapshots of the numerically simulated concentration distributions of both a conservative mixing case and a reactive mixing case. Section 5 and section 6 present the results and discussion, respectively, on the mixing/reactive behavior of each scenario.

2.2   Conceptual Model

The model analyzed in this study represents a confined, two-dimensional, isotropic rectangular aquifer bounded by no flow boundaries on all sides. It is designed this way so it matches the experimental apparatus. Conservative mixing and reaction mixing simulations are performed. For the conservative mixing simulations, a circular plume of Species A with radius r_A is centered at the origin as shown in Figure 2.1a. For the reactive mixing simulations, a circular plume of species A with radius r_A is located at the center of a circular plume of species B with outer radius r_B, centered at the origin as shown in Figure 2.1b. In all simulations, four wells are placed symmetrically around the plume, each at a distance of L from the origin. A fifth well is located at the origin.

2.3   Numerical Modeling

The governing equation of the transient groundwater flow for this aquifer is given by

$$S_s \frac{\partial h}{\partial t} = \nabla \cdot K \nabla h + \sum_{j=1}^{5} Q_j(t) \delta(\mathbf{x} - \mathbf{x}_j), \tag{2.1}$$

where K is the hydraulic conductivity (here assumed to be isotropic and homogeneous), h is hydraulic head, Q_j is the injection rate in well j, $\mathbf{x} = (x, y)$ is the spatial coordinate, $\mathbf{x}_j$ is the location of well j, and $\delta()$ is the Dirac delta function. The boundary conditions are

$$\nabla h \cdot \mathbf{n} = 0 \text{ at } x = x_l, x = x_r, y = y_l, y = y_u, \tag{2.2}$$
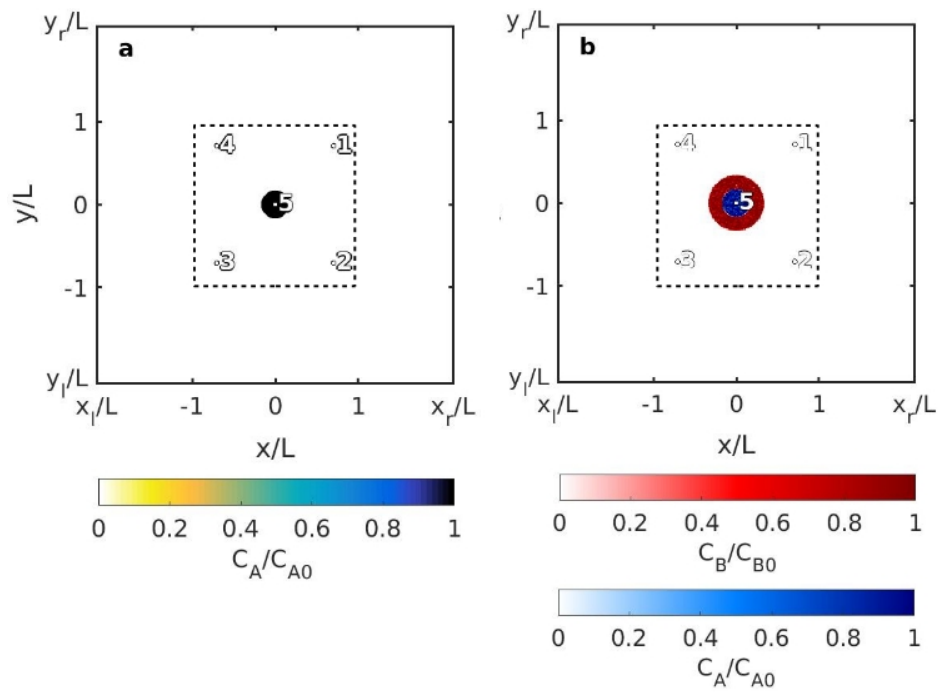
Figure 2.1: Plan view of model aquifer showing the initial concentration of (a) species A for the conservative transport simulations and (b) species A (blue) and species B (red) for the reactive transport simulations. The small open circles denote the five wells, identified by number. The remaining figures are restricted to the region inside the dashed lines.

where $\mathbf{n}$ is the outward unit normal vector. The groundwater flow equation (2.1) is solved numerically using MODFLOW, a standard finite difference groundwater flow simulator (Harbaugh et al., 2000). Parameter values are given in Tables 2.1 - 2.4.

The transport of a dissolved species in porous media is governed by the advection-dispersion-reaction equation (ADRE), given by

$$n\frac{\partial C_i}{\partial t} = -\nabla \cdot (n\mathbf{v}C_i) + \nabla \cdot \mathbf{D}n\nabla C_i - R_i, \tag{2.3}$$

where C_i is the concentration of $i = A$ (Species A), $i = B$ (Species B) and $i = C$ (Reaction Product), t is time, R_i is the reaction rate of species i, n is porosity, $\mathbf{v}$ is the groundwater velocity vector which comes from Darcy's law given by $\mathbf{v} = -(K/n)\nabla h$, and $\mathbf{D}$ is the dispersion tensor, with components given by

$$
\begin{aligned}
D_{xx} &= \alpha_L \frac{v_x^2}{|\mathbf{v}|} + \alpha_T \frac{v_y^2}{|\mathbf{v}|}, \\
D_{xy} &= D_{yx} = (\alpha_L - \alpha_T)\frac{v_x v_y}{|\mathbf{v}|}, \\
D_{yy} &= \alpha_L \frac{v_y^2}{|\mathbf{v}|} + \alpha_T \frac{v_x^2}{|\mathbf{v}|},
\end{aligned}
\tag{2.4}
$$

where α_L and α_T are the longitudinal and horizontal transverse dispersivities, respectively, with $\alpha_L > \alpha_T$, and the vertical bars denote magnitude.

For the reactive transport simulations, the chemical reaction takes the form of a bimolecular reaction, given by $A + B \rightarrow C$ (reaction product); thus, $R_A = R_B = -R_C = kC_AC_B$, where k is the reaction rate coefficient. We assume that the reaction is fast relative to the transport time scale, thus $k \rightarrow \infty$. For the conservative transport simulations, $R_i = 0$.

The initial condition for Species A is given by

$$
C_A(\mathbf{x}, 0) = \begin{cases} C_{A0} & \sqrt{x^2 + y^2} \leq r_A \\ 0 & \text{otherwise} \end{cases}
\tag{2.5}
$$

for both the conservative and reactive transport simulations, where C_{A0} is the initial concentration of Species A and r_A is the radius of the initial solute plume of Species A. The initial condition for

Species B is $C_B = 0$ for the conservative transport simulations and is given by

$$C_B(\mathbf{x}, 0) = \begin{cases} C_{B0} & r_A < \sqrt{x^2 + y^2} \leq r_B \\ \\ 0 & \text{otherwise} \end{cases} \tag{2.6}$$

for the reactive transport simulations, where C_{B0} is the initial concentration of Species B and r_B is the radius of the initial solute plume of Species B. The initial condition of Species C is $C_C = 0$ for both the conservative and reactive transport simulations. The boundary conditions for both the conservative and reactive transport simulations are given by

$$\nabla C_i \cdot \mathbf{n} = \quad 0 \text{ at } x = x_l, x = x_r, y = y_l, y = y_u. \tag{2.7}$$

The transport equation (2.3) is solved numerically using RW3D (Salamon et al., 2006), which uses random walk particle tracking. Particle tracking is a common method for modeling solute transport in aquifers known for its computational efficiency and absence of numerical dispersion (Berkowitz et al., 2006; Le Borgne et al., 2008a,b). Parameter values are given in Table 2.1. For the conservative transport simulations, the bivariate density estimation model from the R package locfit produced smooth concentration fields from the particle positions provided by RW3D (Loader, 2013). For the reactive transport simulations, the particle positions and masses provided by RW3D were first used to calculate a concentration field by binning the particles. This concentration field was then smoothed using a bivariate local likelihood regression model from locfit.

2.4   Description of Flow Scenarios

Three active spreading scenarios were used in the combined numerical and experimental investigations. The injection/extraction sequence of the first scenario, referred to as push pull, is given in Table 2.2 and the concentration distribution after each step for the conservative and reactive simulations are presented in Figures 2.2a and 2.2b, respectively. As seen in Figures 2.2a and 2.2b, the push pull scenario uses a series of injection and extraction steps to push the plume radially outward from well 5 and then pull the plume back in. During the push steps (1 and 3), the

Table 2.1: Parameter values used in numerical simulations

Parameter	Value
Hydraulic conductivity, K	0.154 cm/min
Aquifer thickness, b	4.3 cm
Porosity, n	0.311
Aquifer left boundary, x_l	-25 cm
Aquifer right boundary, x_r	25 cm
Aquifer upper boundary, y_u	25 cm
Aquifer lower boundary, y_l	-25 cm
Finite difference grid discretization	0.05 cm
Coordinates of well 1, $\mathbf{x_1}$	(8.2 cm, 8.2 cm)
Coordinates of well 2, $\mathbf{x_2}$	(8.2 cm, -8.2 cm)
Coordinates of well 3, $\mathbf{x_3}$	(-8.2 cm, -8.2 cm)
Coordinates of well 4, $\mathbf{x_4}$	(-8.2 cm, 8.2 cm)
Coordinates of well 5, $\mathbf{x_5}$	(0 cm, 0 cm)
Distance between wells, L	11.6 cm
Injection/extraction step duration	30 min
Longitudinal dispersivity, α_L	0.2 cm
Transverse dispersivity, α_T	0.02 cm
Initial concentration of species A, C_{A0}	4 mg/mL
Initial concentration of species B, C_{B0}	1 mg/mL
Radius of initial plume of species A, r_A	1.933 cm
Outer radius of initial plume of species B, r_B	3.97 cm
Number of particles of species A	2×10^5
Number of particles of species B	6×10^5

Table 2.2: Injection rates of each well for the push pull scenario. Negative rates represent extraction.

	Injection Rate (ml/min)				
Step	Well 1	Well 2	Well 3	Well 4	Well 5
1	-0.75	-0.75	-0.75	-0.75	3.00
2	0.25	0.25	0.25	0.25	-1.00
3	-0.25	-0.25	-0.25	-0.25	1.00
4	0.125	0.125	0.125	0.125	-0.5

outer wells (1-4) extract water at a low rate to maintain the same fluid volume in the experimental apparatus; likewise during the pull steps (2 and 4), the outer wells inject water at a low rate. Nevertheless, flow is essentially radial near Well 5. Consequently, this flow, is on the one hand, non-uniform and thus produces active spreading, while on the other hand, is symmetric around well 5. The radial symmetry allows the implementation of radial averaging that can be applied to both the experimental and numerical data as well as enables the use of the experimental results in calibrating the longitudinal dispersivity of the numerical model.

Because of dispersion, if the extraction rate in Step 2 were equal to the injection rate in Step 1, solute would be extracted from Well 5 during Step 2. To avoid this, the extraction rate in Step 2 is 67% lower than the injection rate in Step 1, and the extraction rate in Step 4 is 50% lower than the injection rate in Step 3.

The next scenario is called the folding scenario. The injection/extraction sequence for this scenario is given in Table 2.3 and the concentration distribution after each step for the conservative and reactive simulations are presented in Figures 2.3a and 2.3b, respectively. The motivation for this flow scenario was to create active spreading by folding (i.e., stretching) the plume around a stagnation point. As seen in Figures 2.3a and 2.3b, The first step translates the plume towards well 4. Step 2 then uses a three well injection/extraction pattern to produce a stagnation point in between wells 4 and 5 and effectively folds the plume around well 5 towards well 2. Step 3 elongates the plume in the direction of well 2 and well 4. Finally, the first two steps are repeated but in the opposite direction. Specifically, step 4 translates the plume towards well 3 while step 5 produces a stagnation point in between wells 3 and 5 and effectively folds the plume around well 5 towards

(a)

(b)

Figure 2.2: Concentration distribution after each step of the push pull sequence (Table 2.2) for (a) species A in conservative transport with flow lines (grey) and (b) species A and B in reactive transport.
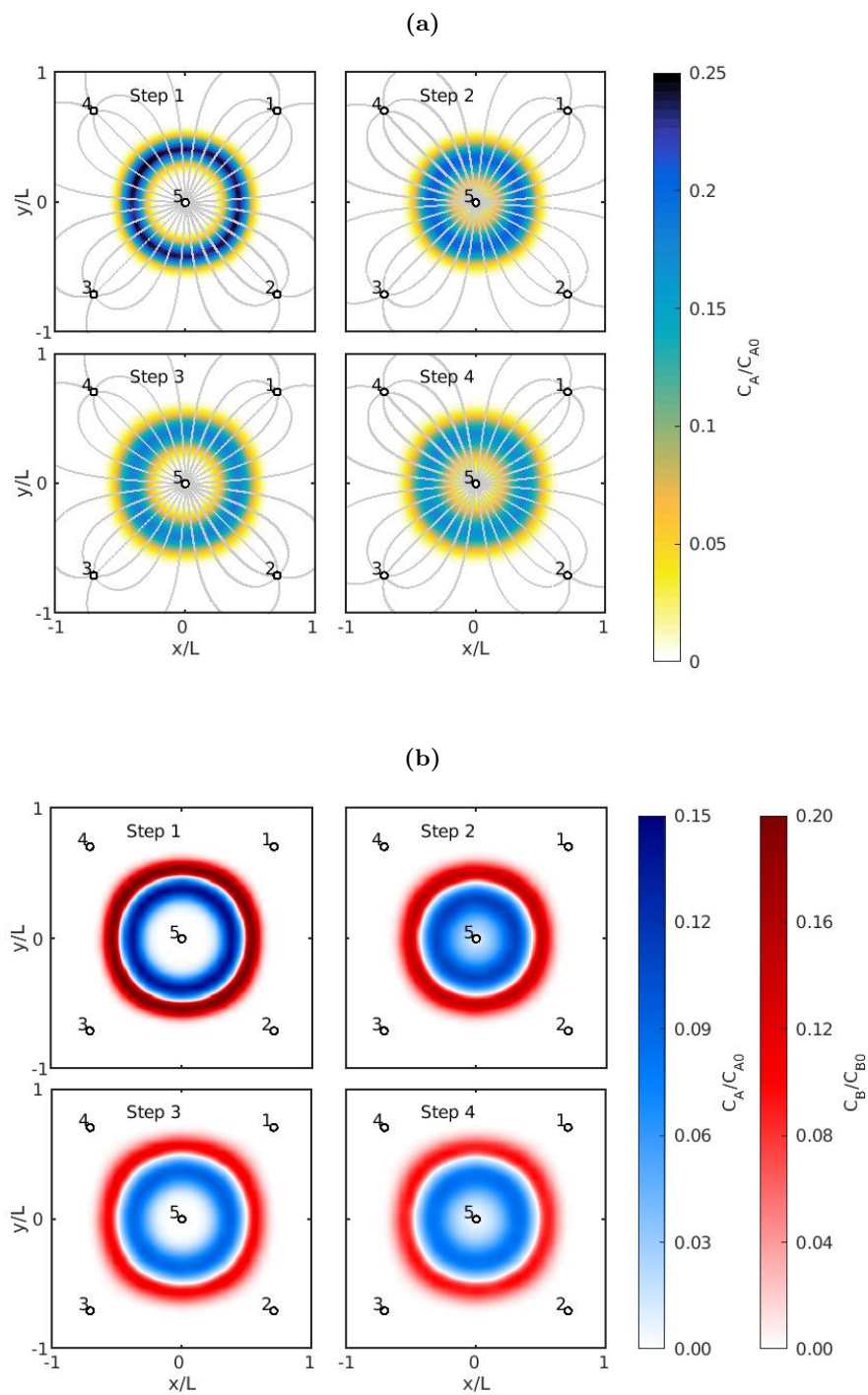
Table 2.3: Injection rates of each well for the folding scenario. Negative rates represent extraction.

	Injection Rate (ml/min)				
Step	Well 1	Well 2	Well 3	Well 4	Well 5
1	0	5.5	0	-5.5	0
2	0	-11	0	8.8	2.2
3	2.75	-0.55	2.75	-4.95	0
4	5.5	0	-5.5	0	0
5	-8.5	0	5.1	0	3.4

well 1.

The last scenario is called the oscillating scenario. The injection/extraction sequence for this scenario is given in Table 2.4 and the concentration distribution after each step for the conservative and reactive simulations are presented in Figures 2.4a and 2.4b, respectively. The motivation for this scenario was to investigate the effect of the orientation of the plume with the local flow direction on mixing. In groundwater the dispersive mass flux is greater (usually by an order of magnitude or more (Sahimi et al., 1986)) in the direction of flow than in the direction perpendicular to flow. Thus, designing a scenario where the boundary of the plume is oriented perpendicular to the flow direction should lead to enhanced mixing and reaction. To do this, the plume was first stretched to increase the interface length by injecting in the well 5 and extracting equally in wells 1-4. Then the plume was elongated in the direction of wells 2 and 4 by extracting in wells 2 and 4 and injecting in wells 1 and 3. Lastly, Wells 1 and 3 are operated as a dipole, with alternating flow direction from Step 3 to Step 4 and from Step 4 to Step 5 (Figures 2.4a and 2.4b). The elongation in step 2 oriented the plume boundary to be perpendicular to the flow lines produced by the alternating dipole in steps 4 and 5.

2.5   Results

The amount of mixing achieved in the conservative mixing simulations is measured by the dilution index, $E(t)$, given by

$$E(t) = \exp\left[-\int (P(\mathbf{x},t)\ln(P(\mathbf{x},t))d\mathbf{x})\right], \tag{2.8}$$

(a)

(b)
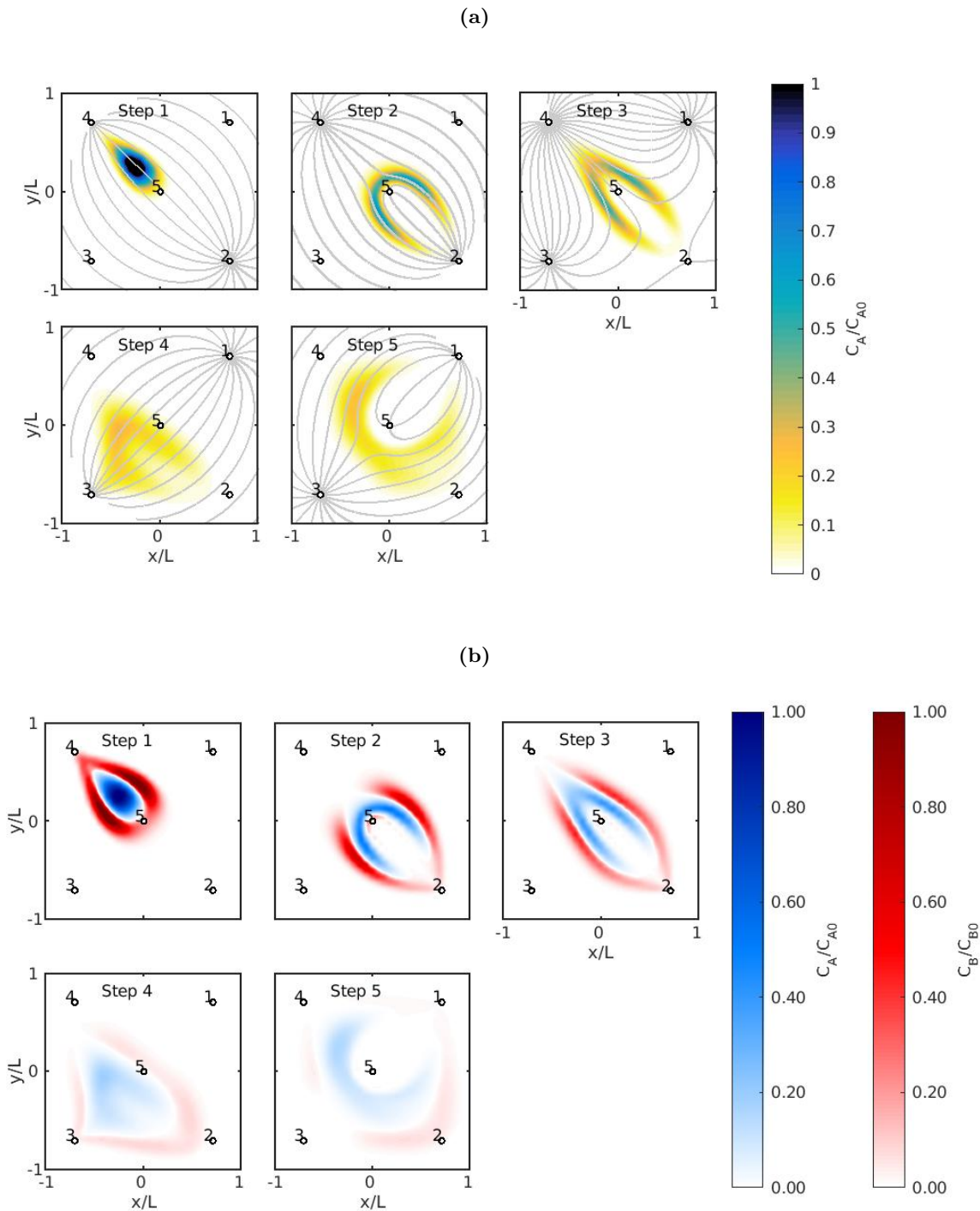
Figure 2.3: Concentration distribution after each step of the folding sequence (Table 2.3) for (a) species A in conservative transport with flow lines (grey) and (b) species A and B in reactive transport.
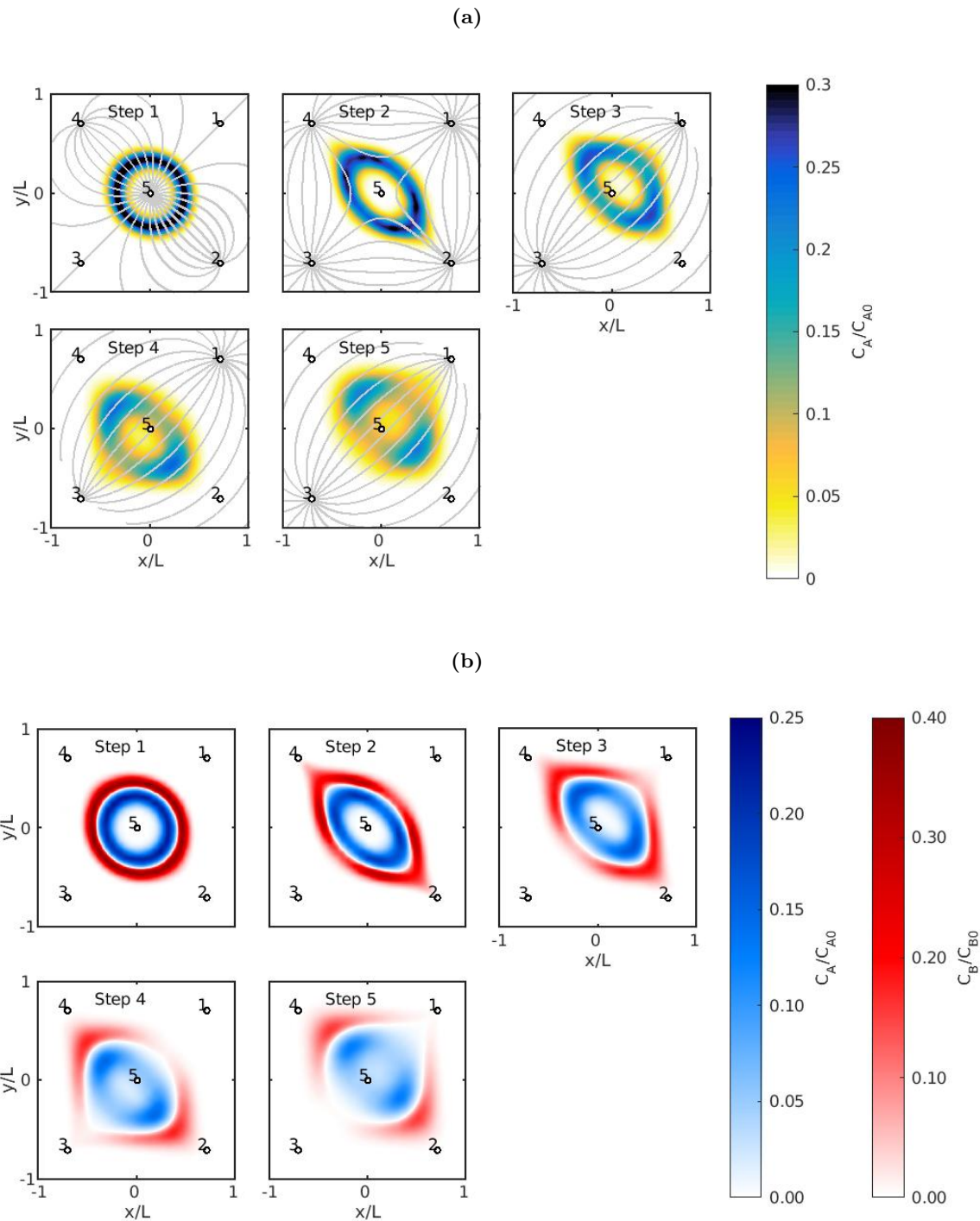
Figure 2.4: Concentration distribution after each step of the oscillating sequence (Table 2.4) for (a) species A in conservative transport with flow lines (grey) and (b) species A and B in reactive transport.

Table 2.4: Injection rates of each well for the oscillating scenario. Negative rates represent extraction.

	Injection Rate (ml/min)				
Step	Well 1	Well 2	Well 3	Well 4	Well 5
1	0	-1	0	-1	2
2	2	-2	2	-2	0
3	-2	0	2	0	0
4	4	0	-4	0	0
5	-4	0	4	0	0

where $P(\mathbf{x}, t)$ is concentration normalized by the total solute mass, $\mathbf{x}$ is the spatial coordinate and t is time (Kitanidis, 1994). The dilution index is based on entropy concepts and quantifies the volume occupied by the solute (Kitanidis, 1994). As such, it measures the mixing state of a plume. The $E(t)$ is normalized by E_0, where E_0 is the dilution index of the initial plume of species A.

The amount of reaction in the reactive mixing simulations is presented as cumulative mass reacted, $M_{\mathrm{rxn}}(t)$, given by

$$M_{\mathrm{rxn}}(t) = M_{A0} - M_A(t), \tag{2.9}$$

where $M_A(t)$ is the current mass of solute A with time and M_{A0} is the initial mass of solute A.

We compared the amount of mixing or reaction that occurred across all three scenarios. Figure 2.5a plots $E(t)/E_0$ for the three conservative mixing scenarios. For the push pull scenario, $E(t)$ increases at a decreasing rate. Over half of the total increase in E occurs in the first step alone. For the oscillating scenario, $E(t)$ also increases at a decreasing rate, similar to the push pull scenario. However, the rate of increase of the first step is lower than that the push pull scenario while the rate of the subsequent steps is higher than the push pull scenario. For the foldings sequence, $E(t)$ increases at a much slower rate than either the push pull or oscillating scenarios for the first three steps. However, starting at step 4, the slope increases. The rate of increase is similar to step 1 of the push pull scenario. As described above, the behavior of $E(t)$ of each scenario is distinct; nonetheless, all three scenarios converge to roughly the same value of $E(t)$ after 120 minutes.

Figure 2.5b plots the cumulative mass reacted of species A, $M_{\mathrm{rxn}}(t)$, for the three scenarios.

$M_{\text{rxn}}(t)$ follows the same patterns as $E(t)$. For all scenarios, $M_{\text{rxn}}(t)$, similar to $E(t)$, increases at a decreasing rate, with the push-pull scenario having the highest growth at $t = 0$ and the folding scenario the lowest. Furthermore, at the end of all three active spreading scenarios, M_{rxn} is approximately 84%.

2.6   Discussion

As seen in Figures 2.5a and 2.5b, $E(t)$ and $M_{\text{rxn}}(t)$ increase the fastest during the first step, for both the push pull scenario and the oscillating scenario. Both of these scenarios inject in the center well (well 5) during step 1, producing local velocities that are everywhere perpendicular to the boundary of the plume (Figures 2.2a and 2.4a) . Thus, the dispersion coefficient is dominated by the longitudinal dispersivity, which, as mentioned before, is usually an order of magnitude higher that the transverse dispersivity (Sahimi et al., 1986). Also, the radial flow stretches the plume perpendicular to the local flow direction and compresses in the opposite direction, thereby increasing the concentration gradient and enhancing mixing. The combination of high dispersion coefficient and stretching perpendicular to flow produces the high rate of increase during the first step.

For the push pull scenario, since the injection and extraction rates are lower in Steps 2-4 (compared to step 1), the local velocities are lower, reducing the local dispersion coefficient and therefore the rate of mixing and reaction. For the oscillating scenario, the injection rate at well 5 is 33% lower than the push pull scenario, which explains why the rate of increase of both $E(t)$ and $M_{\text{rxn}}(t)$ for the oscillating scenario is lower than that of the push pull scenario. Also, for the oscillating scenario, the rate of increase of $E(t)$ and $M_{\text{rxn}}(t)$ is higher during steps 3-5 than during step 2 but not as high as during step 1. A probable explanation is that the dipole between wells 2 and 4 during steps 3-5 create a flow field that has a substantial portion of the plume boundary aligned perpendicular to the local velocities, but not the complete boundary as in radial flow (Figure 2.4a).

For the folding sequence, both $E(t)$ and $M_{\text{rxn}}(t)$ increase quickly during step 4 because a
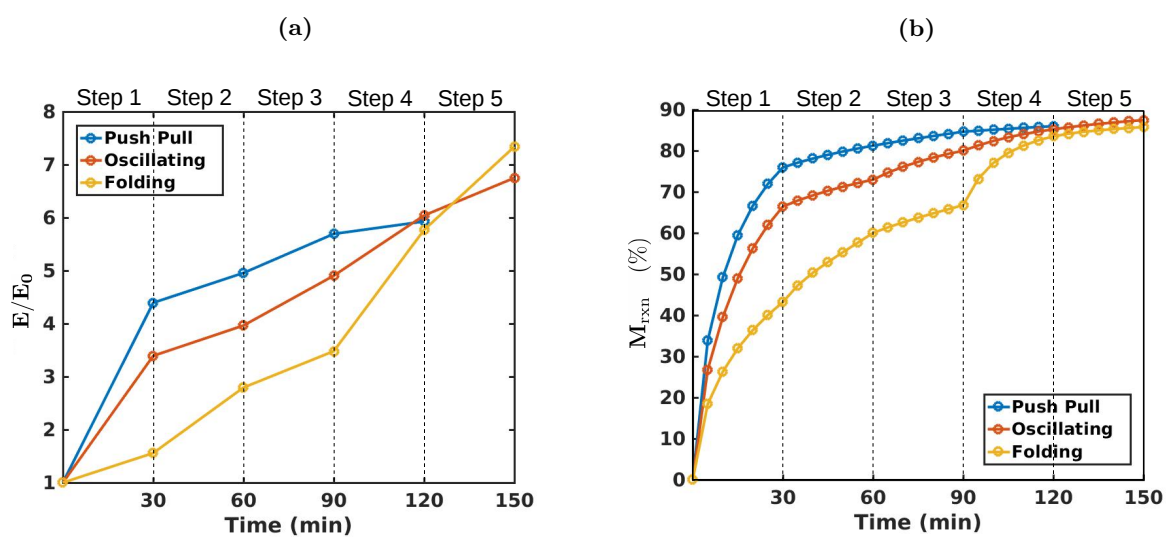
Figure 2.5: Evolution of mixing and reaction with time. (a) Normalized dilution index, $E(t)/E_0$, for each conservative mixing active spreading scenario and (b) cumulative mass reacted of species A, M_{rxn}, for each reactive mixing active spreading scenario.

substantial portion of the plume interface is perpendicular to the flow direction (Figure 2.3a). This orientation was the result of the folding during step 2, where the direction of stretching is parallel to the direction of flow, causing the plume boundary to become increasingly parallel to the local flow direction (Figure 2.3a). Unlike the behavior observed in the push pull and oscillating scenarios, when the plume boundary is parallel to the local flow direction, the dispersion coefficient is controlled by the transverse dispersivity which limits mixing enhancement. However, since the folding in step 2 is followed by a flow field that is oriented perpendicular to the stretched plume boundary in step 4, the stretching during the folding step promotes the mixing and reaction enhancement observed in step 4.

Unlike the push pull and oscillating scenarios, there are some differences between $E(t)$ and $M_{\mathrm{rxn}}(t)$ for the folding sequence that warrant further discussion. In particular, $M_{\mathrm{rxn}}(t)$ increases quickly during step 1 while $E(t)$ does not and $E(t)$ increases quickly during step 5 while $M_{\mathrm{rxn}}(t)$ does not. The value of $M_{\mathrm{rxn}}(t)$ grows quickly during step 1 because the concentrations of species A and B are initially uniform, producing high concentration gradients of A and B at the interface, producing high dispersive mass flux, which brings the molecules of A and B together to react, independent of the flow field. The value of $E(t)$ grows quickly during step 5 because again, the plume boundary is perpendicular to the flow direction. In contrast, $M_{\mathrm{rxn}}(t)$ does not increase quickly during step 5 because the flow field in this step separates portions of plume A and B thus limiting the amount of reaction that occurs (Figure 2.3b).

2.7   Conclusion

This study showed that while the amount of mixing and reaction after 120 days was similar between scenarios, the rates of increase of the individual steps were distinct. By analyzing the different flow fields in each step we were able to identify certain features of the active spreading flow fields that corresponded to increased rates of mixing and reaction. Specifically, we observed that when the plume boundary was oriented perpendicular to the direction of flow as well as stretched perpendicular to the direction of flow the rate of increase of mixing and reaction was high. Addi-

tionally, we also observed that stretching parallel to the direction of flow leads to high mixing and reaction rates when it was followed in a subsequent step by a flow field oriented perpendicular to the plume boundary. Thus, the effect of active spreading on mixing and reaction is not only due to the increase in surface area available for mixing and reaction via stretching. The orientation of the plume as well as the direction of spreading with respect to the flow direction is also important.

Chapter 3

Investigating the degree to which active spreading and passive spreading contribute to mixing.

3.1   Introduction

In-situ groundwater remediation is a common method for cleaning up contaminated groundwater. During in-situ groundwater remediation, a chemical or biological amendment is introduced into the aquifer to react with and degrade the contaminant. In this type of remediation, degradation depends on the ability of the amendment to mix into and react with the contaminant. In porous media, mixing is driven by molecular diffusion and pore-scale dispersion (Bellin et al., 2011). Since the length scale of these mechanisms is small compared to the size the plume, reactions are limited to a relatively narrow region, referred to as the reaction front, where the amendment and contaminant are close enough to mix. Thus, enhancements in mixing will lead to enhancements in degradation.

One process that is known to enhance mixing is spreading (Le Borgne et al., 2010). Spreading is the reconfiguration of the plume due to spatially-varying velocity. When a solute plume is stretched due to spreading, the area where mixing and reaction occurs is increased. In addition, this stretching of the reaction front increases concentration gradients (Ou and Ranz, 1983a). Together, these two mechanisms lead to enhanced mixing and reaction.

Spreading occurs both passively and actively. With passive spreading, variability in the hydraulic conductivity (and consequently, in the velocity field) spreads the solute plume, which can lead to enhanced mixing and reaction (Kapoor and Kitanidis, 1996, 1998; Le Borgne et al., 2010,

2013; de Anna et al., 2014; Le Borgne et al., 2015) . Active spreading, on the other hand, is created by spatial and temporal variations in groundwater flow forcings (Lester et al., 2010; Piscopo et al., 2013; Trefrý et al., 2012; Zhang et al., 2009).

For an instantaneous point-like source, Bolster et al. (2011) studied how two-dimensional linear shear flow, as a simple representation for flow through a spatially heterogeneous medium, affects mixing dynamics. They found that in shear flow, the plume extends in the direction transverse to the flow due to transverse dispersion. The shear action of the flow then leads to enhanced longitudinal spreading and mixing of the solute. For an instantaneous line source under uniform flow through porous media with moderate and strong heterogeneity, Le Borgne et al. (2010) saw that the total cumulative mixing at a given time increases with the degree of permeability field heterogeneity. This increase in mixing was partly due to incomplete mixing inside the plume, which generates concentration gradients in the transverse direction, and partly due to irregular spreading which influences the concentration gradients in the longitudinal direction.

Mays and Neupauer (2012) proposed an active spreading method called engineered injection and extraction (EIE) . EIE consists of injecting an amendment into the contaminated groundwater and then implementing a sequence of injections and extractions of clean water at an array of wells surrounding the contaminant plume to create unsteady flow fields that stretch the interface between the treatment solution and contaminated groundwater, effectively spreading the amendment into the contaminant plume.

While EIE has been shown to enhance reaction during in-situ remediation (Piscopo et al., 2013; Rodríguez-Escales et al., 2017), the mechanisms of active spreading that lead to enhanced mixing and mixing-controlled reaction in porous media are not well understood. Le Borgne et al. (2014) studied the impact of reaction front deformation under radial flow (the most simple active spreading flow field). They developed an approach based on a lamellar representation of fluid mixing that provides a direct link between fluid deformation, the distribution of concentration gradients, and the reaction rate. Using this approach, they show that the temporal evolution of the reaction rate is determined by the flow topology and the distribution of local velocity gradients which leads

to an increase in the reaction that is orders of magnitude larger than in uniform flow.

The goal of this work is to investigate the relationship between spreading and mixing under non-uniform flow fields typical of EIE remediation systems (active spreading) in aquifers with simple heterogeneity patterns (passive spreading). EIE operations manipulate the interface between the contaminant plume and the amendment plume; thus, unlike Le Borgne et al. (2014) in which the plume boundary is everywhere transverse to the local flow direction, the local orientation of the contaminant plume boundary relative to the local flow direction varies spatially and temporally. We model velocity-dependent mechanical dispersion which depends on both the magnitude and direction of the local velocity. Since the dispersion coefficient is higher in the direction of flow, and since the concentration gradient is highest perpendicular to the plume interface, dispersive mass flux is highest where the plume interface is perpendicular to the local flow direction and lowest where it is perpendicular to the local flow direction. These effects can be augmented or diminished by aquifer heterogeneity. Since the subsurface is inherently heterogeneous, insights gained from this research will provide crucial information for the optimal design of EIE systems in the field.

The rest of the paper is organized as follows. Section 2 describes the aquifer used in the numerical simulations, the active spreading and passive spreading flow fields, and the numerical model used. Section 3 introduces the global and local measures used to analyze the results. Section 4,5 and 6 presents the effects of active spreading alone, passive spreading alone, and the active and passive spreading combined, respectively. Lastly, our conclusions are given in section 7.

3.2   Conceptual Model

The aquifer in this study is assumed to be confined, two-dimensional, isotropic and rectangular in shape, bounded by no flow boundaries on the north and south and specified head boundaries on the east and west (Figure 3.1). For the simulations that include passive spreading, the ambient flow is from west to east. For the simulations that only include active spreading, we assume that ambient flow is negligible. A circular solute plume of diameter, d, is centered at (x_p, y_p).

For the active spreading scenarios, we consider a homogeneous aquifer with three wells,
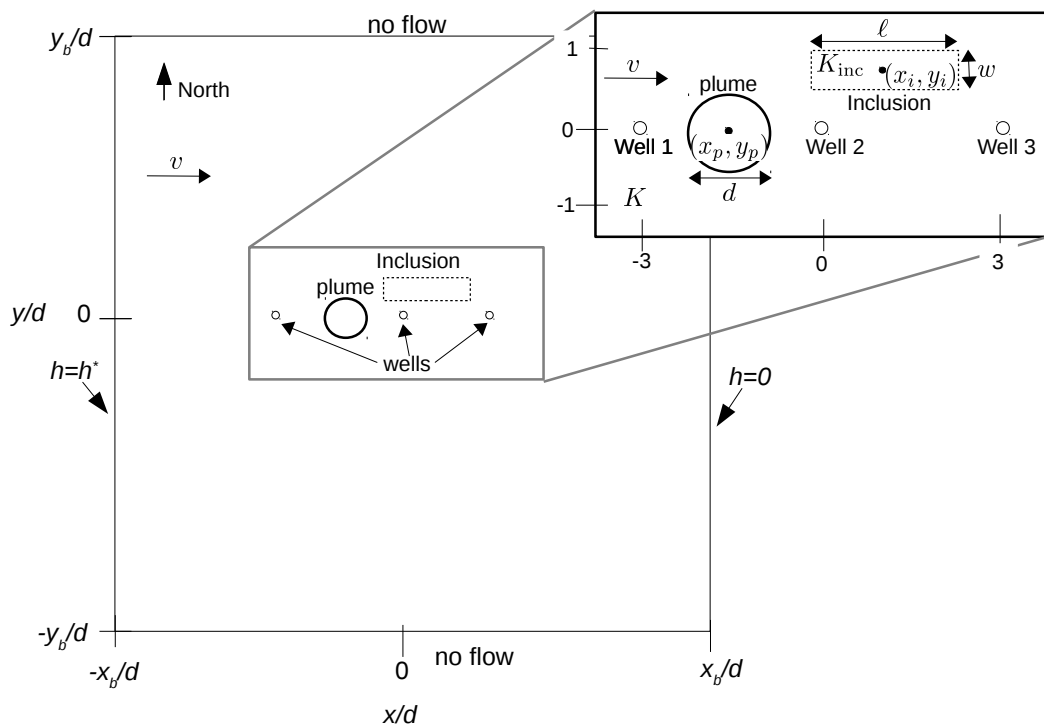
Figure 3.1: Schematic of the aquifer showing the aquifer boundaries, the location of the wells (small open circles), the initial position of the circular plume (large open circle) and the location of the inclusion (dotted line). The zoomed in image shows the length, ℓ, width, w, and center, (x_i, y_i), of the inclusion as well as the initial position of the circular plume of diameter, d, and center (x_p, y_p). The hydraulic conductivity of the aquifer and inclusion are K and K_{inc}, respectively. The arrow, labeled with a v, represents the mean direction of ambient flow.

Table 3.1: Details of active spreading scenarios. $\rho(T)$ is the total distance traveled by the plume centroid, where T is the time required for the plume centroid to travel said distance. Negative injection rates represent extraction.

Scenario Name	Plume center $(x_p/d, y_p/d)$	T (days)	$\rho(T)/d$ (-)	Injection/Extraction Pattern		
				Well 1	Well 2	Well 3
Radial	(0,0)	1.1	2	0	$+Q$	0
Diverging	(-1.5,0)	11.5	2	$+Q$	0	0
Converging	(-1.5,0)	15.75	2	0	0	$-Q$
Dipole	(-1.5,0)	6.3	2	$+Q$	0	$-Q$
Stagnation	(-1.5,0)	9.5	2	$+0.8Q$	$+0.2Q$	$-Q$

separated by a distance of $3d$ (Figure 3.1). We investigate five active spreading scenarios that represent components of EIE. Schematics of the flow fields are shown in Figure 3.2 and details are provided in Table 3.1. In the 'Radial' scenario, a single well at the center of the solute plume injects water into the aquifer, creating a radial flow field (Figure 3.2a). In the 'Diverging' scenario, a single well to the west of the solute plume injects water into the aquifer, creating a diverging flow field (Figure 3.2b). In the 'Converging' scenario, a single well to the east of the solute plume extracts water from the aquifer, creating a converging flow field (Figure 3.2c). The 'Dipole' scenario is the combination of the 'Diverging' and 'Converging' scenarios (Figure 3.2d). The 'Stagnation' scenario is similar to the 'Dipole' scenario except that the injection is distributed over two wells, creating a stagnation point (Figure 3.2e).

For the passive spreading scenarios, we consider a homogeneous aquifer with a rectangular-shaped inclusion shown schematically in Figure 3.1. We consider eight different passive spreading scenarios, with details given in Table 3.2. All active and passive spreading scenarios are compared to uniform flow with a velocity of $\mathbf{v}_u$ in a homogeneous aquifer, which has neither active nor passive spreading.

3.3   Numerical Modeling

The governing equation of steady-state groundwater flow for this aquifer is given by

$$0 = \nabla \cdot K \nabla h + \sum_{j=1}^{3} Q_j(t)\delta(\mathbf{x} - \mathbf{x}_j), \tag{3.1}$$
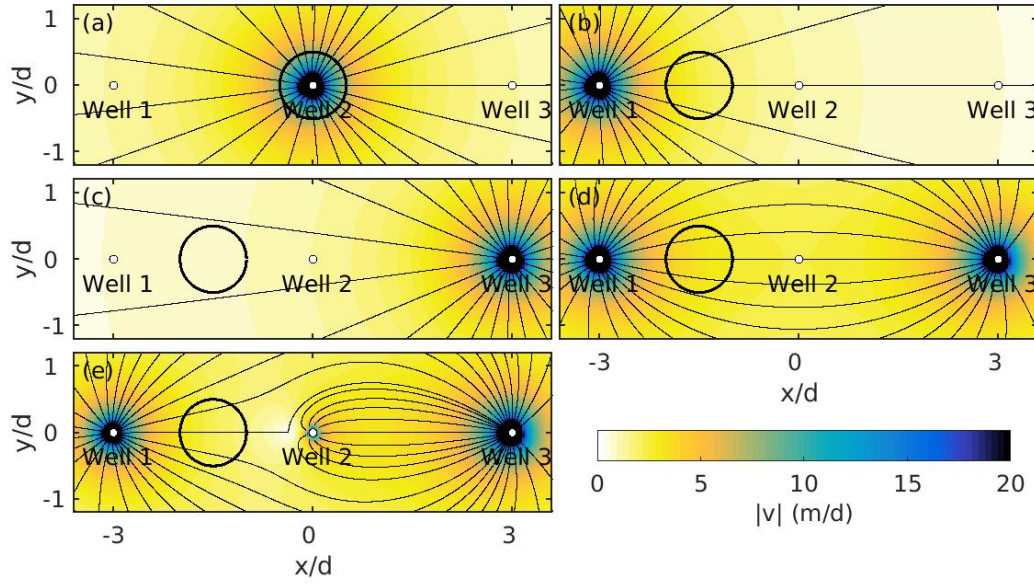
Figure 3.2: The magnitude, $|\mathbf{v}|$, of the velocity field for the active spreading scenarios. (a) 'radial', (b) 'diverging', (c) 'converging', (d) 'dipole' and (e) 'stagnation' active spreading scenarios. Also shown are flow lines (thin black lines), location of the wells (open circles), and the initial position of the circular plume (thick black line).

Table 3.2: Details of passive spreading scenarios (see Figure 3.1 for notation). $\rho(T)$ is the total distance traveled by the plume centroid, where T is the time required for the plume centroid to travel said distance.

Scenario Number	K/K_{inc}	Plume Center $(x_p/d, y_p/d)$	T (days)	$\rho(T)/d$ (-)	Inclusion Geometry		
					Width w/d	Length ℓ/d	Center $(x_i/d, y_i/d)$
P1	10	(-1.5,0)	18	3	0.25	1	0
P2	10	(-1.5,0)	18	3	0.5	1	0
P3	100	(-1.5,0)	16	3	0.25	1	0
P4	100	(-1.5,0)	16	3	0.5	1	0
P5	0.1	(-1.5,0)	26	3	0.5	1	0
P6	0.1	(-1.5,0)	28	3	1	1	0
P7	0.01	(-1.5,0)	26	3	0.5	1	0
P8	0.01	(-1.5,0)	28	3	1	1	0

where K is the hydraulic conductivity (here assumed to be isotropic and heterogeneous), h is hydraulic head, Q_j is the injection rate in well j, $\mathbf{x} = (x, y)$ is the spatial coordinate, $\mathbf{x}_j$ is the location of well j, and $\delta()$ is the Dirac delta function. The boundary conditions are

$$\frac{\partial h}{\partial y} = 0 \text{ at } y = \pm y_b \tag{3.2}$$

$$h = h^* \text{ at } x = -x_b \tag{3.3}$$

$$h = 0 \text{ at } x = x_b, \tag{3.4}$$

The groundwater flow equation (3.1) is solved numerically using MODFLOW, a standard finite difference groundwater flow simulator (Harbaugh et al., 2000). Parameter values are given in Table 3.3.

The transport of a conservative species in porous media is governed by the advection-dispersion equation (ADE), given by

$$n\frac{\partial C}{\partial t} = -\nabla \cdot (n\mathbf{v}C) + \nabla \cdot \mathbf{D}n\nabla C, \tag{3.5}$$

where C is the concentration, t is time, n is porosity, $\mathbf{v} = (v_x, v_y)$ is the groundwater velocity vector which comes from Darcy's law, given by $\mathbf{v} = -(K/n)\nabla h$ and $\mathbf{D}$ is the dispersion tensor, with components given by

$$\begin{aligned} D_{xx} &= \alpha_L \frac{v_x^2}{|\mathbf{v}|} + \alpha_T \frac{v_y^2}{|\mathbf{v}|}, \\ D_{xy} &= D_{yx} = (\alpha_L - \alpha_T)\frac{v_x v_y}{|\mathbf{v}|}, \\ D_{yy} &= \alpha_L \frac{v_y^2}{|\mathbf{v}|} + \alpha_T \frac{v_x^2}{|\mathbf{v}|}, \end{aligned} \tag{3.6}$$

where α_L and α_T are the longitudinal and horizontal transverse dispersivities, respectively, and $\alpha_L > \alpha_T$. The initial and boundary conditions are given by

$$C(\mathbf{x}, 0) = \begin{cases} C_0 & \text{for } \sqrt{(x - x_p)^2 + (y - y_p)^2} \leq d/2 \\ 0 & \text{otherwise} \end{cases} \tag{3.7}$$

$$\nabla C_i \cdot \mathbf{n} = 0 \text{ at } x = \pm x_b, y = \pm y_b. \tag{3.8}$$

where C_0 is the initial concentration of the solute plume, x_p and y_p are the coordinates of the center of the initial solute plume, d is the diameter of the initial solute plume, and $\mathbf{n}$ is the outward unit normal vector.

The transport equation (3.5) is solved numerically using RW3D (Salamon et al., 2006), which uses random walk particle tracking. Particle tracking is a common method for modeling solute transport in aquifers known for its computational efficiency and absence of numerical dispersion (Berkowitz et al., 2006; Le Borgne et al., 2008a,b). Parameter values are given in Table 3.3. The bivariate density estimation model from the R package locfit produced smooth concentration fields from the particle positions provided by RW3D (Loader, 2013).

Figures 3.3-3.10 show the simulated plumes at three different times for uniform flow, the five active spreading scenarios, and P3 and P8 of the passive spreading scenarios, respectively. These figures show how the plume shape changes over time in each spreading scenario. For some the plumes are stretched in the direction of flow (Figures 3.6 and 3.9) while others are stretched perpendicular to flow (Figures 3.4,3.5 and 3.9) and others experience stretching in both directions (Figures 3.7,3.8 and 3.10). Note that the times shown vary between scenarios. Since the plumes travel at different rates in different scenarios, it is more informative to compare the scenarios in terms of some characteristic distance, $\rho(t)$, traveled by the plume (shown in Figures 3.3-3.10).

Due to some unique plume behavior, we define $\rho(t)$ slightly differently between scenarios. For the radial scenario, $\rho(t)$ is the diameter of a circle whose circumference is the advective travel distance from the centroid of the plume. For uniform flow, the remaining active spreading scenarios, and scenarios P1-P4, $\rho(t)$ represents the distance traveled by the center of mass of the plume. For scenarios P5-P8, $\rho(t)$ represents the distance traveled by the center of mass of the portion of the plume that remains outside of the inclusion, since the plume can split in two, and the portion inside the inclusion travels much more slowly. The total travel distance of the plume in each scenario was chosen to be low enough that the plume was not yet extracted at Well 3 for the active spreading scenarios and high enough that the plume traveled downstream of the inclusion for the passive spreading scenarios. For the well placement and plume geometry used in this study, a single travel

Table 3.3: Parameter values used in numerical simulations.

Parameter	Value
Field hydraulic conductivity, K	1 m/d
Aquifer thickness, b	10 m
Porosity, n	0.25
Aquifer left boundary, $-x_b$	-150.125 m
Aquifer right boundary, x_b	150.125 m
Aquifer upper boundary, y_b	150.125 m
Aquifer lower boundary, $-y_b$	-150.125 m
Finite difference grid discretization	0.25 m
Head at $x = -x_b$, h^*	
Active spreading scenarios	0 m
Passive spreading scenarios	75.0625 m
Combined active and passive spreading scenarios	75.0625 m
Injection rate, Q	500 m^3/d
Uniform velocity, $\mathbf{v}_u$	1 m/d
Coordinates of well 1, $\mathbf{x_1}$	(-25 m,0 m)
Coordinates of well 2, $\mathbf{x_2}$	(0 m,0 m)
Coordinates of well 3, $\mathbf{x_3}$	(25 m,0 m)
Longitudinal dispersivity, α_L	0.1 m
Transverse dispersivity, α_T	0.01 m
Initial concentration of solute plume, C_0	25.6 mg/m^3
Diameter of initial solute plume, d	8.33 m
Number of solute particles	2x10^5

distance would not satisfy both of these conditions. Each active spreading scenarios is run until $\rho(T)/d = 2$ while each passive spreading scenarios is run until $\rho(T)/d = 3$, where T is the time required for the plume centroid to travel said distance. The value of T for each scenario varies due to the variation in velocities sampled by the plume and is given in Tables 3.1 and 3.2. For uniform flow, when comparing to the active spreading scenarios, $T = 17$ and when comparing to the passive spreading scenarios, $T = 24$.

3.4   Measures

We use several global and local measures, described in this section, to analyze the active and passive spreading scenarios. The global measures are used to determine the degree of mixing enhancement of each spreading scenario. We define mixing enhancement as the increase in the measure relative to its value for uniform flow (no active spreading) in a homogeneous (no passive spreading) aquifer. If the measure decreases relative to uniform flow in a homogeneous aquifer, mixing is negatively enhanced. The local measures are used to identify the spreading mechanisms responsible for said mixing enhancement. As we introduce each measure, we evaluate it for uniform flow in a homogeneous aquifer to understand its behavior without any active or passive spreading.

3.4.1   Global Measures

We measure the global mixing behavior of the plumes using two different methods. The first global measure is the dilution index, $E(t)$, given by

$$E(t) = \exp\left[-\int P(\mathbf{x}, t) \ln[P(\mathbf{x}, t)]d\mathbf{x}\right],\tag{3.9}$$

where $P(\mathbf{x}, t)$ is concentration normalized by the total solute mass (Kitanidis, 1994). The dilution index is based on entropy concepts and quantifies the volume occupied by the solute. Since the volume increases as a result of diffusion and pore-scale dispersion, i.e., the processes that represent mixing, the dilution index measures the mixing state of a plume.

The motivation for our second method comes from reactive mixing. Consider two species S_1
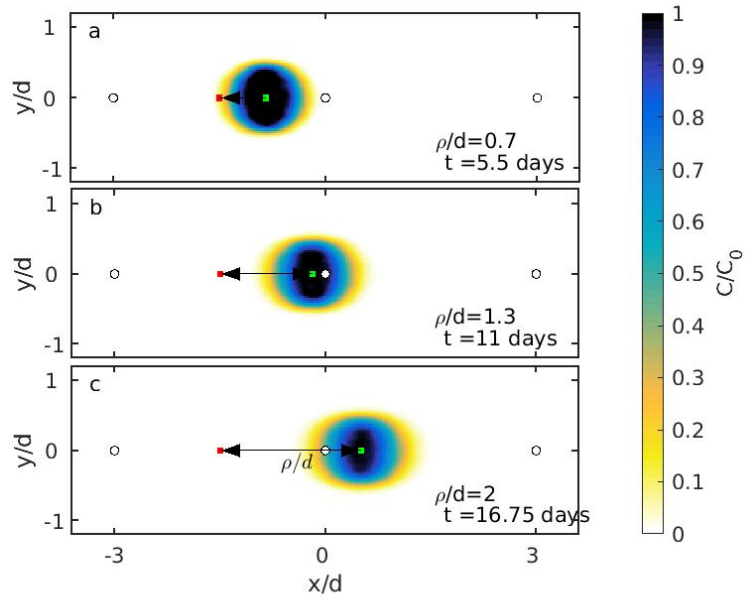
Figure 3.3: Concentration distribution of the solute plume for uniform flow at $\rho/d = 0.7, 1.3, 2$. The red square represents the center of the initial plume, (x_p, y_p), the green square represents the centroid the plume and the distance between them represents the normalized travel distance of the plume ρ/d. The open circles represent the well locations.
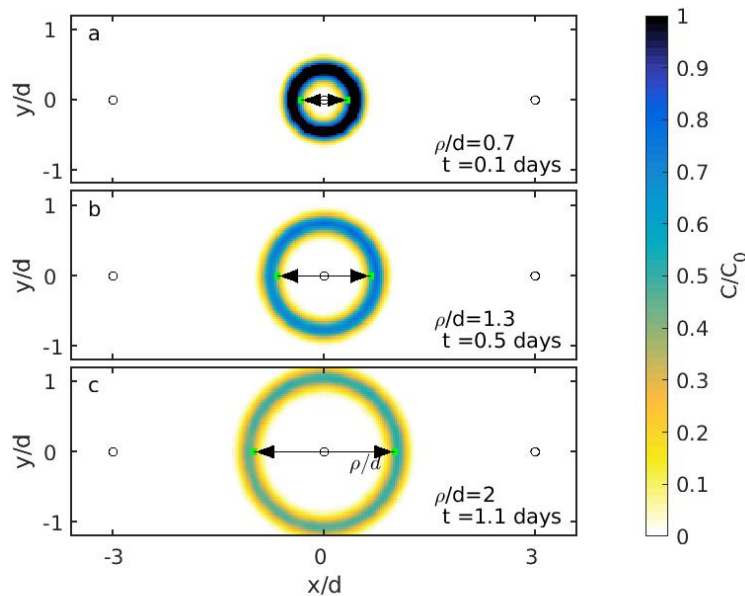
Figure 3.4: Concentration distribution of the solute plume for the radial scenario at $\rho/d = 0.7, 1.3, 2$. The red square represents the center of the initial plume, (x_p, y_p), the green square represents the location of a particle placed at the origin under pure advective travel and the distance between them represents the normalized travel distance of the plume ρ/d. The open circles represent the well locations.

Figure 3.5: Concentration distribution of the solute plume for the diverging scenario at $\rho/d = 0.7, 1.3, 2$. The red square represents the center of the initial plume, (x_p, y_p), the green square represents the centroid the plume and the distance between them represents the normalized travel distance of the plume ρ/d. The open circles represent the well locations.

Figure 3.6: Concentration distribution of the solute plume for the converging scenario at $\rho/d = 0.7, 1.3, 2$. The red square represents the center of the initial plume, (x_p, y_p), the green square represents the centroid the plume and the distance between them represents the normalized travel distance of the plume ρ/d. The open circles represent the well locations.
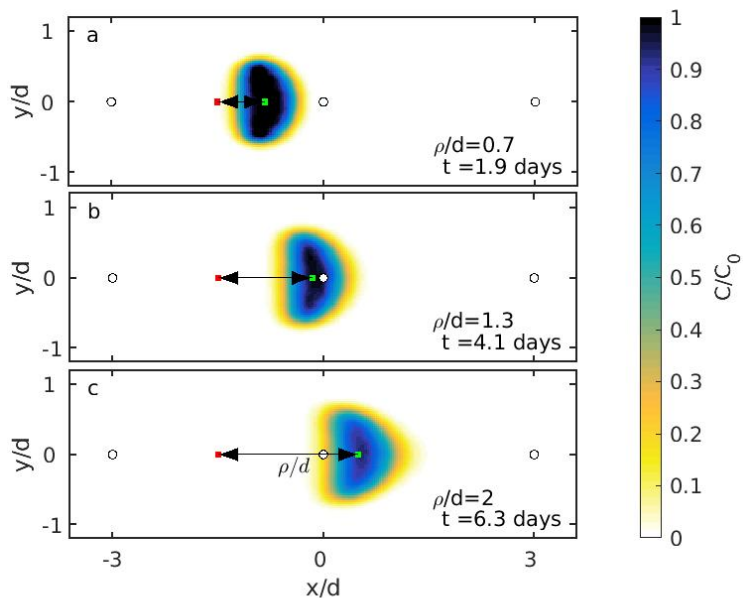
Figure 3.7: Concentration distribution of the solute plume for the dipole scenario at $\rho/d = 0.7, 1.3, 2$. The red square represents the center of the initial plume, (x_p, y_p), the green square represents the centroid the plume and the distance between them represents the normalized travel distance of the plume ρ/d. The open circles represent the well locations.
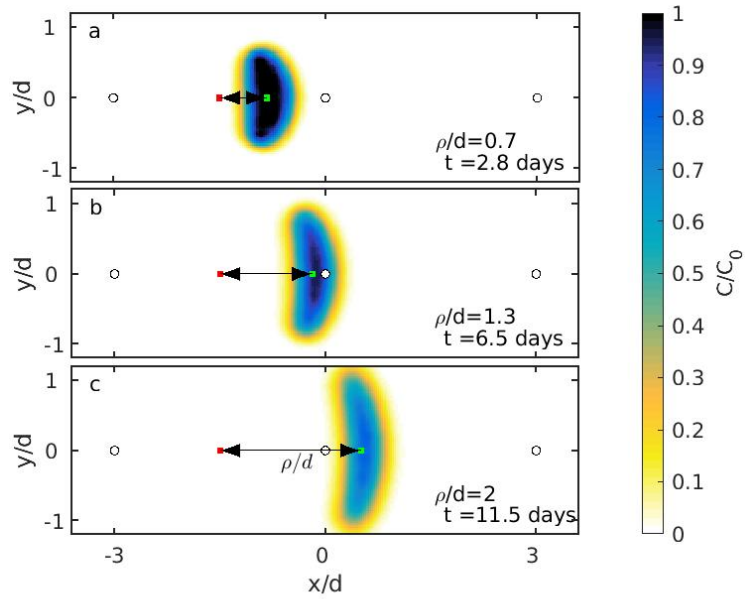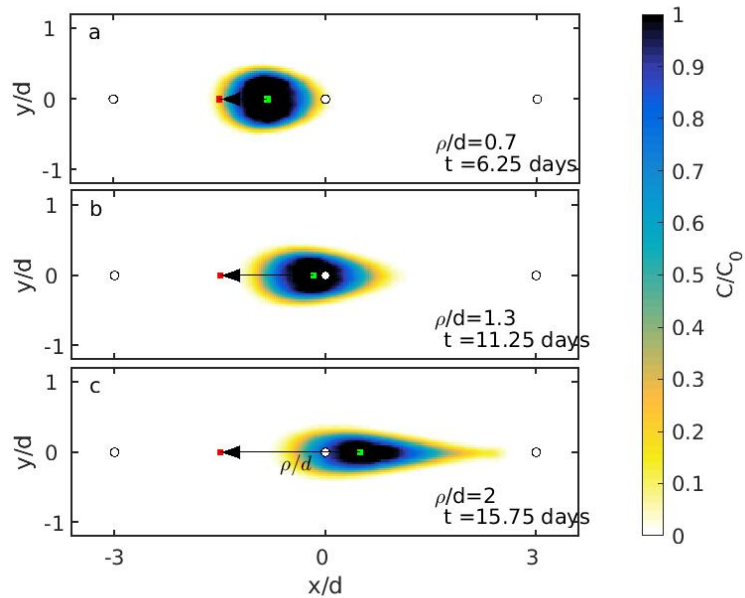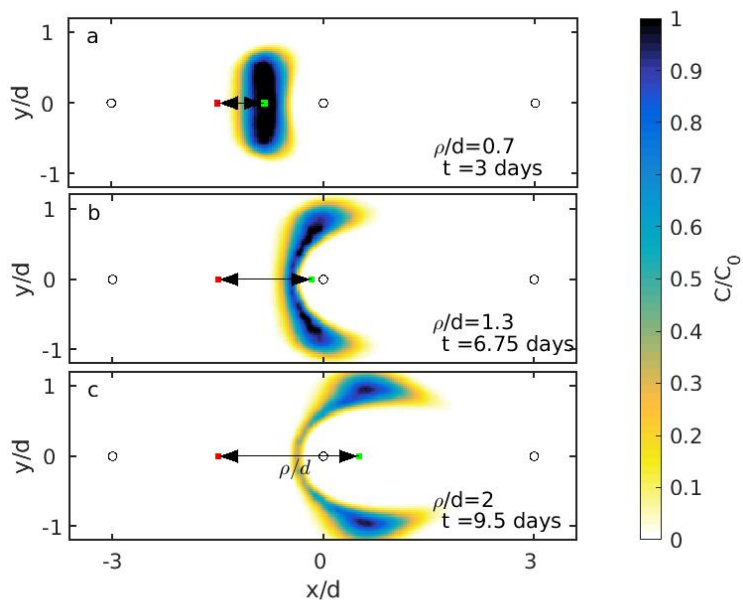

Figure 3.8: Concentration distribution of the solute plume for the stagnation scenario at $\rho/d = 0.7, 1.3, 2$. The red square represents the center of the initial plume, (x_p, y_p), the green square represents the centroid the plume and the distance between them represents the normalized travel distance of the plume ρ/d. The open circles represent the well locations.
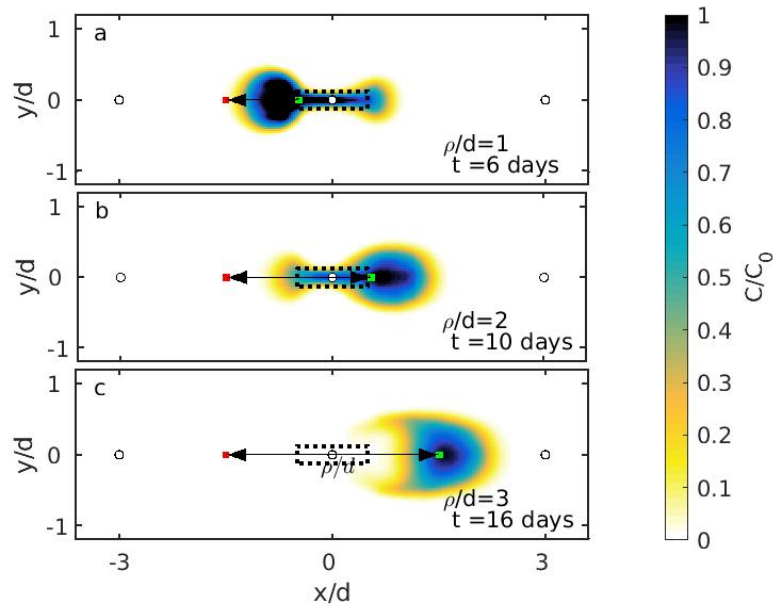
Figure 3.9: Concentration distribution of the solute plume for the passive spreading scenario P3 at $\rho/d = 0.7, 1.3, 2$. The red square represents the center of the initial plume, (x_p, y_p), the green square represents the centroid the plume and the distance between them represents the normalized travel distance of the plume ρ/d. The open circles represent the well locations.

Figure 3.10: Concentration distribution of the solute plume for the passive spreading scenario P8 at $\rho/d = 0.7, 1.3, 2$. The red square represents the center of the initial plume, (x_p, y_p), the green square represents the centroid the plume outside the inclusion and the distance between them represents the normalized travel distance of the plume ρ/d. The open circles represent the well locations.
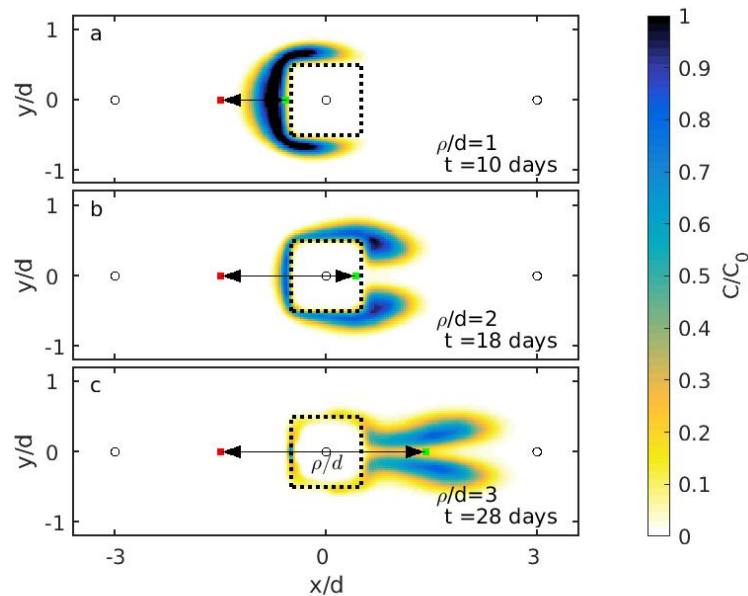
and S_2 that react instantaneously and irreversibly to form species S_3 (i.e.,$S_1 + S_2 \to S_3$). Since the reaction is fast, the rate of change of the cumulative mass of $S1$ that has reacted with $S2$, $M_{\mathrm{R}_{S1}}$, is limited by the flux of S_1, or alternatively S_2, over the interface between the two species (Ottino, 1989), which is expressed by

$$\frac{dM_{\mathrm{R}S1}}{dt} = nb \int_{\Gamma_{\mathrm{Int}}} \frac{\partial C_{s_1}}{\partial \beta} D_\perp d\Gamma_{\mathrm{Int}}, \tag{3.10}$$

where Γ_{Int} is the interface between S_1 and S_2, $\partial C_{S_1}/\partial \beta$ is the concentration gradient of S_1 in the direction β defined as the local outward direction perpendicular to Γ_{Int}, and $D_\perp$ is the component of the dispersion tensor perpendicular to Γ_{Int} (defined below). It follows directly from (3.10) that $M_{\mathrm{R}_{S1}}$ is given by

$$M_{\mathrm{R}S1}(t) = \int_0^t \frac{dM_{\mathrm{R}S1}}{dt} dt'. \tag{3.11}$$

We propose that a similar concept can be applied to conservative (non-reactive) mixing. Specifically, we hypothesize that by measuring the total dispersive mass flow rate across some representative curve along the plume, we can measure the instantaneous rate of mixing over the entire plume. Following the same argument as above, by measuring the cumulative solute mass that disperses across that same representative curve over time, we can measure the evolution of the mixing state of the entire plume. For this study, we select the curve along which the concentration is equal to C^*, where $C^*(t) = 0.5 C_{\max}(t)$ and $C_{\max}(t)$ is the maximum concentration of the plume at time t. We define this curve as Γ_{C^*}, which is depicted for uniform flow at $\rho/d = 2$ in Figure 3.11. Rewriting (3.10) for a conservative species, the total dispersive mass flow rate, $\dot{M}_{\Gamma_{C^*}}$ across Γ_{C^*} is given by

$$\dot{M}_{\Gamma_{C^*}} = \frac{dM_{\Gamma_{C^*}}}{dt} = bn \int_{\Gamma_{C^*}} \frac{\partial C}{\partial \beta} D_\perp d\Gamma_{C^*}, \tag{3.12}$$

where $M_{\Gamma_{C^*}}(t)$ represents the cumulative solute mass that disperses across Γ_{C^*}, and $D_\perp$, the component of the dispersion tensor perpendicular to Γ_{C^*}, has a contribution from longitudinal dispersion that is proportional to the component of velocity perpendicular to Γ_{C^*} and a contribution
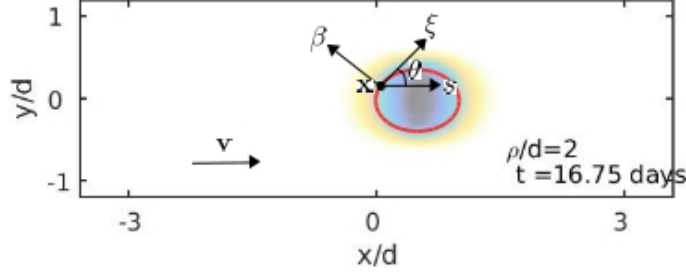
Figure 3.11: Concentration of the plume under uniform flow at $\rho/d = 2$ showing the location of Γ_{C*} (red curve) as well as the directions perpendicular, β, and transverse, ξ, to Γ_{C*} at the point $\mathbf{x}$. Also shown is the angle, θ, between the local flow direction, s, and the ξ direction at $\mathbf{x}$. $\mathbf{v}$ is the local flow velocity vector.

from transverse dispersion that is proportional to the component of velocity parallel to Γ_{C*}, given by

$$D_\perp = \alpha_L \left| \sin\theta(\mathbf{v} \cdot \hat{\mathbf{n}}) \right| + \alpha_T \left| \cos\theta(\mathbf{v} \cdot \hat{\mathbf{z}}) \right|, \tag{3.13}$$

where $\hat{\mathbf{n}}$ and $\hat{\mathbf{z}}$ are unit vectors in the directions normal, β, and transverse, ξ, to Γ_{C*}, respectively, and θ is the angle between the local flow direction, s, and the ξ direction as shown in Figure 3.11. It follows directly from (3.12) that

$$M_{\Gamma_{C*}}(t) = \int_0^t \dot{M}_{\Gamma_{C*}} dt'. \tag{3.14}$$

Figure 3.12a shows the evolution of $E(t)/E_0$ for uniform flow, where E_0 is the dilution index of the plume at $t = 0$. Figure 3.12b shows the evolution of $M_{\Gamma_{C*}}(t)/m_0$ for uniform flow, where m_0 is the initial mass of the solute plume. For both Figures 3.12a and b, the x-axis is plotted in terms of $\rho(t)$, normalized by d. The dilution index is a measures for the mixing state of the entire plume while $M_{\Gamma_{C*}}(t)$ is only measuring the mixing behavior along Γ_C^*. However, Figure 3.12 shows that both measures exhibit similar behavior, increasing with ρ at a decreasing rate, supporting the claim that the mixing behavior along Γ_C^*, measured by $M_{\Gamma_{C*}}(t)$ and $\dot{M}_{\Gamma_{C*}}(t)$, can be used to evaluate the overall mixing behavior of the entire plume. Figure 3.12c shows the evolution of $\dot{M}_{\Gamma_{C*}}$ for uniform flow as a function of time (instead of ρ because it is a time derivative). $\dot{M}_{\Gamma_{C*}}$ decreases at a decreasing rate with time.

Now that we have shown that the mixing behavior along Γ_C^* can be used to represent the
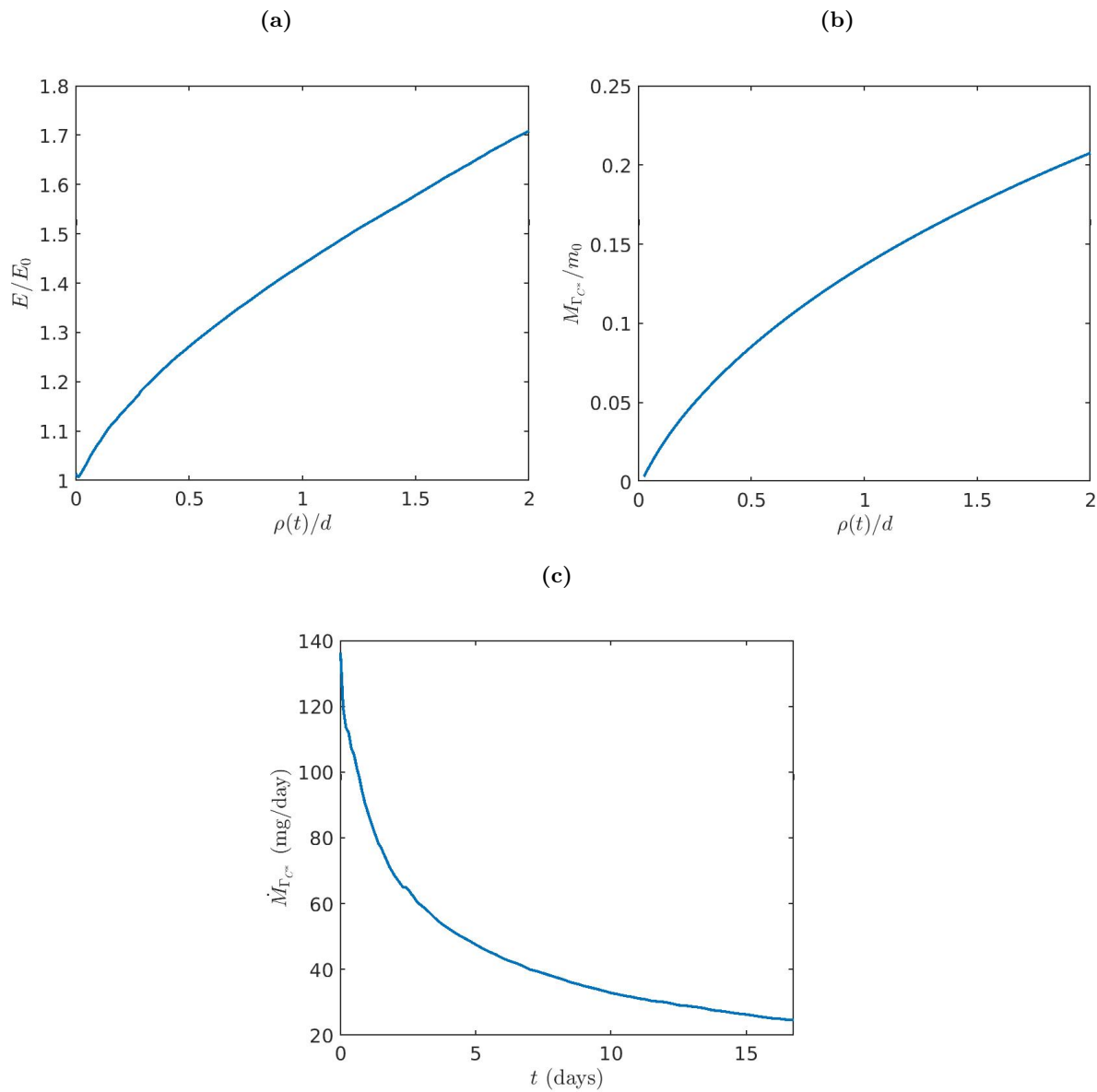
Figure 3.12: Evolution of global measures for uniform flow in a homogeneous aquifer. (a) Normalize dilution index, $E(t)/E_0$, and (b) Cumulative solute mass dispersed across Γ_{C^*}, $M_{\Gamma_{C^*}}(t)/m_0$, and (c) Dispersive mass flow rate, $\dot{M}_{\Gamma_{C^*}}$, across Γ_{C^*}.

plume as a whole, we can examine the local behavior in space and in time of the mechanisms along Γ_{C^*} that control both $\dot{M}_{\Gamma_{C^*}}$, specifically, $\partial C/\partial \beta$ and $D_\perp$, to understand the global mixing behavior of the plume as a whole.

3.4.2   Local Measures

To evaluate the local mixing behavior, we use the concentration gradient, $\partial C/\partial \beta$, and the component of the dispersion coefficient perpendicular to Γ_{C^*}, $D_\perp$. The product of these two measures is proportional to the dispersive mass flux across Γ_{C^*} (3.12). Thus, they are a direct measure for mixing at a specific point along Γ_{C^*}.

Since the goal of this paper is to determine how the spreading of the solute plume under different scenarios affects mixing enhancement, in addition to the local mixing measures described above, we also evaluate the local spreading along Γ_{C^*} using the instantaneous strain, ζ, along Γ_{C^*} given by

$$\zeta = \frac{d\ell}{dt}\frac{\triangle t}{\ell}, \tag{3.15}$$

where ℓ is the length of a small arc of Γ_{C^*} and $\triangle t$ is the time interval over which the strain is calculated. Since the instantaneous strain depends on advection only and not dispersion, it is a direct measure of spreading (Zhang et al., 2009).

Figure 3.13 shows the local spreading measure, ζ, as well as both the local mixing measures, $\partial C/\partial \beta$ and $D_\perp$, for uniform flow along Γ_{C^*} at $\rho/d = 0.7, 1.3, 2$. At any given time, the strain is zero along the entire length of Γ_{C^*} since uniform flow has no spatial variability of velocity, which is necessary to produce spreading. At a given point in time, $\partial C/\partial \beta$ is highest for the northern and southern extremes of Γ_{C^*} and lowest for the eastern and western extremes. At a given point along Γ_{C^*}, $\partial C/\partial \beta$ decreases over time, as dispersion smooths the plume. To compare the difference in rate of decrease of $\partial C/\partial \beta$ along Γ_{C^*}, we plot $\partial C/\partial \beta$, with respect to ρ/d for both the western most point and the northern most point of Γ_{C^*} (Figure 3.14). The values of $\partial C/\partial \beta$ for both locations start out roughly the same at $\rho/d = 0$. However, $\partial C/\partial \beta$ initially decreases more rapidly for the
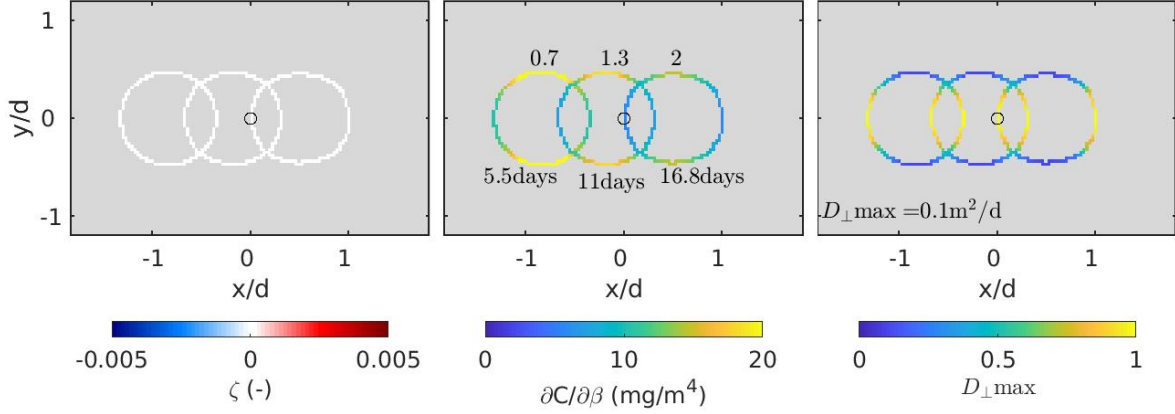
Figure 3.13: Evolution of local measures for uniform flow in a homogeneous aquifer. (a)Instantaneous strain, ζ, (b) $\partial C/\partial \beta$, and (c) The component of the dispersion coefficient perpendicular to Γ_{C*}, $D_\perp$. Arrow denotes direction of flow and the open circle represents the location of the center well. On the middle figure, the value of ρ/d is listed above each curve while the time is listed below.

western most point than the northern most point of Γ_{C*}.

The difference in the rate of decrease in $\partial C/\partial \beta$ between the two locations is due to the difference in $D_\perp$ at the two locations. At any given time, $D_\perp$ is highest along the eastern and western extremes of Γ_{C*} and lowest along the northern and souther extremes. Since longitudinal dispersivity is higher than transverse dispersivity, $D_\perp$ is higher where Γ_{C*} is perpendicular to velocity because longitudinal dispersion dominates in those regions and lower where Γ_{C*} is parallel to velocity because transverse dispersion dominates in those regions. Subsequently, regions where $D_\perp$ is higher, the dispersive mass flux across Γ_{C*} is higher, resulting in a faster rate of decrease of $\partial C/\partial \beta$. As a result, as seen from Figure 3.13b and c for uniform flow, the regions where $D_\perp$ is highest, $\partial C/\partial \beta$ is lowest and the regions where $D_\perp$ is lowest, $\partial C/\partial \beta$ is highest.

3.5   The Effects of Active Spreading Alone

In this section, we evaluate the global and local measures for the five active spreading scenarios described in Table 3.1 and Figures 3.2. We compare the evolution of $E(t)$ and $M_{\Gamma_{C*}}(t)$ to that obtained with uniform flow to evaluate the degree of mixing enhancement obtained by the active
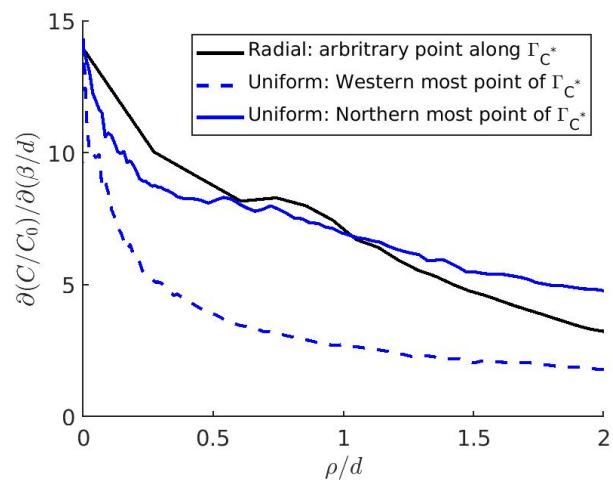
Figure 3.14: The derivative of C/C_0 in the β-direction, $\partial C/\partial \beta$, plotted with respect to ρ/d for the radial scenario (black line) and uniform flow (blue lines)

spreading scenarios. We use $\dot{M}_{\Gamma_{C^*}}$ as well as the local measures, evaluated along Γ_{C^*}, to explain the varying degrees of mixing between scenarios.

3.5.1   Global Analysis

The evolution of the global mixing measures, $E(t)/E_0$ and $M_{\Gamma_{C^*}}(t)/m_0$, with respect to ρ/d are shown in Figures 3.15a and b. For the active spreading scenarios, we compare the amount of mixing after the plume has traveled a normalized travel distance of $\rho/d = 2$. Given that the plume samples different velocities magnitudes in different scenarios, the total time to reach $\rho/d = 2$, and therefore the total time available for mixing, T, varied over a large range between scenarios (Table 3.1). The radial scenario has the least amount of time available for reaction ($T = 1.1$ days) while uniform flow has the greatest ($T = 16.75$ days). The second smallest is the dipole scenario ($T = 6.3$ days), followed by the stagnation scenario ($T = 9.5$ days), diverging scenario ($T = 11.5$ days) and then the converging scenario ($T = 15.75$ days).

Both $E(t)$ and $M_{\Gamma_{C^*}}(t)$ show similar mixing behavior which supports our hypothesis that $M_{\Gamma_{C^*}}(t)$ represents the mixing behavior for the entire plume. For both $E(t)$ and $M_{\Gamma_{C^*}}(t)$, all active spreading scenarios grow with time. The radial scenario has the most mixing enhancement, followed by the diverging scenario, the stagnation scenario and then the dipole scenario. The converging scenario has slightly negative mixing enhancement when compared to uniform flow. Also note, when plotted with respect to ρ/d, both $E(t)$ and $M_{\Gamma_{C^*}}(t)$ of the radial scenario are less than uniform flow for $\rho/d < 0.7$.

To better understand the behavior of $E(t)$ and $M_{\Gamma_{C^*}}$, we examine the temporal evolution of the dispersive mass flow rate, $\dot{M}_{\Gamma_{C^*}}$, across Γ_{C^*} (Figure 3.15c). While $E(t)$ and $M_{\Gamma_{C^*}}(t)$ are plotted with respect to ρ/d to allow for comparison between scenarios, since $M_{\Gamma_{C^*}}(t)$ at $\rho/d = 2$ is the integral of $\dot{M}_{\Gamma_{C^*}}$ from $t = 0$ to $t = T$, it is beneficial to see the difference in T between scenarios as well as the difference in $\dot{M}_{\Gamma_{C^*}}$. For all scenarios, $\dot{M}_{\Gamma_{C^*}}$ decreases at a decreasing rate. However, the initial $\dot{M}_{\Gamma_{C^*}}$ varies between scenarios. The radial scenario has the highest initial $\dot{M}_{\Gamma_{C^*}}$ by an order of magnitude of the other scenarios. The dipole, stagnating and diverging scenarios all have

(a)

(b)

(c)
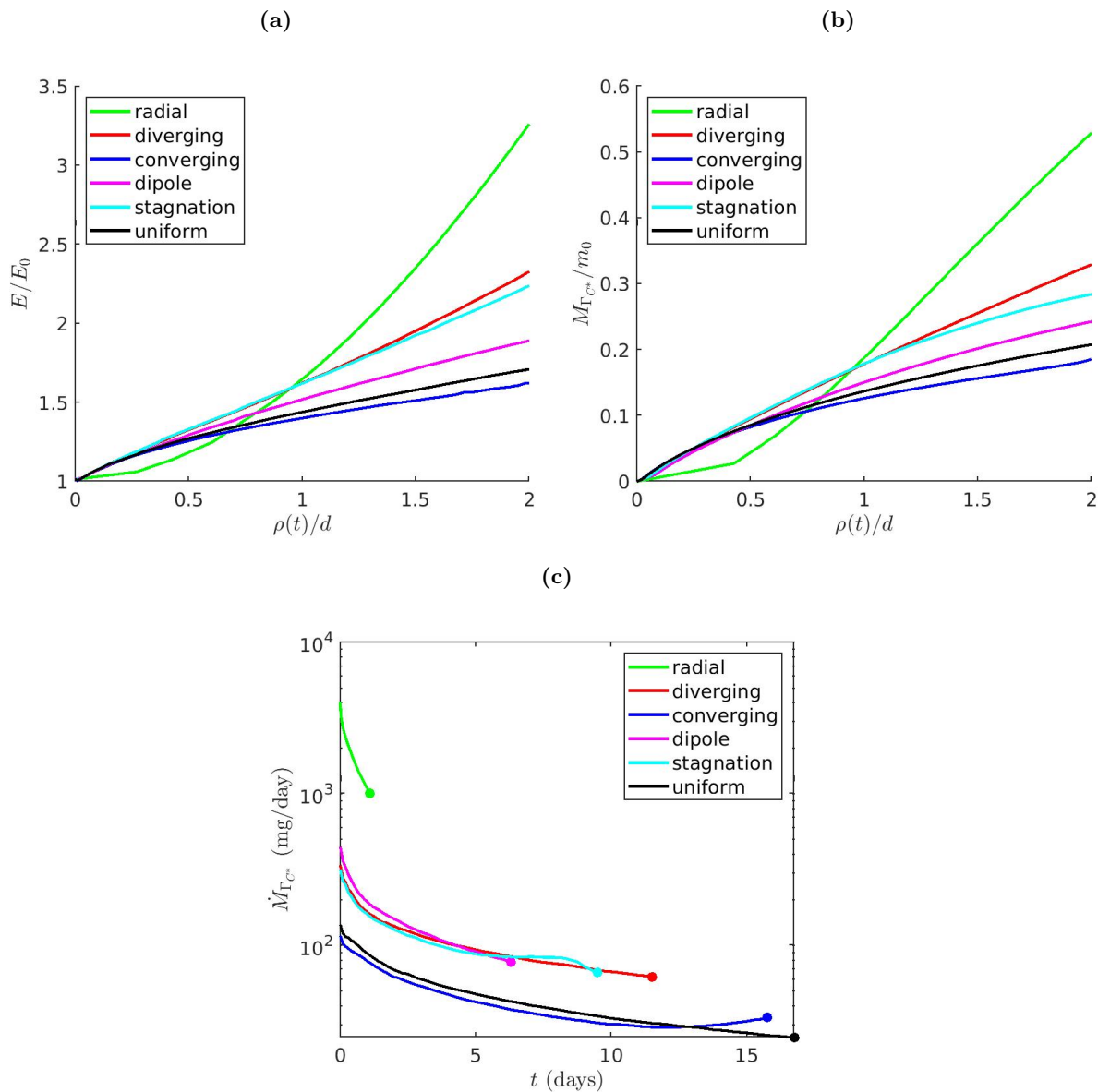
Figure 3.15: Evolution of global measures for the active spreading scenarios. (a) Normalize dilution index, $E(t)/E_0$, and (b) Cumulative solute mass dispersed across Γ_{C^*}, $M_{\Gamma_{C^*}}(t)/m_0$, and (c) Dispersive mass flow rate, $\dot{M}_{\Gamma_{C^*}}$, across Γ_{C^*}. The filled in circles are included to help distinguish where each scenario ends.

similar initial $\dot{M}_{\Gamma_{C*}}$ values while the initial $\dot{M}_{\Gamma_{C*}}$ for the converging scenario is slightly less than uniform flow.

The differences in T as well as initial $\dot{M}_{\Gamma_{C*}}$ explain the varying degrees of mixing enhancement shown in Figures 3.15a and b. While the radial scenario has the shortest T, the initial magnitude of $\dot{M}_{\Gamma_{C*}}$ is large enough compared to the other scenarios that the radial flow scenario has the highest mixing enhancement. As stated above, the diverging, dipole and stagnation scenarios all have similar initial $\dot{M}_{\Gamma_{C*}}$ values as well as similar rates of decrease. Thus, it is the difference in T that explains the different degrees of mixing enhancement. Out of the three scenarios, the diverging scenario has the longest T and thus has the most mixing enhancement after $\rho/d = 2$ while the dipole scenario has the shortest T thus the least amount of mixing enhancement. Lastly, the converging scenario has a similar T as uniform flow but has slightly lower $\dot{M}_{\Gamma_{C*}}$ for nearly all time, which explains why it has negative mixing enhancement compared to uniform flow as seen in Figures 3.15a and b.

3.5.2   Local Analysis

In the previous section, the behavior of $\dot{M}_{\Gamma_{C*}}$ was analyzed to explain the different degrees of mixing enhancement, measured by $E(t)$ and $M_{\Gamma_{C*}}(t)$, between the active spreading scenarios. This section attempts to further that understanding by analyzing locally the effect of active spreading on the behavior of the local mixing measures, $\partial C/\partial \beta$ and $D_\perp$ along Γ_{C*}. Specifically, we identify the effects of active spreading on $\partial C/\partial \beta$ and $D_\perp$ that lead to positive mixing enhancement as well as those that lead to negative mixing enhancement.

As described previously, mixing at a point in space is related to the dispersive mass flux at that point, which in turn, depends on the product of $D_\perp$ and $\partial C/\partial \beta$. Therefore, regions where both $D_\perp$ and $\partial C/\partial \beta$ are high, the amount of mixing will be also be high. Alternatively, where both $D_\perp$ and $\partial C/\partial \beta$ are low, the amount of mixing will also be low. Consequently, to understand how active spreading enhances mixing, we need to understand first how $D_\perp$ and $\partial C/\partial \beta$ affect mixing and second how active spreading can affect the behavior of $D_\perp$ and $\partial C/\partial \beta$ in such way that leads

to enhanced mixing.

The value of $D_\perp$ is based on the orientation of Γ_{C^*} with the local velocity vector (3.13). Since longitudinal dispersivity is usually an order of magnitude more that transverse dispersivity (Sahimi et al., 1986), when Γ_{C^*} is oriented perpendicular to flow, $D_\perp$ will be the maximum for a given velocity. Alternatively when Γ_{C^*} is oriented parallel to flow, $D_\perp$ will be the minimum for a given velocity. Thus, active spreading that reconfigures the plume in such a way that orients Γ_{C^*} perpendicular to the flow direction will enhance mixing.

For flow with no spreading, the rate of decrease of $\partial C/\partial \beta$ at a given point along Γ_{C^*} depends on the value of $D_\perp$. As seen in uniform flow, $\partial C/\partial \beta$ decreases faster for regions of high $D_\perp$ and slower for regions of low $D_\perp$. However, spreading or specifically stretching, can also effect the rate of decrease of $\partial C/\partial \beta$. As a region of a solute plume is stretched, due to conservation of mass, the region perpendicular to the stretching direction is contracted and thus the rate of decrease of $\partial C/\partial \beta$ is slowed. Thus, $\partial C/\partial \beta$ will remain elevated for longer time, which will enhance mixing. Lastly, since mixing occurs along Γ_{C^*}, a longer Γ_{C^*} leads to a larger area available for mixing. Since stretching along Γ_{C^*} increases the length of Γ_{C^*}, stretching can enhance mixing in this way as well.

Figures 3.16a,b and c show the local measures for radial flow at $\rho/d=0.7,1.3$ and 2. All three measures are uniform along Γ_{C^*} and decrease with time. The instantaneous strain rate, ζ, is positive which signifies that Γ_{C^*} is being stretched thus increasing in length. To see the effect of stretching on the rate of decrease of $\partial C/\partial \beta$, Figure 3.14 plots $\partial C/\partial \beta$, with respect to ρ/d for the radial scenario alongside both the western most point and the northern most point of Γ_{C^*} for uniform flow. As expected, $\partial C/\partial \beta$ decreases at a decreasing rate for all three cases shown. However, for the radial scenario, $\partial C/\partial \beta$ is higher than both locations for uniform flow for $\rho/d < 1$ and higher than the western most point for uniform flow for all ρ/d. Although the maximum $D_\perp$ is larger in the radial scenario than uniform flow (from Figure 3.16c), the decrease in $\partial C_B/\partial \beta$ due to dispersion is slowed by the increase in $\partial C_B/\partial \beta$ caused by stretching.

The high values of $D_\perp$ are partly due to the fact that the velocity experienced by the plume
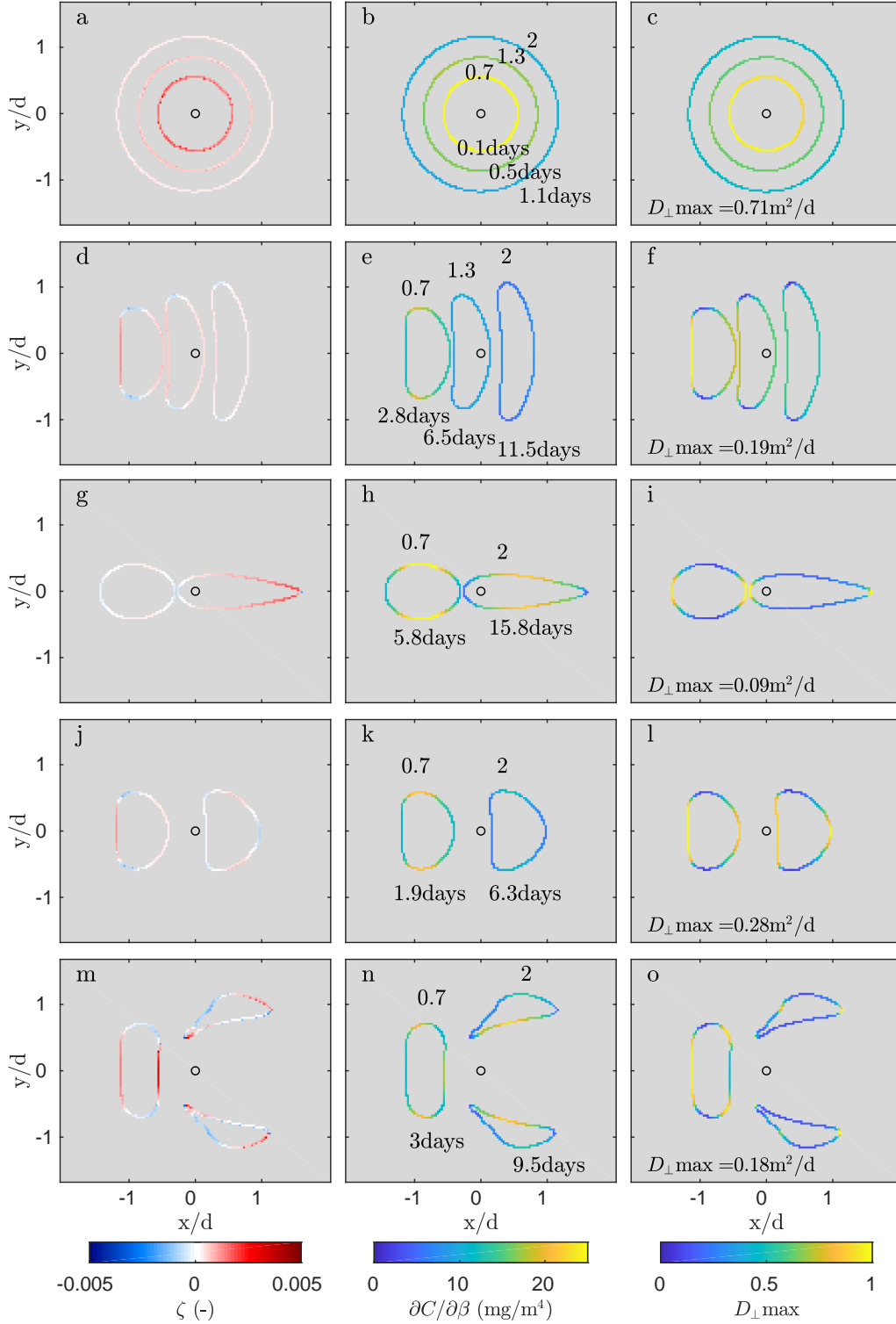
Figure 3.16: Evolution of local measures (Instantaneous strain, ζ $\partial C_B/\partial \beta$, and the component of the dispersion coefficient perpendicular to Γ_{Int}, $D_\perp$) for the active spreading scenarios for $\rho/d = 0.7, 1.3, 2$. The radial scenario is presented in (a),(b) and (c). The diverging scenario in (d),(e) and (f). The converging scenario in (g),(h) and (i). The dipole scenario in (j),(k) and (l), The stagnation scenario in (m),(n) and (o). The open circle represents the location of the Well 2. On the middle figure, the value of ρ/d is listed above each curve while the time is listed below.

is higher than in the other active spreading scenarios. However, it is also because Γ_{C^*} is always perpendicular to the local velocity, so it is the maximum possible for a given velocity. To summarize, the uniform stretching along Γ_{C^*} slows the decrease in $\partial C/\partial \beta$ while the orientation of Γ_{C^*} with the local flow direction ensures the maximum $D_\perp$ for a given velocity all along Γ_{C^*}. The overall effect, as seen in Figures 3.15a and b, is more than 200% enhancement to mixing in the radial scenario over uniform flow.

In contrast to the radial scenario, the remaining active spreading scenarios have regions of stretching ($\zeta > 0$) and contraction ($\zeta < 0$) along Γ_{C^*} as well as regions of high and low $D_\perp$ along Γ_{C^*}. While the same conclusions described above are still applicable, the variation along Γ_{C^*} means that the mixing enhancement will depend on how these regions correspond to each other. Specifically, scenarios where regions of stretching ($\zeta > 0$) which slow the rate of decrease of the gradient as well as increase the area available for mixing correspond to regions of high $D_\perp$ will have more mixing enhancement than scenarios where this is not the case. A good example of this behavior is found in the diverging scenario (Figures 3.16d,e and f), which has the second highest mixing enhancement compared to uniform flow. In the diverging scenario, Γ_{C^*} is stretched north to south while the mean flow direction is west to east. The value of $\zeta > 0$ along the eastern and wester regions and $\zeta < 0$ along the northern and southern regions (Figure 3.16d). The effect of stretching on $\partial C/\partial \beta$ is shown in Figure 3.16e. For regions corresponding to $\zeta > 0$, the rate of decrease in $\partial C/\partial \beta$ is slower compared to the other regions. Additionally, the regions of $\zeta > 0$ also correspond to regions of high $D_\perp$ (Figure 3.16f) for all three values of ρ/d. The overall result is a large amount of mixing enhancement in those regions. Both the dipole (Figure 3.16j,k and l) and the stagnation (Figure 3.16m,n and o) scenarios also have this behavior, although only for $\rho/d = 0.7$, thus, they both have less mixing enhancement than the diverging scenario.

When, instead, regions of low $D_\perp$ correspond to regions of stretching ($\zeta > 0$), the enhancement to mixing caused by the stretching is less than it would be if those regions corresponded to higher $D_\perp$ because even though the stretching will slow the decrease of $\partial C/\partial \beta$ the low $D_\perp$ limits the amount of mixing enhancement. Additionally, when regions of high $D_\perp$ correspond to regions

of contraction ($\zeta < 0$), the enhancement to mixing caused by high $D_\perp$ is less than it would be if those regions corresponded to regions of stretching ($\zeta > 0$) because the high $D_\perp$ values will cause $\partial C/\partial \beta$ to decrease rapidly thus limiting the effect of the $D_\perp$ values. A good example of this behavior is found in the converging scenario (Figures 3.16g,h and i), which has slightly negative mixing enhancement when compared to uniform flow. For the converging scenario, both the direction of plume stretch and the direction of mean flow are in the west to east direction. In consequence, the regions of $\zeta < 0$ (Figure 3.16g) correspond to the regions of high $D_\perp$ (Figure 3.16i) and the regions of $\zeta > 0$ correspond to the regions of low $D_\perp$, for all ρ/d. Notice that the rate of decrease of the gradient for regions of $\zeta > 0$ is slowed as a result of the stretching but the overall mixing enhancement is limited due to the low $D_\perp$ values. This behavior is also observed, for $\rho/d = 2$, in both the dipole (Figure 3.16j,k,l) and the stagnation (Figure 3.16m,n,o) scenarios. Thus, while the dipole and stagnation scenarios have more mixing enhancement than the converging flow scenario, they have less than the radial and diverging scenarios.

3.6   The Effects of Passive Spreading Alone

In this section, we evaluate the global and local measures for the eight passive spreading scenarios described in Table 3.2 and Figure 3.1. We compare the evolution of the global measures to that obtained with uniform flow to evaluate the degree of mixing enhancement obtained by the passive spreading scenarios. We use the local measures, evaluated along Γ_{C^*}, to demonstrate the mechanism that control the degree of mixing enhancement. We ran four scenarios (P1-P4) with $K/K_{\text{inc}} > 1$ and four scenarios (P5-P8) with $K/K_{\text{inc}} < 1$. For the scenarios with $K/K_{\text{inc}} > 1$, P1 and P2 have $K/K_{\text{inc}} = 10$ and P3 and P4 have $K/K_{\text{inc}} = 100$. P1 and P3 have an inclusion width, $w/d = 0.25$ while P2 and P4 have an inclusion width, $w/d = 0.5$. For the scenarios with $K/K_{\text{inc}} > 1$, P5 and P6 have $K/K_{\text{inc}} = 0.1$ and P7 and P8 have $K/K_{\text{inc}} = .01$. P5 and P7 have an inclusion width, $w/d = 0.5$ while P6 and P8 have an inclusion width, $w/d = 1$.

3.6.1   Passive Scenarios with $K/K_{\text{inc}} > 1$ (P1-P4): Global Analysis

The evolution of the global mixing measures, $E(t)$ and $M_{\Gamma_{C^*}}(t)$, with respect to ρ/d, for P1-P4 are shown in Figures 3.17a and b. For all scenarios, both $E(t)$ and $M_{\Gamma_{C^*}}(t)$ increase at a decreasing rate. For both measures, P3 has the highest positive mixing enhancement while P2 has the highest negative mixing enhancement compared to uniform flow. The other two scenarios, P1 and P3, have similar mixing behavior to uniform flow. The fact that $M_{\Gamma_{C^*}}(t)$ has similar behavior to $E(t)$ shows that the mixing behavior along Γ_{C^*} is representative of the mixing behavior of the plume as a whole.

The dispersive mass flow rate along Γ_{C^*}, $\dot{M}_{\Gamma_{C^*}}$, with respect to t, for scenarios P1-P4, is shown in Figure 3.17c. For all passive spreading scenarios, $\dot{M}_{\Gamma_{C^*}}$ decreases at a decreasing rate, except during the time when the plume is interacting with the inclusion (between about $t = 4$ days and $t = 10$ days). When the plume begins to interact with the inclusion, $\dot{M}_{\Gamma_{C^*}}$ increases. Near $t = 7.5$ days, $\dot{M}_{\Gamma_{C^*}}$ reaches a maximum, decreases rapidly until it slightly undershoots the $\dot{M}_{\Gamma_{C^*}}$ curve for uniform flow, and then asymptotically approaches it.

The degree of increase in $\dot{M}_{\Gamma_{C^*}}$ is related to both the width, w/d, and the hydraulic conductivity ratio, K/K_{inc}. For a fixed w, $\dot{M}_{\Gamma_{C^*}}$ increases more for the scenario with the larger K/K_{inc}. For a fixed K/K_{inc}, $\dot{M}_{\Gamma_{C^*}}$ increases more for the scenario with smaller w.

Similar to the active spreading scenarios, since the plume samples different velocities magnitudes depending on K_{inc}, the total time to reach $\rho/d = 3$, and therefore the total time available for mixing, T, varied between scenarios (Table 3.2). For scenarios with high K/K_{inc} (P3 and P4), $T = 16$ days while for the scenarios with lower K/K_{inc} (P1 and P2), $T = 18$ days. As a result, even though $\dot{M}_{\Gamma_{C^*}}$ is higher while the plume is traveling through the inclusion, the higher velocity in the inclusion reduces the travel time and therefore reduces the time available for mixing when compared to uniform flow ($T = 24$ days). For P2, which has the larger inclusion width and smaller K/K_{inc}, the increase in $\dot{M}_{\Gamma_{C^*}}$ was not sufficient to overcome the decrease in travel time, resulting in negative enhancement to mixing. For P1 and P3, the increase in $\dot{M}_{\Gamma_{C^*}}$ was similar to the de-
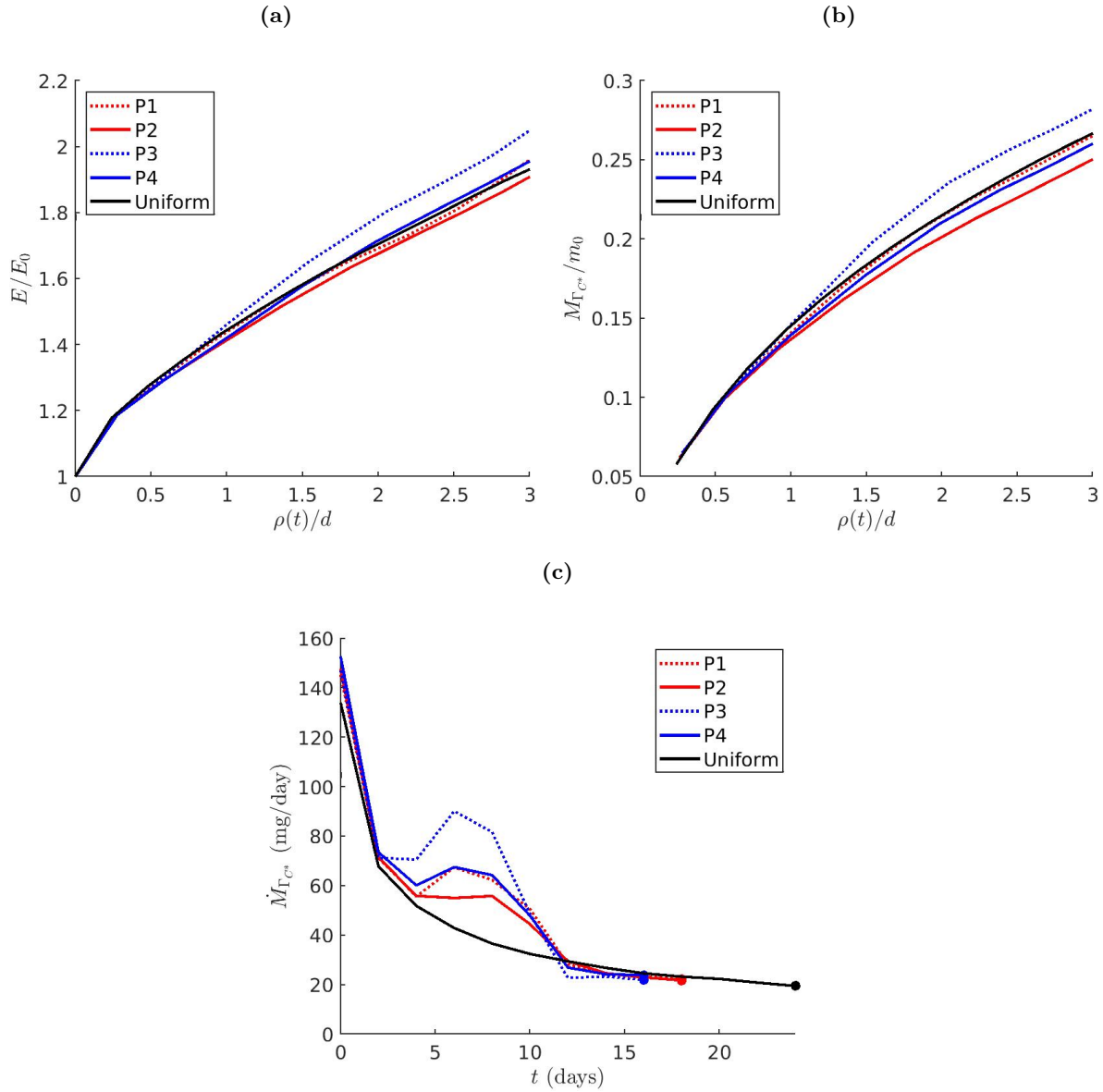
Figure 3.17: Evolution of global measures for the passive spreading scenarios P1-P4. (a) Normalize dilution index, $E(t)/E_0$, and (b) Cumulative solute mass dispersed across Γ_{C^*}, $M_{\Gamma_{C^*}}(t)/m_0$, and (c) Dispersive mass flow rate, $\dot{M}_{\Gamma_{C^*}}$, across Γ_{C^*}. Lines with the same colors have the same K/K_{inc} while lines with the same linestyle have the same inclusion width. The filled in circles are included to help distinguish where each scenario ends.

crease in travel time, resulting in no net enhancement to mixing. For P3, which has the smaller inclusion width and larger K/K_{inc}, the increase in $\dot{M}_{\Gamma_{C*}}$ was sufficient to overcome the decrease in travel time, resulting in positive enhancement to mixing. To understand how the passive spreading in these scenarios leads to an elevated $\dot{M}_{\Gamma_{C*}}$ while the plume is interacting with the inclusion is discussed in the next section.

3.6.2   Passive Scenarios with $K/K_{\text{inc}} > 1$ (P1-P4): Local Analysis

The goal of the following local analysis is to understand how the behavior of the local measures lead to the behavior of $\dot{M}_{\Gamma_{C*}}$ seen in Figure 3.17c. Since $\dot{M}_{\Gamma_{C*}}$ is elevated while interacting with the inclusion for all scenarios, we use P3 as an example for the behavior in the other scenarios. Figure 3.18 shows ζ, $\partial C/\partial \beta$, $D_\perp$ along Γ_{C*} for P3 for $\rho/d = 1, 2, 3$. The same conclusions described in section 3.5.2 apply here as well. Regions where both $D_\perp$ and $\partial C/\partial \beta$ are high, the amount of mixing will be also be high. Alternatively, where both $D_\perp$ and $\partial C/\partial \beta$ are low, the amount of mixing will also be low. The specific behavior of each measure is described below.

Figure 3.18a, for all times, shows that, in general, Γ_{C*} stretches ($\zeta > 0$) while entering the inclusion and contracts ($\zeta < 0$) while leaving the inclusion. Figures 3.18b shows that the regions of Γ_{C*} that show stretching correspond to regions of high $\partial C/\partial \beta$. This behavior is exactly what we would expect since, as stated previously, stretching slows the decrease of $\partial C/\partial \beta$. Note, however, that $\partial C/\partial \beta$ for these regions decreases over time. This is why, as seen in Figure 3.17c, $\dot{M}_{\Gamma_{C*}}$ first increases rapidly as the plume enters the inclusion and then decreases more slowly as the plume flows through the inclusion. (Figure 3.17c).

Figure 3.18c shows that, at any given time, $D_\perp$ is higher for regions of Γ_{C*} in the inclusion compared to regions of Γ_{C*} parallel to the flow outside of the inclusion. For regions of Γ_{C*} parallel to the local flow velocity, $D_\perp$ is dominated by transverse dispersion. However, the velocity is higher in the inclusion compared to the surrounding aquifer, thus, $D_\perp$, while not the maximum value along Γ_{C*}, is still at least double (sometimes triple) the value of $D_\perp$ along the other regions of the Γ_{C*} parallel to the flow.
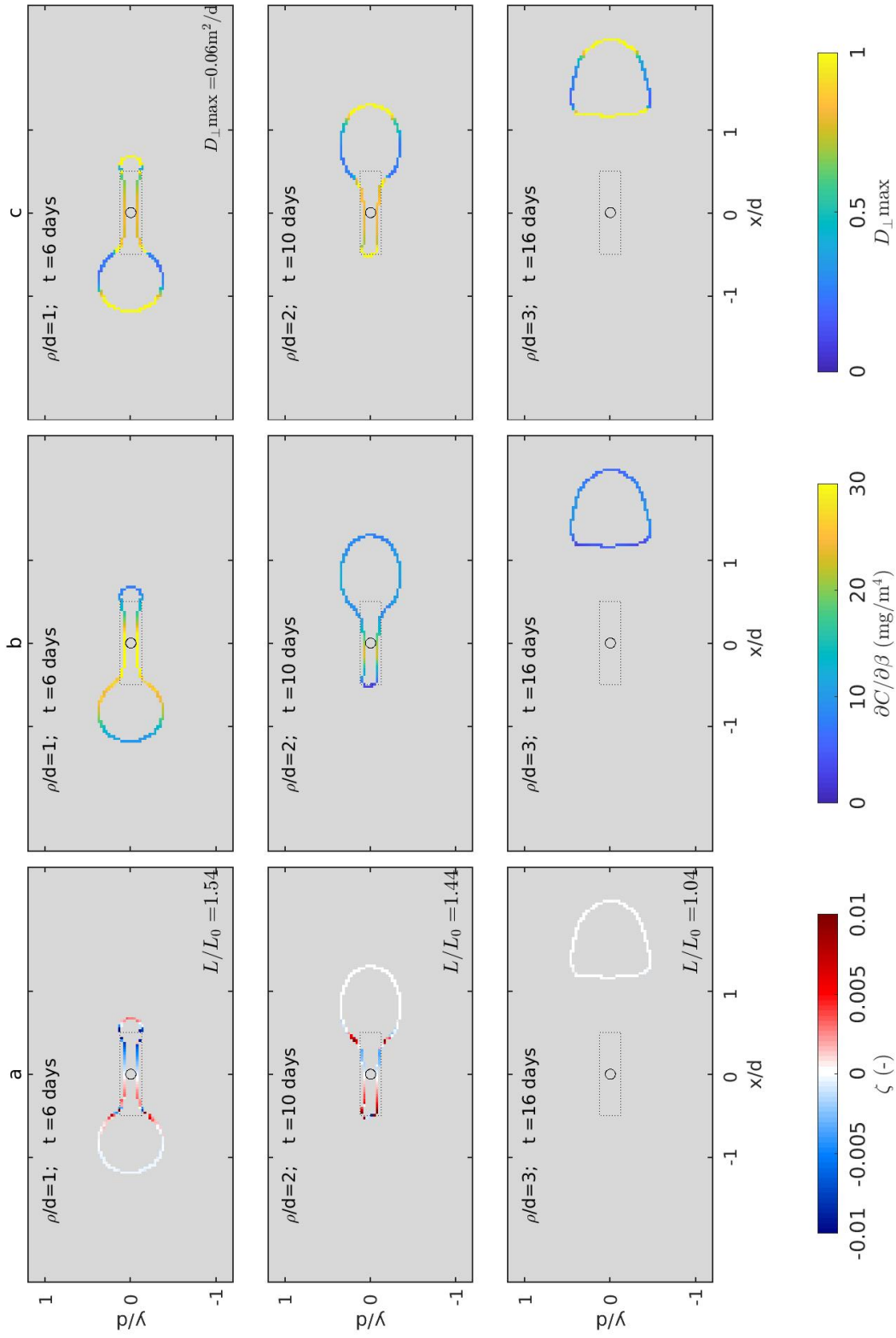
Figure 3.18: Evolution of local measures for the passive spreading scenario P3. (a)Instantaneous strain, ζ, (b) $\partial C/\partial\beta$, and (c) The component of the dispersion coefficient perpendicular to Γ_{C*}, $D_\perp$. The open circle represents the location of the center well.

In summary, the regions of Γ_{C^*} in the inclusion experience stretching (which slows the decrease of $\partial C/\partial \beta$) and high $D_\perp$. Thus, the overall effect is an increase in $\dot{M}_{\Gamma_{C^*}}$ compared to uniform flow while the plume is interacting with the inclusion.

3.6.3   Passive Scenarios with $K/K_{\mathbf{inc}} < 1$ (P5-P8): Global Analysis

The evolution of the global mixing measures, $E(t)/E_0$ and $M_{\Gamma_{C^*}}(t)/m_0$, with respect to ρ, for passive scenarios P5-P8 are shown in Figures 3.19a and b. In contrast to the active spreading and passive spreading scenarios P1-P4, $E(t)$ and $M_{\Gamma_{C^*}}(t)$ show slightly different behavior. For $\rho/d < 2$ both measures increase at a decreasing rate. For $\rho/d > 2$, $E(t)$ increases at and increasing rate for all four passive spreading scenarios. In contrast, for $\rho/d > 2$, $M_{\Gamma_{C^*}}(t)$ increases at an increasing rate for P6, however, continues increasing at a decreasing rate for P5,P7 and P8. One possible explanation is that $E(t)$ is calculated using the whole plume while $M_{\Gamma_{C^*}}(t)$ is only calculated along Γ_{C^*}. Γ_{C^*} is only a representative contour. Thus $M_{\Gamma_{C^*}}(t)$ does not represent mixing behavior that is not experienced by Γ_{C^*}. However, even with the differences in rate of increase, both measures still predict similar mixing enhancement for all scenarios. Both measures are highest for P8 and second highest for P6. Also, both measures show that the mixing enhancement in P5 and P7 is almost identical and that the value is about half the amount of mixing achieved in P8. Thus, even though there are some differences between $E(t)$ and $M_{\Gamma_{C^*}}(t)$, the overall mixing behavior is similar and thus the mixing behavior along Γ_{C^*} can still be used to understand the general mixing behavior of the plume.

The temporal evolution of the dispersive mass flow rate along Γ_{C^*}, $\dot{M}_{\Gamma_{C^*}}$, with respect to t, for scenarios P5-P8, is shown in Figure 3.19c. For all passive spreading scenarios, P5-P8, $\dot{M}_{\Gamma_{C^*}}$ decreases at a decreasing rate, except during the time when the plume is flowing around the inclusion (starting around $t = 6$ days). When the plume begins to interact with the inclusion, $\dot{M}_{\Gamma_{C^*}}$ increases. Near $t = 15$ days, $\dot{M}_{\Gamma_{C^*}}$ reaches a maximum, then slowly decreases.

The degree of increase in $\dot{M}_{\Gamma_{C^*}}$ is related to both w/d and K/K_{inc}. For a fixed K/K_{inc}, $\dot{M}_{\Gamma_{C^*}}$ increases more for the scenario with larger w/d. For a fixed w/d, the behavior differs for different
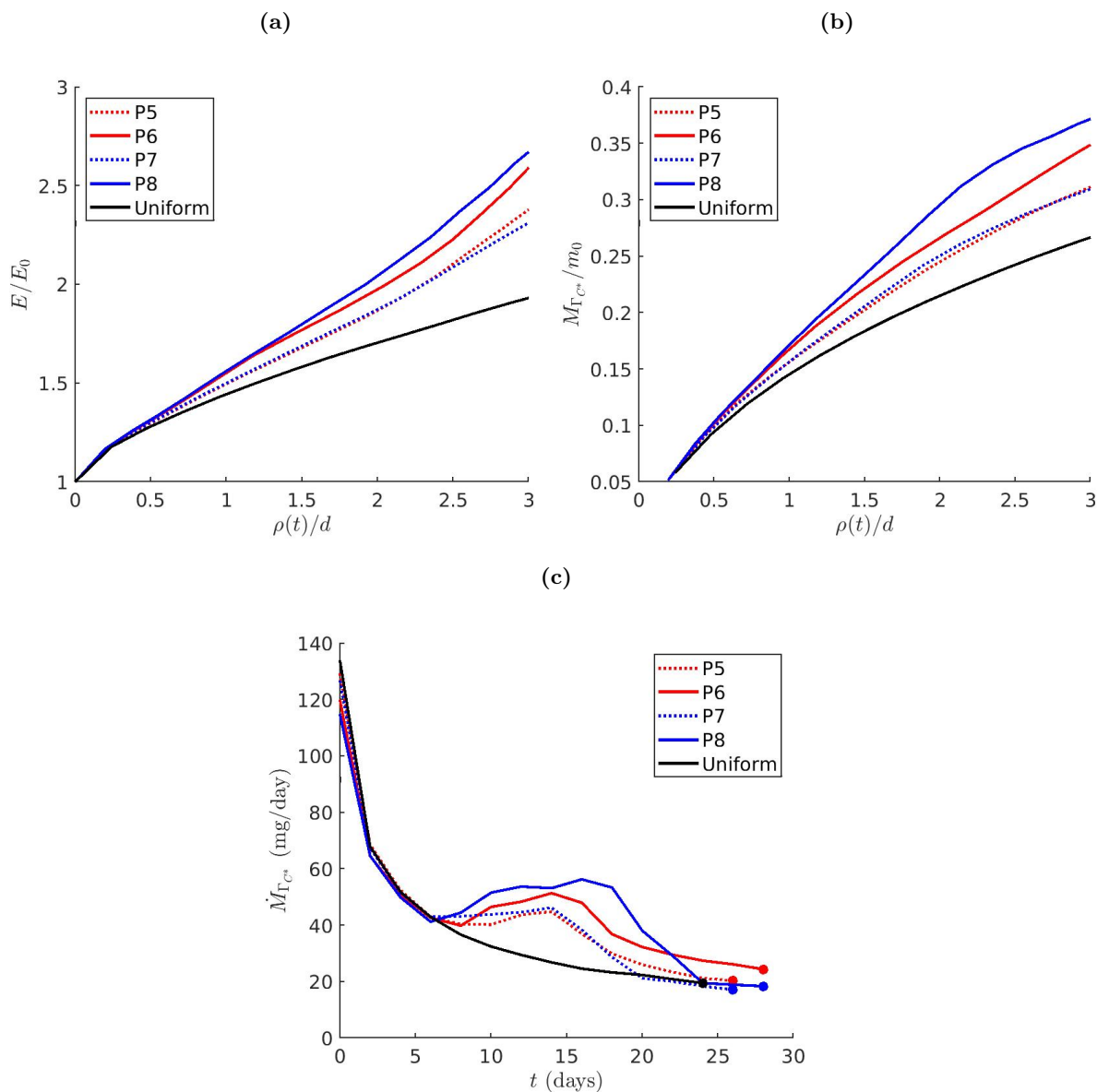
Figure 3.19: Evolution of global measures for the passive spreading scenarios P5-P8.(a) Normalize dilution index, $E(t)/E_0$, and (b) Cumulative solute mass dispersed across Γ_{C*}, $M_{\Gamma_{C*}}(t)/m_0$, and (c) Dispersive mass flow rate, $\dot{M}_{\Gamma_{C*}}$, across Γ_{C*}. Lines with the same colors have the same K/K_{inc} while lines with the same linestyle have the same inclusion width. The filled in circles are included to help distinguish where each scenario ends.

K/K_{inc}. For $w/d = 0.5$ (P5 and P7), both scenarios have similar increases in $\dot{M}_{\Gamma_{C^*}}$. Although, $\dot{M}_{\Gamma_{C^*}}$ increases faster before the local maximum in P7 and then decreases slower after the local maximum in P5. The overall result is that the global mixing behavior is very similar for both scenarios (Figures 3.19a and b). For $w/d = 1$ (P6 and P8), $\dot{M}_{\Gamma_{C^*}}$ is greater for the scenario with $K/K_{\text{inc}} = 0.01$ (P8) for all time $t < 22$ days. For times $t > 22$ days, $\dot{M}_{\Gamma_{C^*}}$ is greater for P6. The overall results is that P8 has more mixing enhancement than P6 (Figures 3.19a and b). Note above that we did not discuss the effect of T on the overall mixing behavior. Why $\dot{M}_{\Gamma_{C^*}}$ is elevated, in particular why the amount of increase in $\dot{M}_{\Gamma_{C^*}}$ as well as the differences in rate of decrease after the local maximum differ between scenarios, is discussed in the next section.

3.6.4 Passive Scenarios with $K/K_{\text{inc}} < 1$ (P5-P8): Local Analysis

The goal of the following local analysis is to explain the behavior of $\dot{M}_{\Gamma_{C^*}}$ seen in Figure 3.19c while the plume is flowing around the inclusion. Since the most signifigant differences occur between scenarios for different K/K_{inc}, we examine P6 (K/K_{inc}=0.1) and P8 (K/K_{inc}=0.01) in detail in this section. Figures 3.20 and 3.21 show ζ, $\partial C/\partial \beta$, and $D_\perp$ along Γ_{C^*} for P6 and P8, respectively, for $\rho/d = 1, 2, 3$. Since the behavior of these measures vary significantly for different values of ρ/d, it is necessary to investigate them at each value of ρ/d to understand how their behavior effects $\dot{M}_{\Gamma_{C^*}}$.

For $\rho/d = 1$ and $t = 10$ days (row 1 of Figures 3.20 and 3.21), Γ_{C^*} has just started to interact with the inclusion. For both scenarios, the west edge of Γ_{C^*} stretches ($\zeta > 0$). Note that this region of stretching corresponds to high $D_\perp$, explaining the initial increase in $\dot{M}_{\Gamma_{C^*}}$. The main difference in the stretching behavior between P6 and P8, is that in P8 the east edge of Γ_{C^*}, the region closest to the west side of the inclusion, also stretches ($\zeta > 0$). This behavior is not present in P6. The difference is that, in P6, K_{inc} is only 10 times lower than K where as in P8 K_{inc} is 100 times lower. The result is that, in P6, a portion of the plume is directed into the inclusion where as in P8, the majority of the plume is directed around the inclusion. Consequently, P6 experiences less stretching than P8 which supports why the increase in $\dot{M}_{\Gamma_{C^*}}$ is higher in P8.
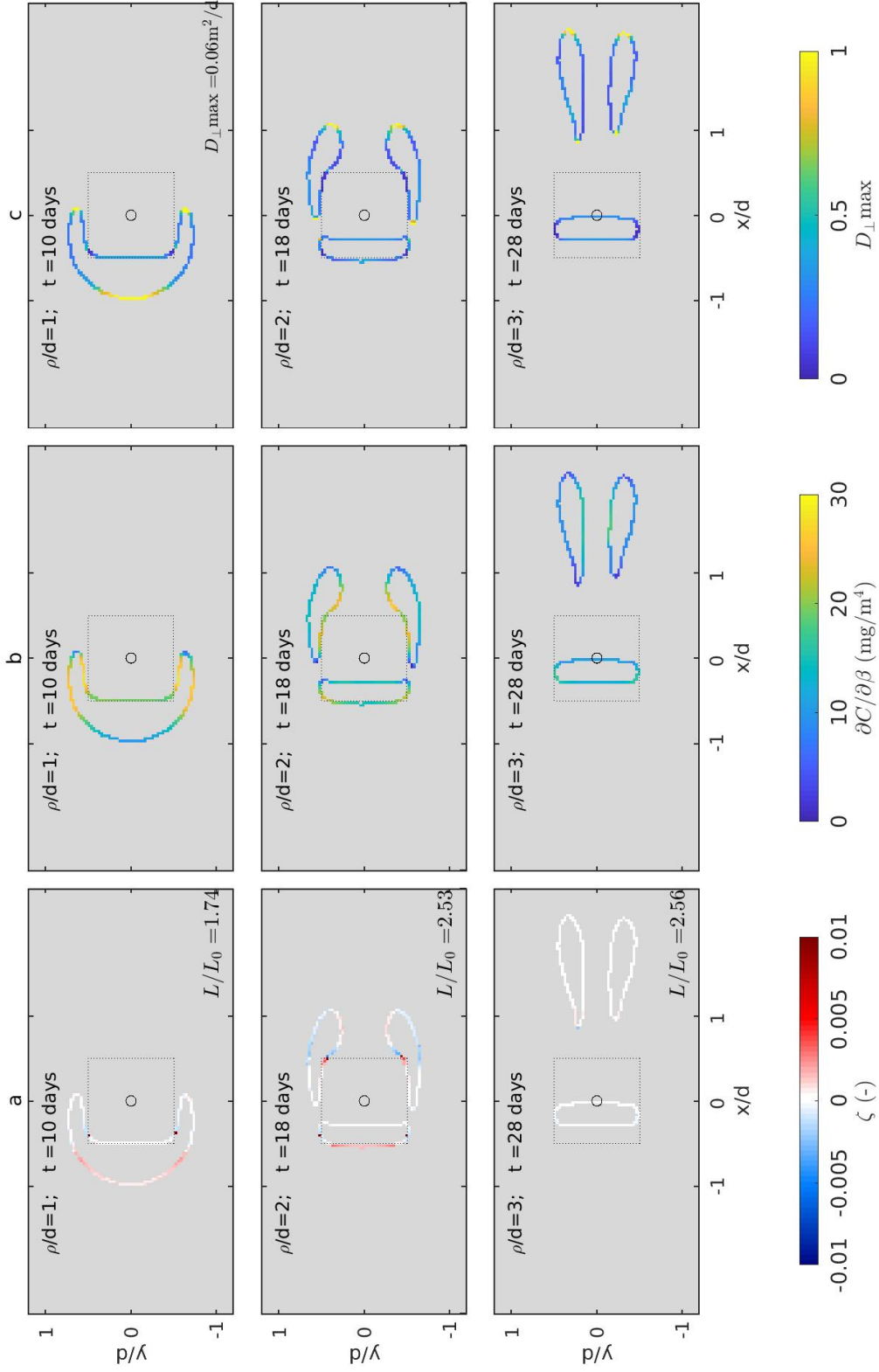
Figure 3.20: Evolution of local measures for the passive spreading scenario P6. (a)Instantaneous strain, ζ, (b) $\partial C/\partial\beta$, and (c) The component of the dispersion coefficient perpendicular to Γ_{C*}, $D_\perp$. The open circle represents the location of the center well.
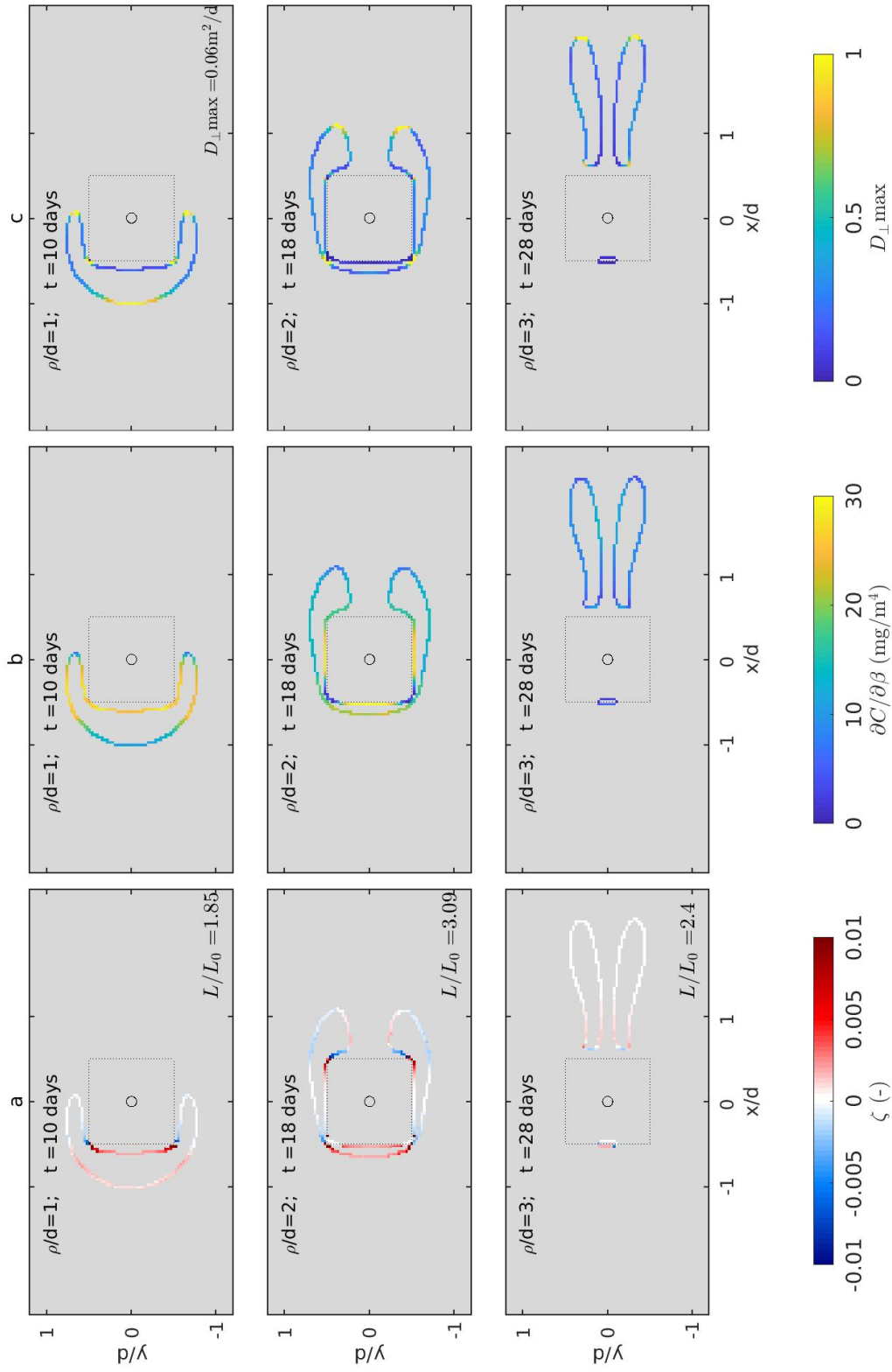
Figure 3.21: Evolution of local measures for the passive spreading scenario P8. (a)Instantaneous strain, ζ, (b) $\partial C/\partial \beta$, and (c) The component of the dispersion coefficient perpendicular to Γ_{C*}, $D_{\perp}$. The open circle represents the location of the center well.
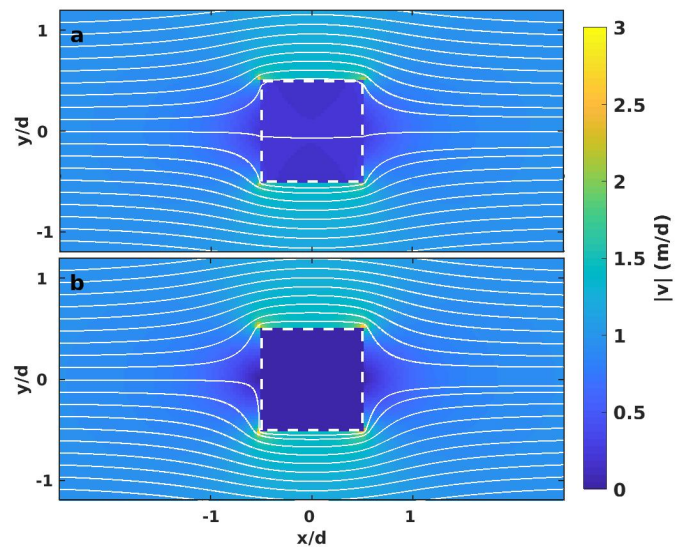
Figure 3.22: The magnitude, $|\mathbf{v}|$, of the velocity field with flow lines (thick black lines), for (a) P6 (b) P8

For $\rho/d = 2$ and $t = 18$ days (row 2 of Figures 3.20 and 3.21), Γ_{C*} is fully stretched around the inclusion. Again, both scenarios show the largest region of stretching is along Γ_{C*} to the west of the inclusion. Notice the value of the gradient in these regions has actually increased compared to $\rho/d = 1$, a direct result of the high sustained stretching. However, unlike for $\rho/d = 1$, these regions of Γ_{C*} now correspond to region of low $D_\perp$. However, $\dot{M}_{\Gamma_{C*}}$ is still elevated above uniform flow for this time. A likely explanation is due to the increase in the length of Γ_{C*}. For P8, the length of Γ_{C*} and thus the area available for mixing has tripled. P6 has a similar, although slightly less, increase as well. So even though $D_\perp$ is low, the increased area for mixing explains the elevated $\dot{M}_{\Gamma_{C*}}$ for this time.

For $\rho/d = 3$ and $t = 22$ days, (row 3 of Figures 3.20 and 3.21), Γ_{C*} is starting to converge east of the inclusion. The degree of convergence depends on both w/d and K/K_{inc}. For a fixed K/K_{inc}, the scenario with the larger width has less convergence because the two lobes are farther apart. For a fixed w/d, the degree of convergence is higher for P8 than P6. Figures 3.22a and b show the flow field for P6 and P8, respectively. The flow lines converge more quickly after the inclusion in P8 than they do in P6. The result is that for both of the scenarios with $K/K_{\mathrm{inc}} = 0.1$ (P5 and P6), $\dot{M}_{\Gamma_{C*}}$ decreases slower than the other scenarios after the local maximum.

Based on the above analysis, the type of spreading and mixing enhancement in passive spreading with $K/K_{\mathrm{inc}} < 1$ is less straight forward than that for the passive spreading with $K/K_{\mathrm{inc}} > 1$. The increase in mixing was in part a result of regions of stretching corresponding to regions of high $D_\perp$ as seen for $\rho/d = 1$, however, it was also due to the relatively large increase in the length of Γ_{C*}, independent of the value of $D_\perp$. Additionally, the amount of convergence of the plume after the inclusion also affected the degree of mixing enhancement.

3.7   The Combined Effect of Active and Passive Spreading

In this section, we investigate the combined effect of active and passive spreading on mixing by performing numerical simulations using the diverging, converging and dipole active spreading scenarios from Section 3.5 combined with the P3 and P8 passive spreading scenarios from Section

3.6. Specifically, we perform the following 5 scenarios: "diverging+P3", "dipole+P3", "converging+P3", "diverging+P8" and "dipole+P8". Unfortunately due an issue with the analysis program, the results for the "converging+P8" scenario are unavailable at this time. However, they will be included when the paper is published. Similar to the active spreading scenarios, each combined scenario was run until $\rho(T)/d = 2$, where the value of T for each scenario varies due to the variation in velocities sampled by the plume.

For each type of active spreading scenario listed above (diverging, dipole and converging), we compare the evolution of $E(t)$ and $M_{\Gamma_{C^*}}(t)$ for the scenarios with passive spreading to that obtained for the active spreading only scenarios to evaluate if a specific combination of active and passive spreading leads to more or less mixing enhancement compared to active spreading alone. Again, we use $\dot{M}_{\Gamma_{C^*}}$ as well as the local measures, evaluated along Γ_{C^*}, to explain the varying degrees of mixing between scenarios.

3.7.1 Global Analysis

Tor the combined active and passive spreading scenarios, the evolution of the global mixing measures, $E(t)/E_0$ and $M_{\Gamma_{C^*}}(t)/m_0$, with respect to ρ/d are shown in Figures 3.23a and b. Both $E(t)$ and $M_{\Gamma_{C^*}}(t)$ show, for the most part, similar mixing behavior which supports our hypothesis that $M_{\Gamma_{C^*}}(t)$ represents the mixing behavior for the entire plume. For both $E(t)$ and $M_{\Gamma_{C^*}}(t)$, all combined active and passive spreading scenarios grow with time.

For the combined diverging scenarios, $E(t)$ shows increased mixing enhancement when combined with P8 and decreased mixing enhancement when combined with P3 compared to the diverging scenario alone. $M_{\Gamma_{C^*}}(t)$ also shows decreased mixing enhancement for the diverging scenario combined with P8, however, it shows no mixing enhancement for the diverging scenario combined with P3. Specifically, for $\rho/d > 1.5$, $M_{\Gamma_{C^*}}(t)$ increases at a decreasing rate while $E(t)$ increases at an increasing rate. For some reason, currently unknown to the authors, the mixing behavior along Γ_{C^*} for this scenario is not representing the mixing behavior of the plume.

For the combined dipole scenarios, both $E(t)$ and $M_{\Gamma_{C^*}}(t)$ show almost identical behavior.
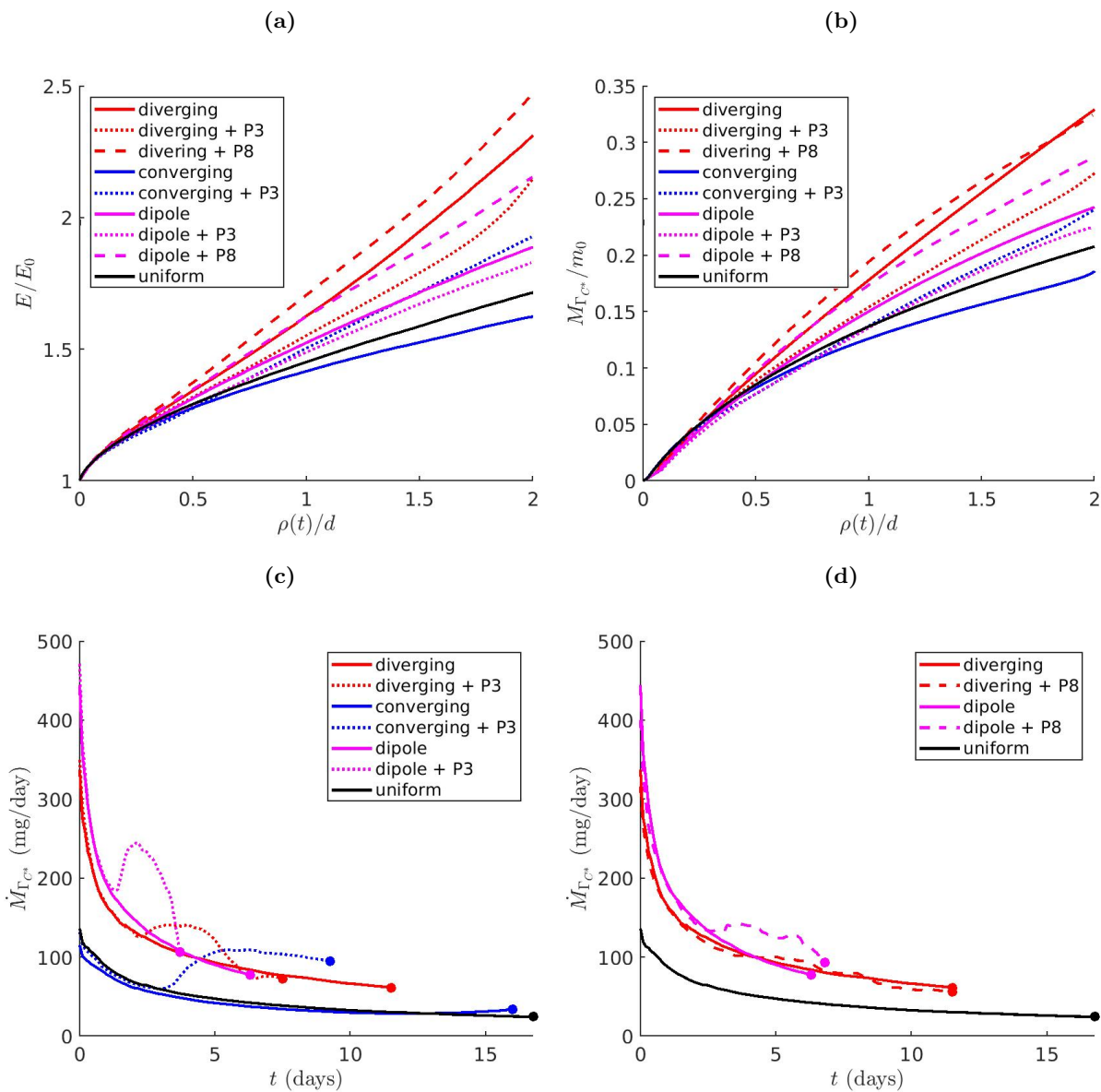
Figure 3.23: Evolution of global measures for the combined active and passive spreading scenarios. (a) Normalize dilution index, $E(t)/E_0$, and (b) Cumulative solute mass dispersed across Γ_{C^*}, $M_{\Gamma_{C^*}}(t)/m_0$, (c) Dispersive mass flow rate, $\dot{M}_{\Gamma_{C^*}}$, across Γ_{C^*} for the P3 scenarios and (d) Dispersive mass flow rate, $\dot{M}_{\Gamma_{C^*}}$, across Γ_{C^*} for the P8 scenarios. Lines with the same colors have the same active spreading. The filled in circles are included to help distinguish where each scenario ends.

Similar to the diverging scenarios, the mixing enhancement is increased when the dipole scenario is combined with P8 and slightly decreased when combined with P3. In contrast to both the combined diverging and combined dipole scenarios, for the combined converging scenarios, both $E(t)$ and $M_{\Gamma_{C^*}}(t)$ show an increase in mixing enhancement when the converging scenario is combined with P3.

To better understand the behavior of $E(t)$ and $M_{\Gamma_{C^*}}$, we examine the temporal evolution of the dispersive mass flow rate, $\dot{M}_{\Gamma_{C^*}}$, across Γ_{C^*}. The combined scenarios with P3 are shown in Figure 3.23c and the combined scenarios with P8 are shown in Figure 3.23d. Each active spreading only scenario is included for comparison. For all three of the combined scenarios with P3, $\dot{M}_{\Gamma_{C^*}}$ decreases at a decreasing rate except for when Γ_{C^*} is interacting with the inclusion. During this time, $\dot{M}_{\Gamma_{C^*}}$ behaves much like it did in the P3 only scenario (Figure 3.17c). However, the amount of time $\dot{M}_{\Gamma_{C^*}}$ is elevated as well as the amount of increase depends on the type of active spreading scenario.

For the "converging+P3" scenario, $\dot{M}_{\Gamma_{C^*}}$ increases around $t = 4$ and remains elevated. Even though the total mixing time for this scenario is $T = 9.5$ days which is shorter than the converging only scenario ($T = 15.75$ days), the increased $\dot{M}_{\Gamma_{C^*}}$ for a sustained period of time leads to an increase in overall mixing enhancement.

For the "dipole+P3" scenario, $\dot{M}_{\Gamma_{C^*}}$ starts to increase around $t = 2$ days, reaches a local maximum around $t = 3$ days and then decreases back to the level achieved by the dipole only scenario around $t = 4$ days where the simulation ends after a total mixing time of $T = 3.7$ days which is about 3 days shorter than the dipole only scenario. Thus, while $\dot{M}_{\Gamma_{C^*}}$ increases when interacting with the inclusion, the decrease in T means there is less time available for mixing, producing a slight decrease in mixing enhancement for the "dipole+P3" scenario when compared the dipole only scenario. The "diverging+P3" scenario is similar to the "dipole+P3" scenario. However, $\dot{M}_{\Gamma_{C^*}}$ increases less while interacting with the inclusion and the decrease in T is higher than the "dipole+P3" scenario. The result is an even larger decrease to mixing enhancement for the "diverging+P3" scenario than was observed for the "dipole+P3" scenario.

For all three of the combined scenarios with P8, the value of $\dot{M}_{\Gamma_{C*}}$ decreases at a decreasing rate except for when Γ_{C*} is interacting with the inclusion. For the "dipole+P8" scenario $\dot{M}_{\Gamma_{C*}}$ behaves much like it did in the P8 only scenario (Figure 3.19c). The value of $\dot{M}_{\Gamma_{C*}}$ starts to increase around $t = 3$ days, reaches a local maximum around $t = 5$ days and then decreases back to the value of the dipole only scenario around $t = 7$ days. The "dipole+P8" scenario is approximately 1 day longer than the dipole only scenario. Thus, $\dot{M}_{\Gamma_{C*}}$ increases while Γ_{C*} is interacting with the inclusion as well as the amount of time available for mixing increases. The overall effect is an increase in mixing enhancement when compared to the dipole only scenario. Different from the "dipole+P8" scenario, the behavior of $\dot{M}_{\Gamma_{C*}}$ for the "diverging+P8" scenario show almost no change from the diverging only scenario. However, as mentioned above, $E(t)$ did show increased mixing enhancement for "diverging+P8". Thus for this case it is not appropriate to use $\dot{M}_{\Gamma_{C*}}$ along Γ_{C*} to understand the global mixing behavior.

3.7.2   Local Analysis

For the local analysis we investigate the "converging+P3" scenario because this combination of active and passive spreading leads to the largest increase in mixing enhancement and the "diverging+P3" scenario because this combination of active and passive spreading leads to the largest decrease in mixing enhancement.

Figures 3.24a,b and c show the local measures for the "converging+P3" scenario at ρ/d=0.7,1.3 and 2. Both the P3 only and converging only scenarios have similar behavior. They both stretch the plume parallel to flow. However, for the converging only scenario, this behavior led to a slightly negative mixing enhancement when compared to uniform flow. This was due to the fact that even though the stretching slowed the rate of decrease of $\partial C/\partial \beta$, $D_\perp$ was low in those regions. In contrast, for the P3 only scenario, the similar stretching behavior led to positive mixing enhancement because the elevated velocities inside the inclusion increased the $D_\perp$ for those regions. For the "converging+P3" scenario, the effect of increased velocity in the inclusion is now applied to the active spreading from the converging scenario as well. The overall effect is that the active and

passive spreading behaviors enhance one another, leading to an increase in mixing enhancement.

Figures 3.25a,b and c show the local measures for the "diverging+P3" scenario at ρ/d=0.7,1.3 and 2. Unlike the "converging+P3" scenario, only a portion of the plume is directed toward the inclusion because the diverging flow and the converging flow are competing against one another. For $\rho/d = 1.3$, while there are regions of high $\partial C/\partial \beta$ along Γ_{C^*} in the inclusion, similar to the P3 only scenario, the corresponding $D_\perp$ is fairly low for those regions compared to the maximum value of $D_\perp$ overall. Additionally, the size of the regions of high $D_\perp$ around Γ_{C^*} for the "converging+P3" scenario are smaller than for those for the diverging scenario alone. It appears that the active spreading and passive spreading behaviors that enhanced mixing in their respective scenarios are competing against one another in the combined scenario, leading to less mixing enhancement than the diverging scenario alone.

3.8   Conclusion

In this study we investigated the relationship between spreading and mixing under non-uniform flow fields typical of EIE remediation systems (active spreading) in aquifers with simple heterogeneity patterns (passive spreading). Independent of the type of spreading, we identified the following behaviors that affect the degree of mixing enhancement:

(1) Scenarios in which regions along Γ_{C^*} where stretching is high correspond to regions where $D_\perp$ is high have a higher dispersive mass flow rate across Γ_{C^*} and therefor a higher rate of mixing. Scenarios in which the opposite occurs experienced a lower rate of mixing.

(2) For scenarios with similar dispersive mass flow rates, the global mixing behavior over a given travel distance is greater for scenarios in which the total time available for mixing is greater.

For active spreading, in both the radial scenario and the diverging scenario, regions of stretching corresponded to regions of high $D_\perp$, resulting in more mixing enhancement in these scenarios compared to the other scenarios. In converging flow, regions of stretching corresponded to regions

Figure 3.24: Evolution of local measures for the combined active and passive spreading scenario "converging+P3". (a)Instantaneous strain, ζ, (b) $\partial C/\partial \beta$, and (c) The component of the dispersion coefficient perpendicular to Γ_{C*}, $D_\perp$. The open circle represents the location of the center well.
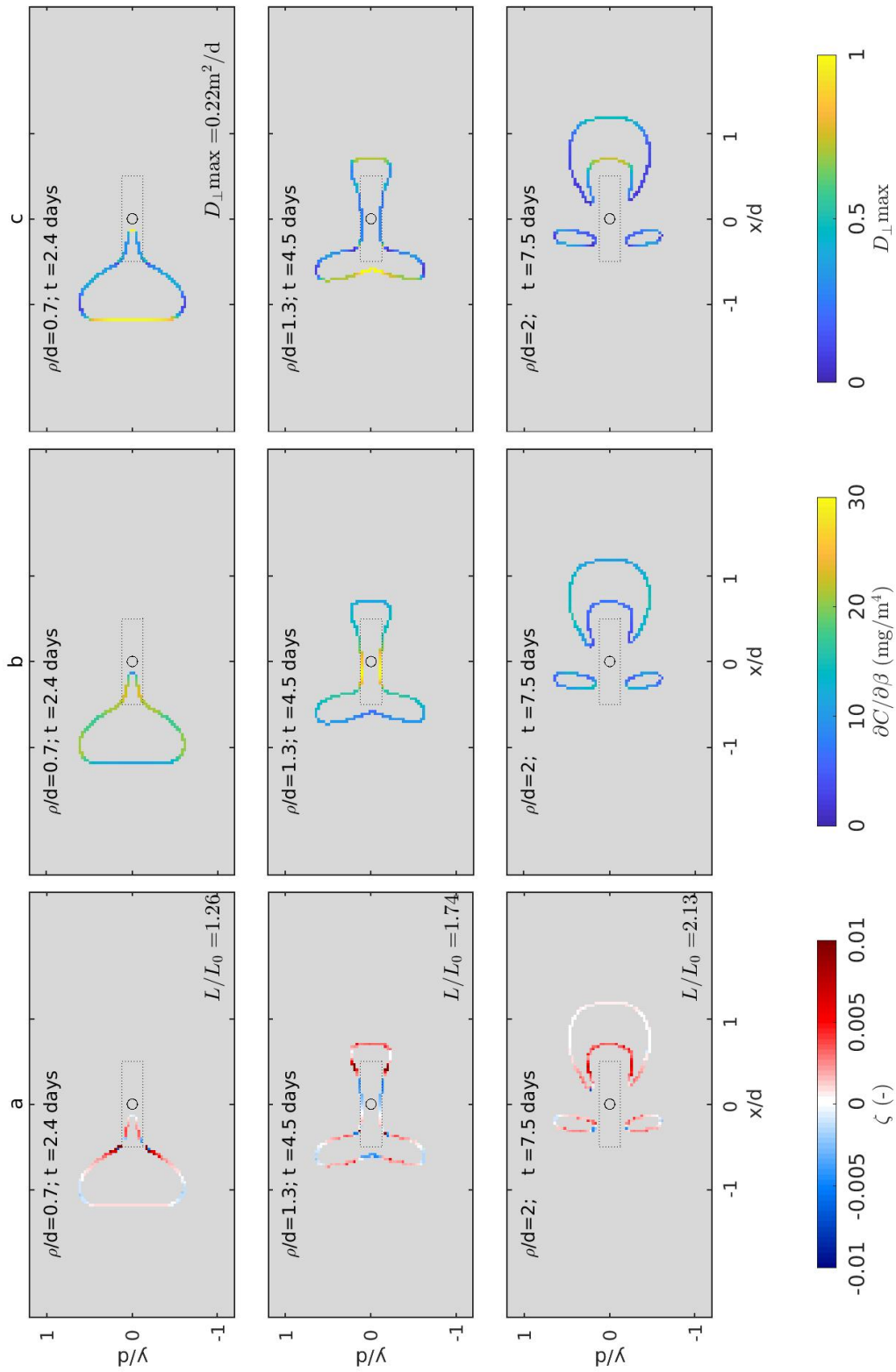
Figure 3.25: Evolution of local measures for the combined active and passive spreading scenario "diverging+P3". (a)Instantaneous strain, ζ, (b) $\partial C/\partial \beta$, and (c) The component of the dispersion coefficient perpendicular to Γ_{C*}, $D_\perp$. The open circle represents the location of the center well.

of low $D_\perp$ and vice versa, resulting in less mixing than uniform flow. The remaining scenarios showed both behaviors at different times, resulting in some mixing enhancement but not as much as the radial and diverging scenarios.

For the passive spreading scenarios where $K/K_{\text{inc}} > 1$, the regions of Γ_{C^*} in the inclusion experienced stretching and high $D_\perp$. Thus, the mixing rate of the plume increased compared to uniform flow while the plume interacted with the inclusion. However, the decreased travel time, due to higher velocities in the inclusion, reduced the time available for mixing compared to uniform flow. Therefore, for a given scenario, mixing was enhanced over a given travel distance when the first effect was stronger than the second.

For the passive spreading scenarios where $K/K_{\text{inc}} < 1$, the degree of mixing enhancement was partly a result of regions of stretching corresponding to regions of high $D_\perp$, however, it was also due to the relatively large increase in the length of Γ_{C^*}, independent of the value of $D_\perp$. Additionally, the amount of convergence of the plume after the inclusion also affected the degree of mixing enhancement.

For combined active and passive spreading, we showed that when the converging active spreading scenario is combined with passive spreading for $K/K_{\text{inc}} > 1$, the behaviors of the converging scenario that negatively enhanced mixing are changed to behaviors that enhanced mixing, resulting in more mixing than in the converging scenario alone. We also showed that when the diverging active spreading scenario is combined with passive spreading $K/K_{\text{inc}} > 1$, the behaviors that enhanced mixing for each scenario alone compete against each other, resulting in a decrease in mixing enhancement compared to the diverging scenario alone.

Chapter 4

Investigating the effects of active spreading on mixing-controlled reaction.

4.1   Introduction

In Chapter 3, we investigated the relationship between spreading and conservative mixing under non-uniform flow fields typical of EIE remediation systems (active spreading) in aquifers with simple heterogeneity patterns (passive spreading). We identified the behaviors of active spreading alone, passive spreading alone, and active and passive spreading combined that positively and negatively enhanced conservative mixing. The goal of this chapter, using a similar approach as in Chapter 3, is to determine how spreading under different active spreading scenarios affects reaction enhancement. Using the same active spreading scenarios from Chapter 3, we identify the active spreading behaviors that positively and negatively enhance reaction. We find that the same behaviors found in Chapter 3 for conservative mixing also apply to mixing-controlled reaction.

4.2   Conceptual Model

The aquifer in this study is assumed to be confined, two-dimensional, isotropic, homogeneous and rectangular in shape bounded by no flow boundaries on the north and south and specified head boundaries on the east and west (Figure 4.1). We assume that ambient flow is negligible. A circular plume of species A with a diameter, d, is located at the center of an annular plume of species B with an outer diameter, $2d$, centered at (x_p, y_p).

The aquifer has three wells, separated by a distance of $3d$. We investigate five active spreading scenarios that represent components of EIE. Schematics of the flow fields are shown in Figure 4.2
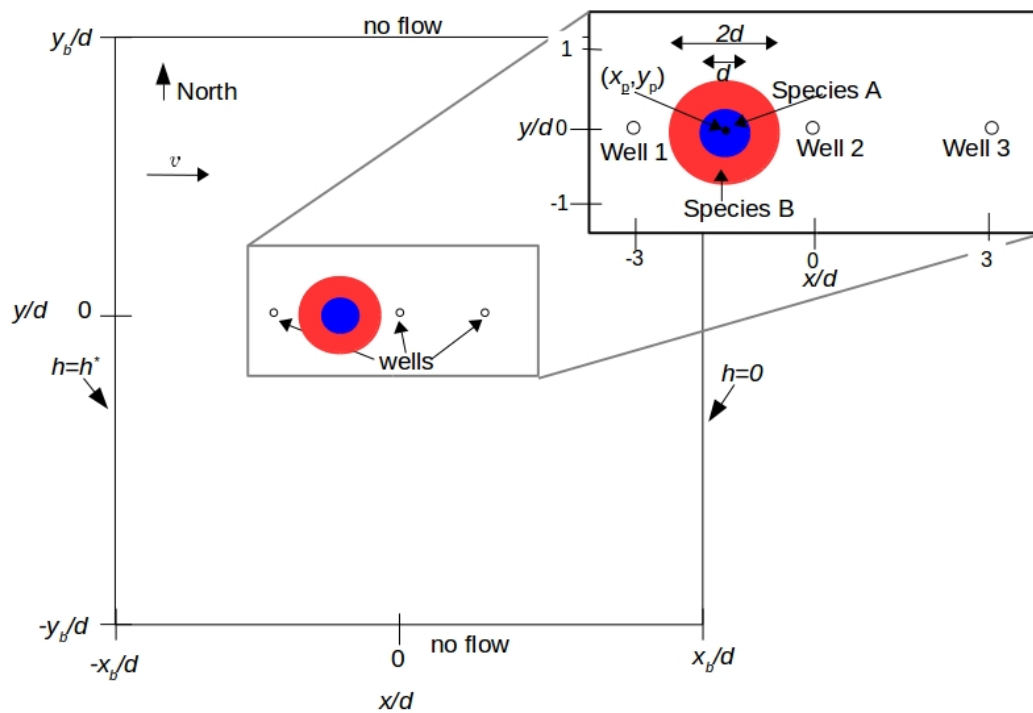
Figure 4.1: Plan view of the model aquifer showing the initial positions of species A (blue) and species B (red) particles. Particles are placed uniformly. Both species A and B plumes are circular, centered at (x_p, y_p) and have diameter d and $2d$, respectively. The small open circles represent the well locations and a north arrow is included. The arrow, labeled with a v, represents the mean direction of ambient flow.

Table 4.1: Details of active spreading scenarios. Total simulation duration, T, and total plume centroid travel distance, $\rho(T)$. Negative injection rates represent extraction.

Scenario Name	Plume center $(x_p/d, y_p/d)$	T (days)	$\rho(T)/d$ (-)	Injection/Extraction Pattern		
				Well 1	Well 2	Well 3
Radial	(0,0)	1.1	2	0	$+Q$	0
Diverging	(-1.5,0)	11.5	2	$+Q$	0	0
Converging	(-1.5,0)	16	2	0	0	$-Q$
Dipole	(-1.5,0)	6.5	2	$+Q$	0	$-Q$
Stagnation	(-1.5,0)	10	2	$+0.8Q$	$+0.2Q$	$-Q$

and details are provided in Table 4.1. In the 'Radial' scenario, a single well at the center of the solute plume injects water into the aquifer, creating a radial flow field (Figure 4.2a). In the 'Diverging' scenario, a single well to the west of the solute plume injects water into the aquifer, creating a diverging flow field (Figure 4.2b). In the 'Converging' scenario, a single well to the east of the solute plume extracts water from the aquifer, creating a converging flow field (Figure 4.2c). The 'Dipole' scenario is the combination of the 'Diverging' and 'Converging' scenarios (Figure 4.2d). The 'Stagnation' scenario is similar to the 'Dipole' scenario except that the injection is distributed over two wells, creating a stagnation point (Figure 4.2e). All active spreading scenarios are compared to uniform flow with a velocity of $\mathbf{v}_u$ in a homogeneous aquifer, which has no active spreading.

4.3   Numerical Model

The governing equation of steady-state groundwater flow for this aquifer is given by

$$0 = \nabla \cdot K \nabla h + \sum_{j=1}^{3} Q_j(t)\delta(\mathbf{x} - \mathbf{x}_j), \tag{4.1}$$

where K is the hydraulic conductivity (here assumed to be isotropic and homogeneous), h is hydraulic head, Q_j is the injection rate in well j, $\mathbf{x} = (x, y)$ is the spatial coordinate, $\mathbf{x}_j$ is the
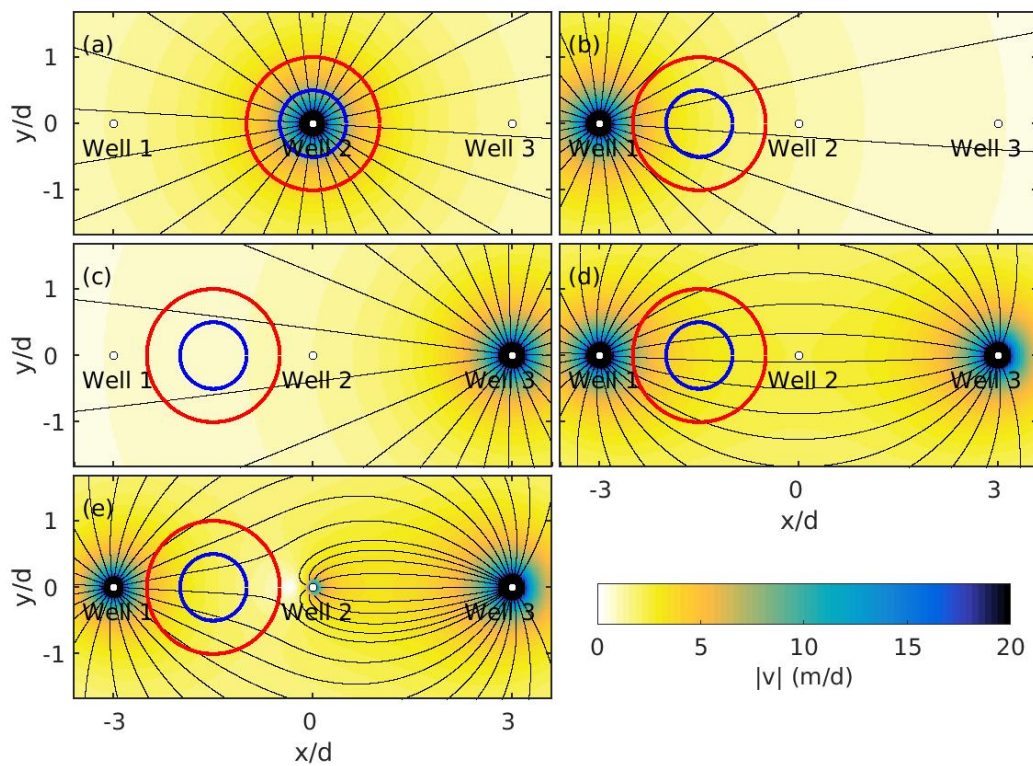
Figure 4.2: The magnitude, $|\mathbf{v}|$, of the velocity field for the active spreading scenarios. (a) 'radial', (b) 'diverging', (c) 'converging', (d) 'dipole' and (e) 'stagnation' active spreading scenarios. Also shown are flow lines (thin black lines), location of the wells (white circles), and the outer radius of the initial plume of species A (blue line) and species B (red line).

location of well j, and $\delta()$ is the Dirac delta function. The boundary conditions are

$$\frac{\partial h}{\partial y} = 0 \text{ at } y = \pm y_b \tag{4.2}$$

$$h = h^* \text{ at } x = -x_b \tag{4.3}$$

$$h = 0 \text{ at } x = x_b, \tag{4.4}$$

The groundwater flow equation (4.1) is solved numerically using MODFLOW, a standard finite difference groundwater flow simulator (Harbaugh et al., 2000). Parameter values are given in Table 4.2.

The transport of species A and B in porous media is governed by the advection-dispersion-reaction equation (ADRE), given by

$$n\frac{\partial C_i}{\partial t} = -\nabla \cdot (n\mathbf{v}C_i) + \nabla \cdot \mathbf{D}n\nabla C_i - R_i, \tag{4.5}$$

where C_i is the concentration of the $i = A$ (Species A) and $i = B$ (Species B) and $i = C$ (Reaction Product), t is time, R_i is the reaction rate of species i, n is porosity, $\mathbf{v}$ is the groundwater velocity vector which comes from Darcy's law, given by $\mathbf{v} = -(K/n)\nabla h$ and $\mathbf{D}$ is the dispersion tensor, with components given by

$$\begin{aligned}
D_{xx} &= \alpha_L \frac{v_x^2}{|\mathbf{v}|} + \alpha_T \frac{v_y^2}{|\mathbf{v}|}, \\
D_{xy} &= D_{yx} = (\alpha_L - \alpha_T)\frac{v_x v_y}{|\mathbf{v}|}, \\
D_{yy} &= \alpha_L \frac{v_y^2}{|\mathbf{v}|} + \alpha_T \frac{v_x^2}{|\mathbf{v}|},
\end{aligned} \tag{4.6}$$

where α_L and α_T are the longitudinal and horizontal transverse dispersivities, respectively, $\alpha_L > \alpha_T$ and the vertical bars denote magnitude.

The chemical reaction takes the form of a bimolecular reaction, given by $A + B \rightarrow C$; thus, $R_A = R_B = -R_C = kC_AC_B$, where k is the reaction rate coefficient. We assume that the reaction is fast relative to the transport time scale, thus $k \rightarrow \infty$.

The initial conditions for (4.5) are given by

$$C_A(\mathbf{x}, 0) = \begin{cases} C_{A0} & \text{for } \sqrt{x^2 + y^2} \leq r_A \\ 0 & \text{otherwise} \end{cases} \tag{4.7}$$

$$C_B(\mathbf{x}, 0) = \begin{cases} C_{B0} & r_A < \sqrt{x^2 + y^2} \leq r_B \\ 0 & \text{otherwise} \end{cases} \tag{4.8}$$

where C_{A0} and C_{B0} are the initial concentration of species A and B, respectively, r_A is the radius of the initial solute plume for species A and r_B is the outer radius of the initial solute plume of species B. The boundary conditions for (4.5) are given by

$$\nabla C_i \cdot \mathbf{n} = 0 \text{ at } x = \pm x_b, y = \pm y_b. \tag{4.9}$$

The transport equation (4.5) is solved numerically using RW3D (Salamon et al., 2006), which uses random walk particle tracking. Particle tracking is a common method for modeling solute transport in aquifers known for its computational efficiency and absence of numerical dispersion (Berkowitz et al., 2006; Le Borgne et al., 2008a,b). Parameter values are given in Table 4.2. The particle positions and masses provided by RW3D were first used to calculate a concentration field by binning the particles. This concentration field was then smoothed using a bivariate local likelihood regression model from the R package locfit(Loader, 2013).

Figures 4.3-4.8 show the simulated plumes at three different times for uniform flow and the five active spreading scenarios, respectively. These figures show how the shape of the plumes for both species change over time in each spreading scenario. For some, the plumes are stretched in the direction of flow (Figure 4.6) while others are stretched perpendicular to flow (Figures 4.4 and 4.5) and others experience stretching in both directions (Figures 4.7 and 4.8). Note that the times shown vary between scenarios. Since the plumes travel at different rates in different scenarios, it is more informative to compare the scenarios in terms of some characteristic distance, $\rho(t)$ traveled by the plume (shown in Figures 4.3-4.8). Due to the unique behavior in radial flow, we define $\rho(t)$ slightly differently between scenarios. For the radial scenario, $\rho(t)$ is the diameter of a circle whose

Table 4.2: Parameter values used in numerical simulations.

Parameter	Value
Field hydraulic conductivity, K	1 m/d
Aquifer thickness, b	10 m
Porosity, n	0.25
Aquifer left boundary, $-x_b$	-150.125 m
Aquifer right boundary, x_b	150.125 m
Aquifer upper boundary, y_b	150.125 m
Aquifer lower boundary, $-y_b$	-150.125 m
Finite difference grid discretization	0.25 m
Head at $x = -x_b$, h^*	
Active spreading scenarios	0 m
Uniform flow scenario	75.0625 m
Injection rate, Q	500 m^3/d
Uniform velocity, $\mathbf{v}_u$	1 m/d
Coordinates of well 1, $\mathbf{x_1}$	(-25 m,0 m)
Coordinates of well 2, $\mathbf{x_2}$	(0 m,0 m)
Coordinates of well 3, $\mathbf{x_3}$	(25 m,0 m)
Longitudinal dispersivity, α_L	0.1 m
Transverse dispersivity, α_T	0.01 m
Initial concentration of solute plume, C_{A0}	25.6 mg/m^3
Initial Concentration of solute plume, C_{B0}	6.4 mg/m^3
Radius of initial plume of species A, r_A	4.1667m
Diameter of initial plume of species A, d	8.3334 cm
Outer radius of initial plume of species B, r_B	8.3334 cm
Number of particles of species A	1x10^6
Number of particles of species B	3x10^6

circumference is the advective travel distance from the centroid of the initial plume for species A. For uniform flow as well as the remaining active spreading scenarios, $\rho(t)$ represents the distance traveled by the center of mass of the species A. Each scenarios is run until $\rho(T)/d = 2$ (chosen to be low enough that the plume was not yet extracted at Well 3), where T is the time required for the plume centroid to travel said distance. The value of T for each active spreading scenario varies due to the variation in velocities sampled by the plume and is given in Table 4.1. For uniform flow, $T = 17$ days.

4.4   Measures

Similar to Chapter 3, we investigate the effect of active spreading on mixing-controlled reaction both globally and locally. We use the cumulative mass reacted to determine the degree of reaction enhancement of each spreading scenario. We define reaction enhancement as the increase in the cumulative mass reacted relative to its value for uniform flow (no active spreading). If the cumulative mass reacted decreases relative to uniform flow, reaction is negatively enhanced. We use both the derivative of the cumulative mass reacted with time as well as the local measures to identify the spreading mechanisms responsible for said reaction enhancement. As we introduce each measure, we evaluate it for uniform flow in a homogeneous aquifer to understand its behavior without any active spreading.

4.4.1   Global Measures

The amount of reaction in each scenario is presented as cumulative mass reacted of species B, $M_{\mathrm{rxn}}(t)$, given by

$$M_{\mathrm{rxn}}(t) = M_{B0} - M_B(t), \tag{4.10}$$

where $M_B(t)$ is the current mass of species B with time and M_{B0} is the initial mass of species B. Since we are assuming a one to one instantaneous reaction between A and B, the cumulative mass reacted of species B is equal to the cumulative mass reacted of species A.
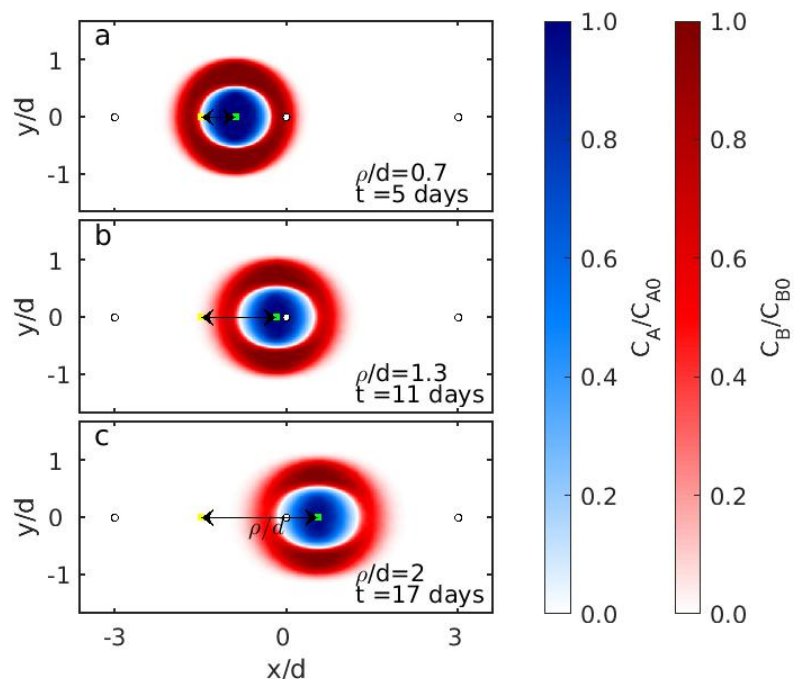
Figure 4.3: Concentration distribution of the species A (blue) and species B (red) for uniform flow at $\rho/d = 0.7, 1.3, 2$. The yellow square represents the center of the initial plume, (x_p, y_p), the green square represents the centroid the plume and the distance between them represents the normalized travel distance of the plume ρ/d. The open circles represent the well locations.
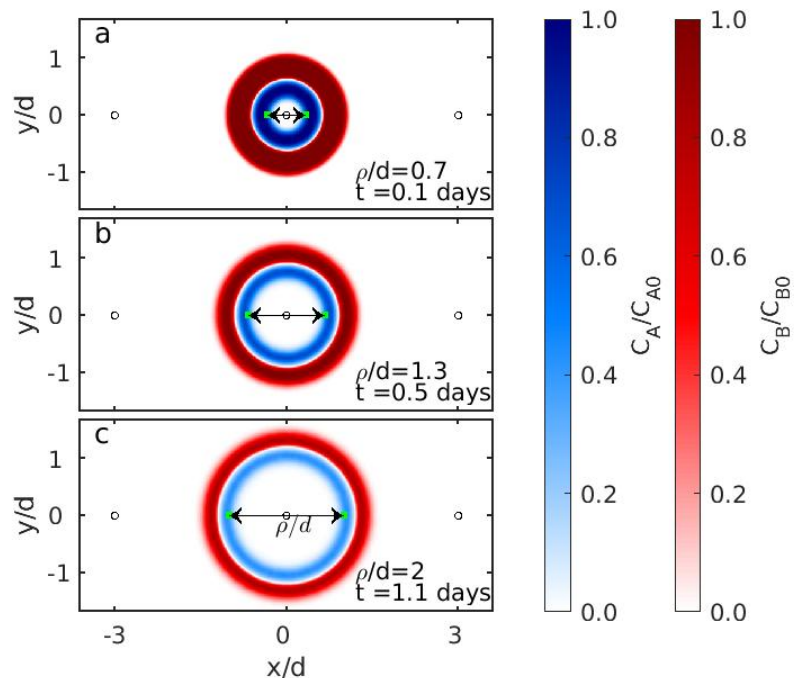
Figure 4.4: Concentration distribution of the solute A (blue) and solute B (red) for the radial scenario at $\rho/d = 0.7, 1.3, 2$. The yellow square represents the center of the initial plume, (x_p, y_p), the green square represents the location of a particle placed at the origin under pure advective travel and the distance between them represents the normalized travel distance of the plume ρ/d. The open circles represent the well locations.
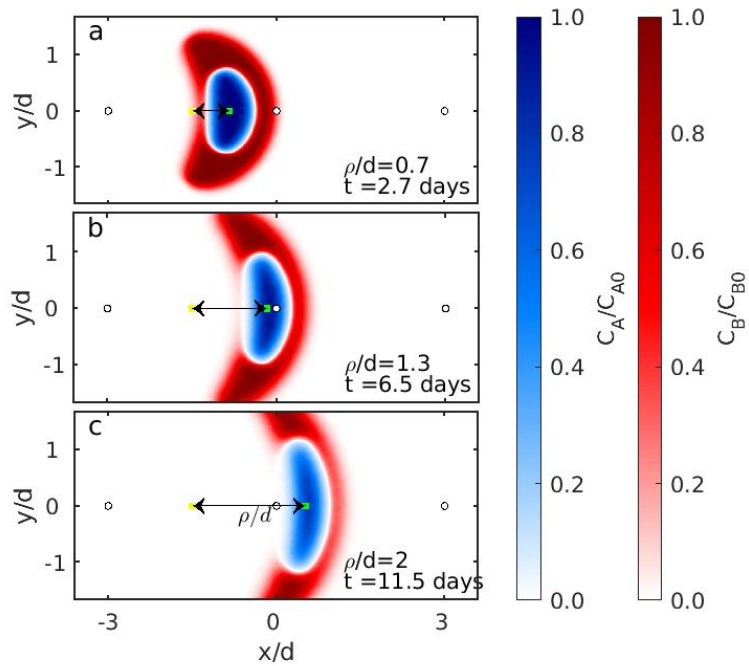
Figure 4.5: Concentration distribution of the solute A (blue) and solute B (red) for the diverging scenario at $\rho/d = 0.7, 1.3, 2$. The yellow square represents the center of the initial plume, (x_p, y_p), the green square represents the centroid the plume and the distance between them represents the normalized travel distance of the plume ρ/d. The open circles represent the well locations.
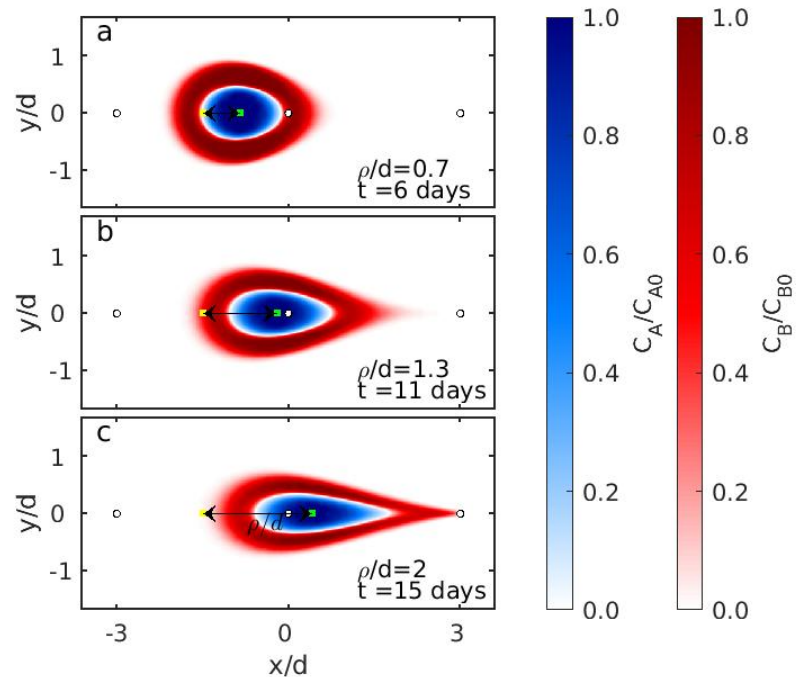
Figure 4.6: Concentration distribution of the solute A (blue) and solute B (red) for the converging scenario at $\rho/d = 0.7, 1.3, 2$. The yellow square represents the center of the initial plume, (x_p, y_p), the green square represents the centroid the plume and the distance between them represents the normalized travel distance of the plume ρ/d. The open circles represent the well locations.
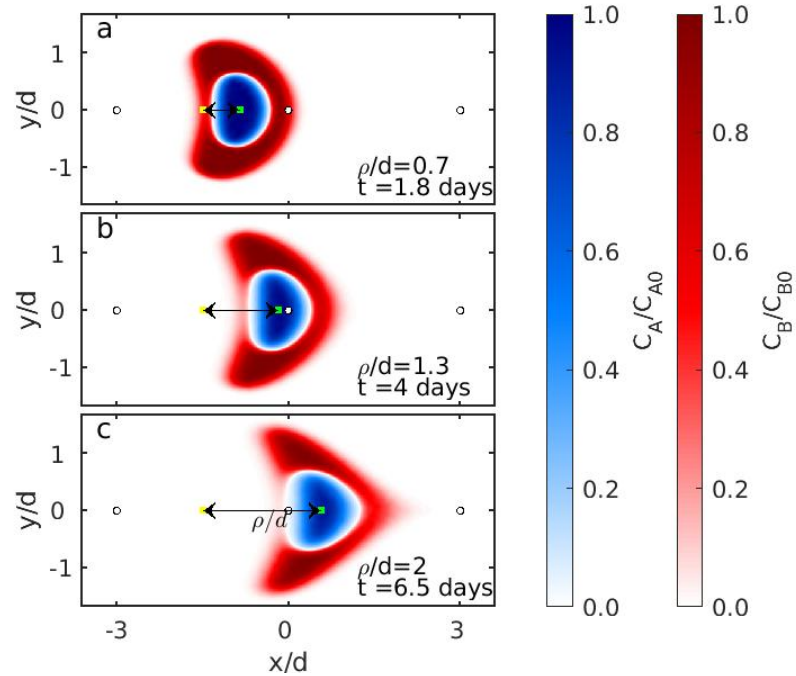
Figure 4.7: Concentration distribution of the solute A (blue) and solute B (red) for the dipole scenario at $\rho/d = 0.7, 1.3, 2$. The yellow square represents the center of the initial plume, (x_p, y_p), the green square represents the centroid the plume and the distance between them represents the normalized travel distance of the plume ρ/d. The open circles represent the well locations.

Figure 4.8: Concentration distribution of the solute A (blue) and solute B (red) for the stagnation scenario at $\rho/d = 0.7, 1.3, 2$. The yellow square represents the center of the initial plume, (x_p, y_p), the green square represents the centroid the plume and the distance between them represents the normalized travel distance of the plume ρ/d. The open circles represent the well locations.
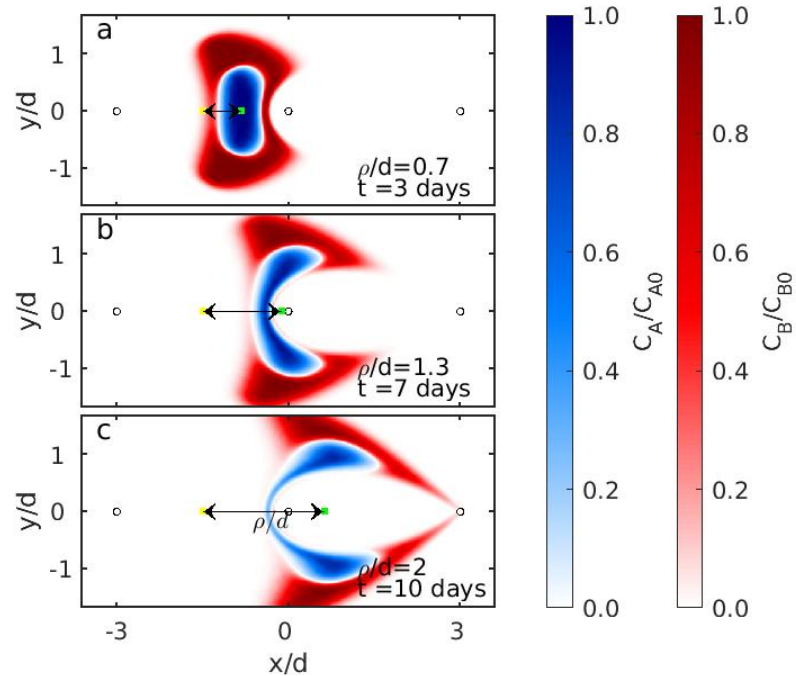
We calculate $M_{\text{rxn}}(t)$ using two different methods. The first method calculates $M_{\text{rxn}}(t)$ directly by summing the mass of all the particles of species B and is given by

$$M_{\text{rxn}}(t) = M_{B0} - \sum_{j=1}^{N} m_{B_j}(t), \tag{4.11}$$

$m_{B_j}(t)$ represents the mass of the *jth* particle for species B and N is total number of species B particles. The second method is described in the next paragraph.

Given our assumption that species A and B react instantaneously and irreversibly, the rate of increase of $M_{\text{rxn}}(t)$, dM_{rxn}/dt, is limited by the flux of species B, or alternatively species A, over the interface between the two species (Ottino, 1989), which is expressed by

$$\frac{dM_{\text{rxn}}}{dt} = nb \int_{\Gamma} \frac{\partial C_B}{\partial \beta} D_{\perp} d\Gamma_{\text{Int}}, \tag{4.12}$$

where Γ_{Int} is the interface between species A and B, $\partial C_B / \partial \beta$ is the concentration gradient of species B in the direction β defined as the local outward direction perpendicular to Γ_{Int}, and $D_{\perp}$, the component of the dispersion tensor perpendicular to Γ_{Int}, has a contribution from longitudinal dispersion that is proportional to the component of velocity perpendicular to Γ_{Int} and a contribution from transverse dispersion that is proportional to the component of velocity parallel to Γ_{Int}, given by

$$D_{\perp} = \alpha_L \left| \sin \theta (\mathbf{v} \cdot \hat{\mathbf{n}}) \right| + \alpha_T \left| \cos \theta (\mathbf{v} \cdot \hat{\mathbf{z}}) \right|, \tag{4.13}$$

where $\hat{\mathbf{n}}$ and $\hat{\mathbf{z}}$ are unit vectors in the directions normal, β, and transverse, ξ, to Γ_{Int}, respectively, and θ is the angle between the local flow direction, s, and the ξ direction as shown in Figure 4.9. It follows directly from (4.12) that $M_{\text{rxn}}(t)$ can also be calculated by

$$M_{\text{rxn}}(t) = \int_{0}^{t} \left[nb \int_{\Gamma} \frac{\partial C_B}{\partial \beta} D_{\perp} d\Gamma_{\text{Int}} \right] dt'. \tag{4.14}$$

Since reaction is instantaneous, the concentrations of both species is zero along Γ_{Int}. However, note that for reaction to occur at a point along Γ_{Int}, and thus for (4.14) to be valid, the concentration of both species must be non-zero in the vicinity around Γ_{Int}. This is different from the conservative mixing in Chapter 3 since, in that case, there was only one species.

The downside to using (4.14), compared to (4.11), is that it requires the calculation of Γ_{Int} and $\partial C_B \partial \beta$ from the concentration distribution of species B, both of which are prone to error since they must be estimated using numerical methods. However, the benefit of calculating $M_{\text{rxn}}(t)$ using (4.14) is that we can break it up into its local components, $\partial C_B/\partial \beta$ and $D_\perp$ and thus investigate how the local behavior along Γ_{Int} affects the global reaction behavior. Given the error associated with estimating both Γ_{Int} and $\partial C_B/\partial \beta$, we compare $M_{\text{rxn}}(t)$ as well as the derivative of $M_{\text{rxn}}(t)$ with time calculated using both methods to show that the general behavior is the same which means that we are capturing the correct behavior of the components of $M_{\text{rxn}}(t)$ at the local level.

Figure 4.10a shows the temporal evolution of $M_{\text{rxn}}(t)$ calculated using both (4.14) and (4.11). Both $M_{\text{rxn}}(t)$, calculated using (4.11), and $M_{\text{rxn}}(t)$, calculated using (4.14), exhibit similar behavior, both increasing at a decreasing rate. However, $M_{\text{rxn}}(t)$, calculated using (4.14) underestimates the amount of reaction measured by (4.11). This is an artifact of how the gradient was estimated. To better evaluate the differences between the two methods, Figure 4.10b shows the temporal evolution of dM_{rxn}/dt with respect to time for $M_{\text{rxn}}(t)$ calculated using (4.14) and $M_{\text{rxn}}(t)$ calculated using (4.11). The value of dM_{rxn}/dt decreases at a decreasing rate regardless of the method used. However, similar to Figure 4.10a, dM_{rxn}/dt calculated using (4.14) is less than when it is calculated using (4.11). Initially, the rate of increase of $M_{\text{rxn}}(t)$ is almost an order of magnitude higher using (4.11) than (4.14). However, the difference between the two methods decreases rapidly. Therefore, we will accept the relative values of $M_{\text{rxn}}(t)$ from (4.14).

4.4.2   Local Measures

To evaluate the local reaction behavior along Γ_{Int}, we use the concentration gradient, $\partial C_B/\partial \beta$, and the component of the dispersion coefficient perpendicular to Γ_{Int}, $D_\perp$. At a point along Γ_{Int}, the product of these two measures is proportional to the dispersive mass flux of species B across Γ_{Int}. Since the dispersive mass flux controls how quickly the two species are brought together to react, $\partial C_B/\partial \beta$ and $D_\perp$ are a direct measures for the reaction rate at a specific point along Γ_{Int}.

Since the goal of this study is to determine how spreading under different active spread-
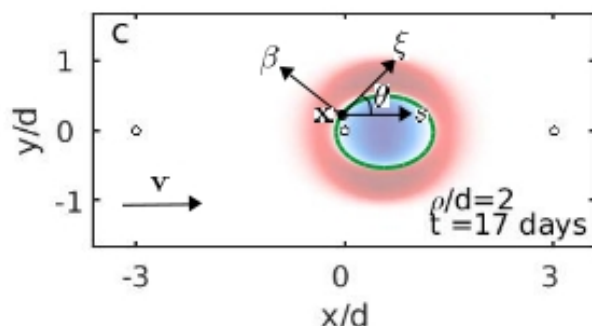
Figure 4.9: Concentration of the plume under uniform flow at $\rho/d = 2$ showing the location of Γ_{Int} (green curve) as well as the directions perpendicular, β, and transverse, ξ, to Γ_{Int} at the point $\mathbf{x}$. Also shown is the angle, θ, between the local flow direction, s, and the ξ direction at $\mathbf{x}$. $\mathbf{v}$ is the local flow velocity vector.
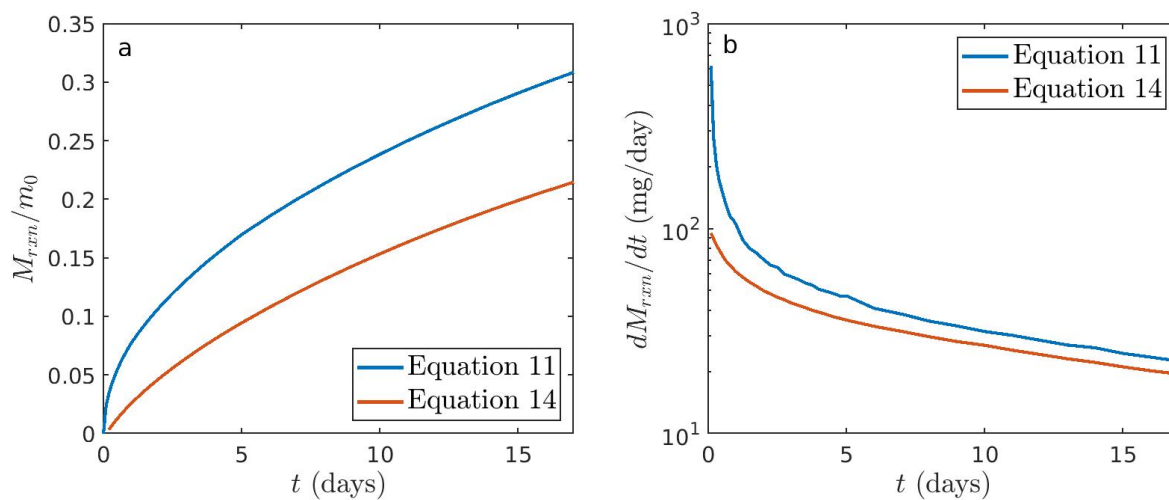
Figure 4.10: Evolution of global measures (calculated using (4.11) and (4.14)) for uniform flow in a homogeneous aquifer. (a) Normalize cumulative mass reacted, $M_{\text{rxn}}(t)/m_{B0}$ and (b) derivative of $M_{\text{rxn}}(t)$ with respect to time, $dM_{\text{rxn}}(t)/dt$

ing scenarios affects reaction enhancement, we evaluate the local spreading along Γ_{Int} using the instantaneous strain, ζ, given by

$$\zeta = \frac{d\ell}{dt}\frac{\triangle t}{\ell}, \tag{4.15}$$

where ℓ is the length of a small arc of Γ_{Int} and $\triangle t$ is the time interval over which the strain is calculated. Since the instantaneous strain depends on advection only and not dispersion, it is a direct measure of spreading (Zhang et al., 2009).

Figure 4.11 shows the local spreading measure, ζ, as well as both the local reaction measures, $\partial C_B/\partial \beta$ and $D_\perp$, along Γ_{Int} for uniform flow at $\rho/d = 0.7, 1.3, 2$. At any given time, the strain is zero along the entire length of Γ_{Int} since uniform flow has no spatial variability of velocity, which is necessary to produce spreading.

At a given point in time, $\partial C/\partial \beta$ is highest for the northern and southern extremes of Γ_{Int} and lowest for the eastern and western extremes. At a given point along Γ_{Int}, $\partial C_B/\partial \beta$ decreases over time. To compare the difference in rate of decrease of $\partial C_B/\partial \beta$ along Γ_{Int}, we plot $\partial C_B/\partial \beta$, with respect to ρ/d for both the western most point and the northern most point of Γ_{Int} (Figure 4.12). The values of $\partial C_B/\partial \beta$ for both locations are approximately equal at $\rho/d = 0$. However, $\partial C_B/\partial \beta$ initially decreases more rapidly for the western most point than the northern most point of Γ_{Int}.

The difference in the rate of decrease in $\partial C_B/\partial \beta$ between the two locations is due to the difference in $D_\perp$ at the two locations. At any given time, $D_\perp$ is highest along the eastern and western extremes of Γ_{Int} and lowest along the northern and souther extremes. Since longitudinal dispersivity is higher than transverse dispersivity, $D_\perp$ is higher where Γ_{Int} is perpendicular to velocity because longitudinal dispersion dominates in those regions and lower where Γ_{Int} is parallel to velocity because transverse dispersion dominates in those regions. Subsequently, in regions where $D_\perp$ is higher, the dispersive mass flux across Γ_{Int} is higher, resulting in more smoothing of the concentration gradient and therefore a faster rate of decrease of $\partial C_B/\partial \beta$. As a result, as seen from Figure 4.11, in regions where $D_\perp$ is highest, $\partial C_B/\partial \beta$ is lowest and vice versa.
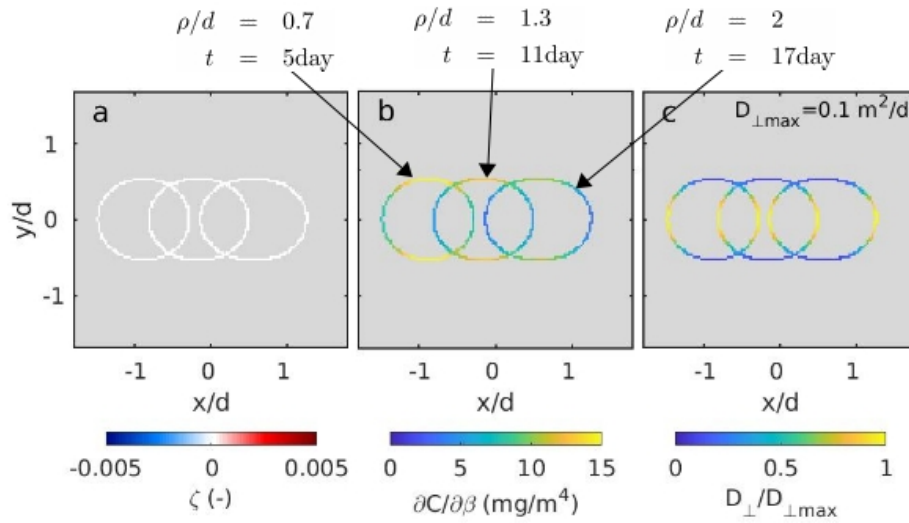
Figure 4.11: Evolution of local measures for uniform flow in a homogeneous aquifer. (a)Instantaneous strain, ζ, (b) $\partial C/\partial \beta$, and (c) The component of the dispersion coefficient perpendicular to Γ_{C^*}, $D_\perp$. Arrow denotes direction of flow and the open circle represents the location of the center well.
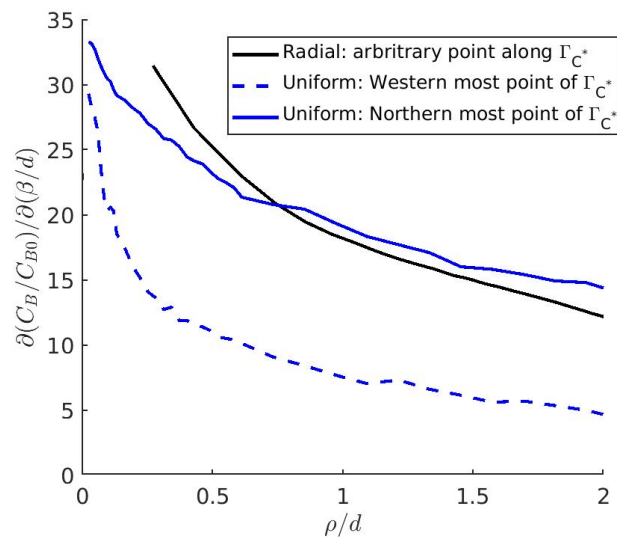
Figure 4.12: $\partial C_B/\partial \beta$ along Γ_{Int} plotted with respect to ρ/d for uniform flow and the radial scenario.

4.5   Results and Discussion: The Effects of Active Spreading on Reaction

In this section, we evaluate the global and local measures for the five active spreading scenarios described in Table 4.1 and Figures 4.2. We compare the evolution of $M_{\mathrm{rxn}}(t)$ to that obtained with uniform flow to evaluate the degree of reaction enhancement obtained by the active spreading scenario. We use dM_{rxn}/dt as well as the local measures, evaluated along Γ_{Int}, to explain the varying degrees of reaction between scenarios.

4.5.1   Global Analysis

The evolution of $M_{\mathrm{rxn}}(t)$ calculated using (4.14) is given with respect to time in Figure 4.13a as well as with normalized travel distance, ρ/d, in Figure 4.13b. In this study, we compare the amount of mixing after the plume has traveled a normalized travel distance of $\rho/d = 2$. Given that the plume samples different velocities magnitudes in different scenarios, the total time to reach $\rho/d = 2$, and therefore the total time available for reaction, varied over a large range between scenarios, as seen in Figure 4.13a. The radial scenario has the least amount of time available for reaction while uniform flow has the greatest. The second smallest is the dipole scenario, followed by the stagnation scenario, diverging scenario and then the converging scenario.

The value of $M_{\mathrm{rxn}}(t)$ grows with time for all active spreading scenarios. For $\rho/d = 2$, the radial and diverging scenario have the most reaction enhancement, followed by the stagnation scenario and then the dipole scenario. The converging scenario has slightly negative reaction enhancement when compared to uniform flow. Also note, when plotted with respect to ρ/d, $M_{\mathrm{rxn}}(t)$ of the radial scenario is less than uniform flow for $\rho/d < 1.7$.

The evolution of the rate of change of $M_{\mathrm{rxn}}(t)$ is given with respect to t in Figure 4.13c as well as with respect to ρ/d in Figure 4.13d. All scenarios decrease at a decreasing rate. However, the initial magnitude of dM_{rxn}/dt varies between scenarios. The radial scenario has the highest initial dM_{rxn}/dt by an order of magnitude over the other scenarios. The dipole, stagnating and diverging scenarios all have similar initial dM_{rxn}/dt values while the initial dM_{rxn}/dt for the converging

scenario is similar to uniform flow.

The differences in the amount of time available for reaction as well as initial values of dM_{rxn}/dt described above help explain the varying degrees of reaction enhancement between scenarios shown in Figures 4.13a and b. While the radial scenario has the least amount of time available for reaction, the initial magnitude of dM_{rxn}/dt is large enough compared to the other scenarios that the radial flow scenario has one of the greatest reaction enhancements. As stated above, the diverging, dipole and stagnation scenarios all have similar initial dM_{rxn}/dt values as well as similar rates of decrease. Thus, for these three scenarios, it is the difference in the amount of time available for reaction that explains the different degrees of reaction enhancement. Out of the three scenarios, the diverging scenario has the greatest amount of time available for reaction and thus has the most reaction enhancement while the dipole scenario has the least amount of time available for reaction thus the least amount of reaction enhancement. Lastly, the converging scenario has less time available for reaction than uniform flow as well as dM_{rxn}/dt decreases more rapidly initially than uniform flow. This explains why the converging scenario has negative reaction enhancement compared to uniform flow.

4.5.2   Local Analysis

In the previous section, the behavior of dM_{rxn}/dt was analyzed to explain the different degrees of reaction enhancement between the active spreading scenarios. This section attempts to further that understanding by analyzing locally the effect of active spreading on the behavior of the local reaction measures, $\partial C_B/\partial \beta$ and $D_\perp$ along Γ_{Int}. Specifically, we identify the effects of active spreading on $\partial C_B/\partial \beta$ and $D_\perp$ that lead to positive reaction enhancement as well as those that lead to negative reaction enhancement.

The mass of B reacted at a point along Γ_{Int} is related the dispersive mass flux of B (or, since we are assuming one to one and instantaneous reaction, alternatively, A) across Γ_{Int} at that point. This, in turn, depends on the product of $D_\perp$ and $\partial C_B/\partial \beta$. Therefore, in regions where both $D_\perp$ and $\partial C_B/\partial \beta$ are high, the amount of reaction will also be high. Alternatively, where both $D_\perp$ and
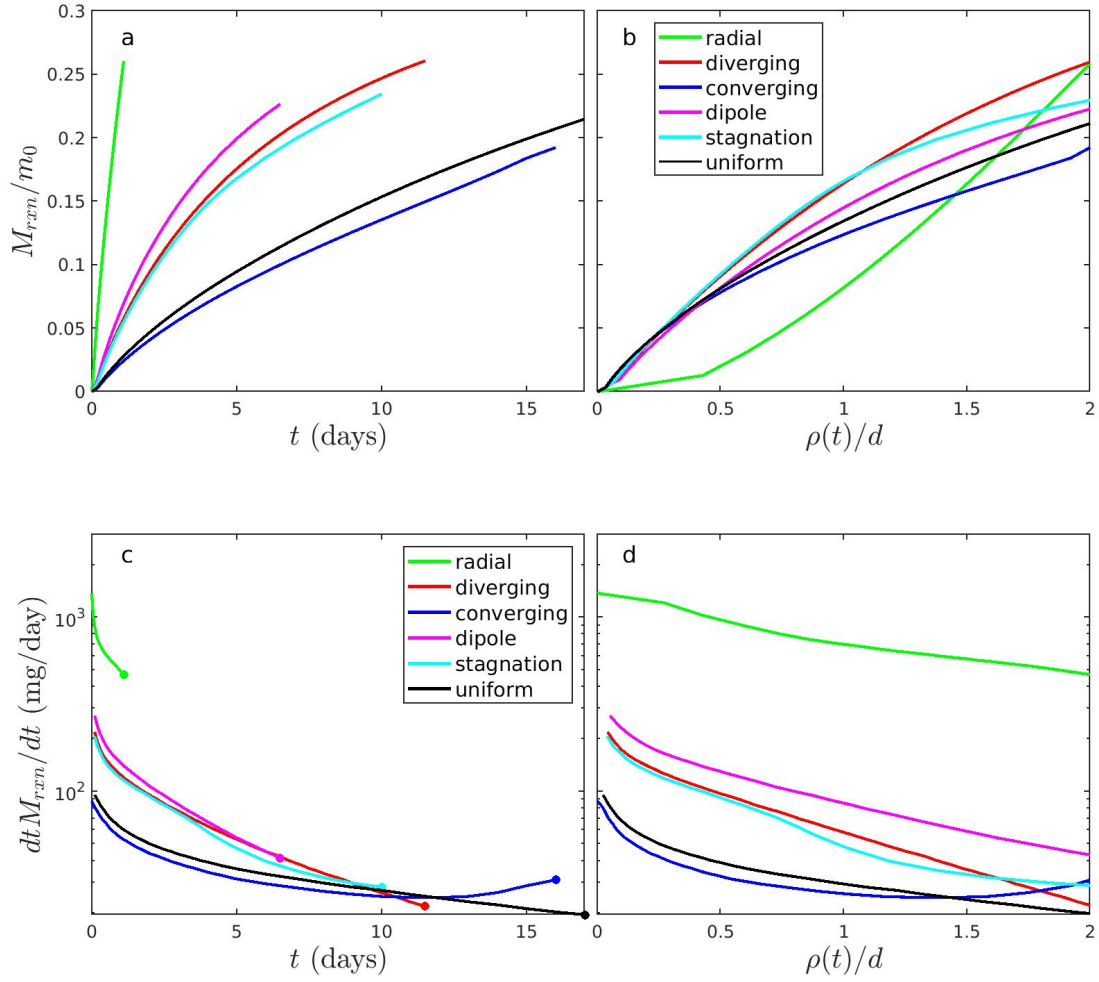
Figure 4.13: Evolution of global measures (calculated using (4.14)) for the active spreading scenarios. (a) Normalized cumulative mass reacted, $M_{\mathrm{rxn}}(t)/m_{B0}$, vs t, (b) Normalized cumulative mass reacted, $M_{\mathrm{rxn}}(t)/m_{B0}$, vs ρ/d, (c) derivative of $M_{\mathrm{rxn}}(t)$, $dM_{\mathrm{rxn}}(t)/dt$, vs t, and (d) derivative of $M_{\mathrm{rxn}}(t)$, $dM_{\mathrm{rxn}}(t)/dt$, vs ρ/d. The filled in circles are included to help distinguish where each scenario ends.

$\partial C_B/\partial \beta$ are low, the amount of reaction will also be low. Consequently, to understand how active spreading enhances reaction, we need to understand first how $D_\perp$ and $\partial C_B/\partial \beta$ affect reaction and second how active spreading can affect the behavior of $D_\perp$ and $\partial C_B/\partial \beta$ in such a way that leads to enhanced reaction. Since for reaction two occur, the two species must first mix, the same concepts for conservative mixing described in Chapter 3 also apply to mixing-controlled reaction.

The value of $D_\perp$ is based on the orientation of Γ_{Int} with the local velocity vector (4.13). Since longitudinal dispersivity is usually an order of magnitude more that transverse dispersivity (Sahimi et al., 1986), where Γ_{Int} is oriented perpendicular to flow, $D_\perp$ is maximized for a given velocity. Alternatively where Γ_{Int} is oriented parallel to flow, $D_\perp$ is minimized for a given velocity. Thus, active spreading that reconfigures the plume in such a way that orients Γ_{Int} perpendicular to the local flow direction will enhance reaction.

For flow with no spreading (i.e., uniform flow) the rate of decrease of $\partial C_B/\partial \beta$ at a given point along Γ_{Int} depends on the value of $D_\perp$. Figure 4.11 shows that for uniform flow $\partial C_B/\partial \beta$ decreases faster in regions of high $D_\perp$ and slower in regions of low $D_\perp$. However, spreading, or specifically stretching, can also affect the rate of decrease of $\partial C_B/\partial \beta$. As a plume is stretched in one direction, it is compressed in the perpendicular direction due to mass conservation, leading to an increase in the concentration gradient in the direction perpendicular to stretching that slows the decrease in the concentration gradient caused by dispersion. Thus, $\partial C_B/\partial \beta$ will remain elevated for longer time, which will enhance reaction. Lastly, since reaction occurs along Γ_{Int}, a longer Γ_{Int} leads to a larger area available for reaction. Since stretching along Γ_{Int} increases the length of Γ_{Int}, stretching can enhance reaction in this way as well.

For mixing-controlled reaction, the total mass of both reactant species decreases with time. Thus, for mixing-controlled reaction, it is possible for the concentration of either species to reduce to zero along Γ_{Int}. In this case, no reaction would occur in that region even it the behaviors of $\partial C_B/\partial \beta$, $D_\perp$ and stretching would promote mixing.

Figures 4.14a,b and c show the local measures for radial flow at ρ/d=0.7,1.3 and 2. All three measures are uniform along Γ_{Int} and decrease with time (and with ρ). The instantaneous strain

rate, ζ, is positive which signifies that Γ_{Int} is stretching and therefore increasing in length. To see the effect of stretching on the rate of decrease of $\partial C_B/\partial \beta$, Figure 4.12 plots $\partial C_B/\partial \beta$, with respect to ρ/d. The value of $\partial C_B/\partial \beta$ decreases at a decreasing rate. However, $\partial C_B/\partial \beta$ is higher for radial flow than both locations for uniform flow for $\rho/d < 0.75$ and higher than the western most point for uniform flow for all ρ/d. Although the maximum $D_\perp$ is larger in the radial scenario than uniform flow (from Figure 4.14c), the decrease in $\partial C_B/\partial \beta$ due to dispersion is slowed by the increase in $\partial C_B/\partial \beta$ caused by stretching.

The high values of $D_\perp$ are partly due to the fact that the velocity experienced by the plume is higher than in the other active spreading scenarios. However, it is also because Γ_{Int} is always perpendicular to the local velocity, so it is the maximum possible for a given velocity. To summarize, the uniform stretching along Γ_{Int} slows the decrease in $\partial C_B/\partial \beta$ while the orientation of Γ_{Int} with the local flow direction ensures the maximum $D_\perp$ for a given velocity all along Γ_{Int}. The overall effect is around 10% more reaction enhancement in the radial scenario over uniform flow.

In contrast to the radial scenario, the remaining active spreading scenarios have regions of stretching ($\zeta > 0$) and contraction ($\zeta < 0$) along Γ_{Int} as well as regions of high and low $D_\perp$ along Γ_{Int}. Thus, the reaction enhancement will depend on how these regions correspond to each other. Specifically, scenarios where regions of stretching ($\zeta > 0$) correspond to regions of high $D_\perp$ will have higher dispersive mass flux and therefor more reaction enhancement as long as both species are present along Γ_{Int}.

A good example of this behavior is found in the diverging scenario (Figures 4.14d,e and f), which has one of the largest reaction enhancements of all the scenarios. In the diverging scenario, Γ_{Int} is stretched north to south while the mean flow direction is west to east. Along the eastern and western regions, $\zeta > 0$ (stretching) and $D_\perp$ is high, resulting in reaction enhancement until $rho/d = 1.3$, when reactant concentrations approach zero along the western regions of Γ_{Int}. Both the dipole (Figure 4.14j,k and l) and the stagnation (Figure 4.14m,n and o) scenarios also have this behavior, although only for $\rho/d = 0.7$, thus, they both have less reaction enhancement than the diverging scenario.
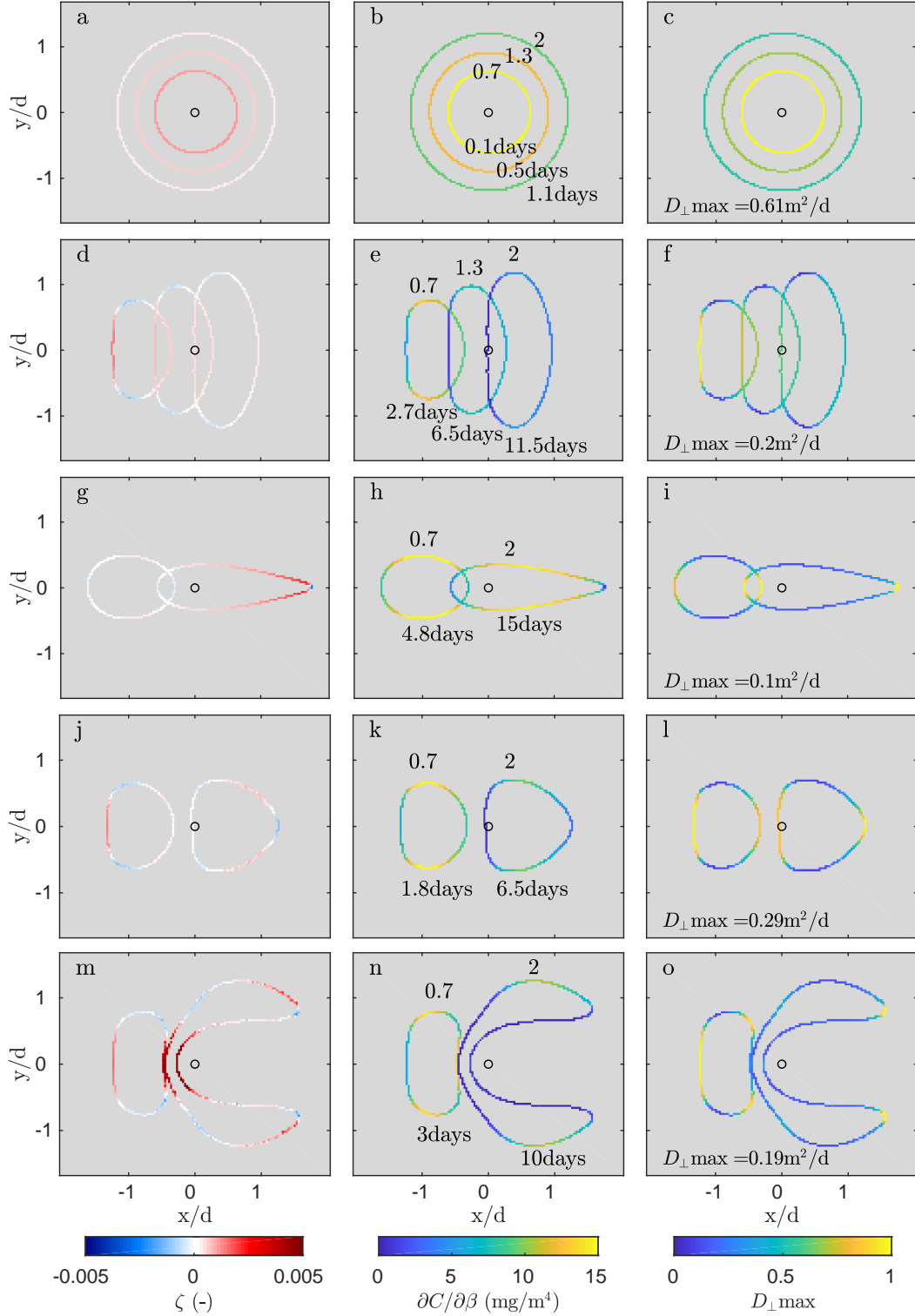
Figure 4.14: Evolution of local measures (Instantaneous strain, ζ $\partial C_B/\partial\beta$, and the component of the dispersion coefficient perpendicular to Γ_{Int}, $D_\perp$) for the active spreading scenarios for $\rho/d = 0.7, 1.3, 2$. The radial scenario is presented in (a),(b) and (c). The diverging scenario in (d),(e) and (f). The converging scenario in (g),(h) and (i). The dipole scenario in (j),(k) and (l), The stagnation scenario in (m),(n) and (o). The open circle represents the location of the Well 2. On the middle figure, the value of ρ/d is listed above each curve while the time is listed below.

Where, instead, regions of low $D_\perp$ correspond to regions of stretching ($\zeta > 0$), the enhancement to reaction caused by the stretching is lower because of the low $D_\perp$. Additionally, where regions of high $D_\perp$ correspond to regions of contraction ($\zeta < 0$), the enhancement to reaction caused by high $D_\perp$ is lower because the high $D_\perp$ values cause $\partial C_B/\partial \beta$ to decrease rapidly. This latter effect was seen in uniform flow (Figures 4.11 and 4.12).

A good example of this behavior is found in the converging scenario (Figures 4.14g,h and i), which has slightly negative reaction enhancement when compared to uniform flow. For the converging scenario, both the direction of plume stretch and the direction of mean flow are in the west to east direction. In consequence, the regions of $\zeta < 0$ (Figure 4.14g) correspond to the regions of high $D_\perp$ (Figure 4.14i) and the regions of $\zeta > 0$ correspond to the regions of low $D_\perp$, for all ρ/d. Notice that the rate of decrease of $\partial C_B/\partial \beta$ for regions of $\zeta > 0$ is slowed as a result of the stretching but the overall reaction enhancement is limited due to the low $D_\perp$ values. Also, notice from figure 4.5 that the concentration of species B adjacent to Γ_{Int} is above zero for all times. Thus, the behavior described above for converging flow with reaction is the same as we saw for converging flow with no reaction in Chapter 3. This behavior is also observed, for $\rho/d = 2$, in both the dipole (Figure 4.14j,k,l) and the stagnation (Figure 4.14m,n,o) scenarios. Thus, while the dipole and stagnation scenarios have more reaction enhancement than the converging flow scenario, they have less than the radial and diverging scenarios.

4.6   Conclusion

In this study, we investigated the relationship between spreading and mixing-controlled reaction under the same active spreading scenarios used in Chapter 3. We identified the following behaviors that affect the degree of reaction enhancement:

(1) Scenarios in which regions along Γ_{Int} where stretching is high correspond to regions where $D_\perp$ is high have a higher dispersive mass flow rate across Γ_{Int} and therefor a higher rate of reaction. Scenarios in which the opposite occurs experienced a lower rate of reaction.

(2) For scenarios with similar dispersive mass flow rates, the global reaction behavior over a given travel distance is greater for scenarios in which the total time available for reaction is greater.

In both the radial scenario and the diverging scenario, regions of stretching corresponded to regions of high $D_\perp$, resulting in more reaction enhancement in these scenarios compared to the other scenarios. In converging flow, regions of stretching corresponded to regions of low $D_\perp$ and vice versa, resulting in less reaction than uniform flow. The remaining scenarios showed both behaviors at different times, resulting in some reaction enhancement but not as much as the radial and diverging scenarios. Note, for the diverging scenario as well as to a lesser extent the dipole and stagnation scenarios, there were times where the concentration of species B reduced to zero along Γ_{Int}. In those regions, no reaction occurred even if the reaction enhancing behaviors described above were present.

Chapter 5

Conclusions and Future Work

5.1 Conclusions

During in-situ groundwater remediation, a chemical or biological amendment is introduced into the aquifer to degrade the groundwater contaminant. A remaining challenge of in-situ remediation is achieving high levels of mixing between the amendment and the contaminant. Spreading, defined as the reconfiguration of the plume shape due to spatially-varying velocity fields, has been shown to enhanced mixing and reaction. Spreading can occur passively by heterogeneity of hydraulic conductivity or actively by engineered injection and extraction (EIE), in which clean water is injected or extracted at an array of wells surrounding the contaminant plume. Many studies have shown that both passive and active spreading enhance mixing and reaction in porous media. However, studies investigating the local flow mechanisms of active and passive spreading that lead to increased mixing and reaction are limited. Therefore, this research investigated the local flow mechanisms of active and passive spreading that lead to increased mixing and reaction. In this dissertation, I identified local behaviors present in a variety of active spreading, passive spreading and combined active and passive spreading flows that enhance mixing and reaction in porous media.

In Chapter 2, I analyzed the mixing and reaction enhancement of the three active spreading scenarios used in a combined experimental and numerical project. The analysis showed that while the amount of mixing and reaction was similar between scenarios, the rates of increase of the individual steps were distinct. By analyzing the different flow fields in each step, I was able to determine certain features of the active spreading flow fields that corresponded to increased rates

of mixing and reaction. Specifically, when the plume boundary was oriented perpendicular to the direction of flow as well as stretched perpendicular to the direction of flow, the rate of increase of mixing and reaction was high. Additionally, stretching parallel to the direction of flow led to high mixing and reaction rates when it was followed in a subsequent step by a flow field oriented perpendicular to the plume boundary. Given these observations, I concluded that the effect of active spreading on mixing and reaction is not only due to the increase in surface area available for mixing and reaction via stretching. The orientation of the plume as well as the direction of spreading with respect to the flow direction is also important.

In Chapter 3, I investigated the relationship between spreading and mixing under non-uniform flow fields typical of EIE remediation systems (active spreading) in aquifers with simple heterogeneity patterns (passive spreading). To investigate active spreading alone, I evaluated five different active spreading scenarios: Radial, Divering, Converging, Dipole and Stagnation. To investigate passive spreading alone, I evaluated uniform flow through a homogeneous aquifer of hydraulic conductivity K with a rectangular inclusion of hydraulic conductivity K_{inc}. I identified the behaviors in active spreading alone, passive spreading alone, and in the combination of active and passive spreading that lead to enhanced mixing and those that lead to negatively enhanced mixing when compared to uniform flow through homogeneous porous media. Independent of the type of spreading, I identified the following behaviors that affect the degree of mixing enhancement:

(1) Let Γ_{C^*} represent the curve along which the concentration is equal to C^*, where $C^*(t) = 0.5C_{\mathrm{max}}(t)$ and $C_{\mathrm{max}}(t)$ is the maximum concentration of the plume at time t. Scenarios in which regions along Γ_{C^*} where stretching is high correspond to regions where the component of the dispersion tensor perpendicular to Γ_{C^*}, $D_{\perp}$, is high have a higher dispersive mass flow rate across Γ_{C^*} and therefore a higher rate of mixing. Scenarios in which the opposite occurs experienced a lower rate of mixing.

(2) For scenarios with similar dispersive mass flow rates, the global mixing behavior over a given travel distance is greater for scenarios in which the total time available for mixing is

greater.

For active spreading, in both the radial scenario and the diverging scenario, regions of stretching corresponded to regions of high $D_\perp$, resulting in more mixing enhancement in these scenarios compared to the other scenarios. In converging flow, regions of stretching corresponded to regions of low $D_\perp$ and vice versa, resulting in less mixing than uniform flow. The remaining scenarios showed both behaviors at different times, resulting in some mixing enhancement but not as much as the radial and diverging scenarios.

For the passive spreading scenarios where $K/K_{inc} > 1$, the regions of Γ_{C^*} in the inclusion experienced stretching and high $D_\perp$. Thus, the mixing rate of the plume increased compared to uniform flow while the plume interacted with the inclusion. However, the decreased travel time, due to higher velocities in the inclusion, reduced the time available for mixing compared to uniform flow. Therefore, for a given scenario, mixing was enhanced over a given travel distance when the first effect was stronger than the second.

For the passive spreading scenarios where $K/K_{inc} < 1$, the degree of mixing enhancement was partly a result of regions of stretching corresponding to regions of high $D_\perp$, however, it was also due to the relatively large increase in the length of Γ_{C^*}, independent of the value of $D_\perp$. Additionally, the amount of convergence of the plume after the inclusion also affected the degree of mixing enhancement.

For combined active and passive spreading, I showed that when the converging active spreading scenario is combined with passive spreading for $K/K_{inc} > 1$, the behaviors of the converging scenario that negatively enhanced mixing are changed to behaviors that enhanced mixing, resulting in more mixing than in the converging scenario alone. I also showed that when the diverging active spreading scenario is combined with passive spreading $K/K_{inc} > 1$, the behaviors that enhanced mixing for each scenario alone compete against each other, resulting in a decrease in mixing enhancement compared to the diverging scenario alone.

In Chapter 4, I investigated the relationship between spreading and mixing-controlled reaction

(one to one, instantaneous and irreversible) under the same active spreading scenarios used in Chapter 3. I identified the following behaviors that affect the degree of reaction enhancement:

(1) Let Γ_{Int} represent the interface between species A and B. Scenarios in which regions along Γ_{Int} where stretching is high correspond to regions where the component of the dispersion tensor perpendicular to Γ_{Int}, $D_\perp$, is high have a higher dispersive mass flow rate across Γ_{Int} and therefor a higher rate of reaction. Scenarios in which the opposite occurs experienced a lower rate of reaction.

(2) For scenarios with similar dispersive mass flow rates, the global reaction behavior over a given travel distance is greater for scenarios in which the total time available for reaction is greater.

In both the radial scenario and the diverging scenario, regions of stretching corresponded to regions of high $D_\perp$, resulting in more reaction enhancement in these scenarios compared to the other scenarios. In converging flow, regions of stretching corresponded to regions of low $D_\perp$ and vice versa, resulting in less reaction than uniform flow. The remaining scenarios showed both behaviors at different times, resulting in some reaction enhancement but not as much as the radial and diverging scenarios. Note that for the diverging scenario as well as to a lesser extent the dipole and stagnation scenarios, there were times where the concentration of species B reduced to zero along Γ_{Int}. In those regions, no reaction occurred even if the reaction enhancing behaviors described above were present.

5.2   Future Work

This work links the global mixing/reaction enhancement to the local transport behavior to identify the local behavior during active spreading alone, passive spreading alone and combined active and passive spreading that enhance mixing and reaction. I focused our analysis on simple active spreading flow fields as well as simple heterogeneity patterns. However, while the results of this work in their current form can be used to assist the design of EIE sequences in the field, their

usefulness can be increased by increasing the complexity of both the active spreading scenarios as well as the heterogeneity patterns analyzed.

In Chapters 3 and 4, the active spreading scenarios analyzed were representative of the individual steps typical to an active spreading sequence used in EIE. For each active spreading flow field investigated, I evaluated one initial plume position/active well combination. The next step is to vary the location and size of the plume with respect to the active wells to see how the spreading and mixing behavior changes. Additionally, I evaluated each active spreading scenario separately. Since EIE uses time-varying flows that string together a sequence of different active spreading flow fields, it is also necessary to look at different combinations in time of active spreading flow fields to understand how each step builds off each other to increase or decrease mixing and reaction enhancement. I saw evidence of this in Chapter 2 where stretching parallel to the direction of flow led to high mixing and reaction rates when it was followed in a subsequent step by a flow field oriented perpendicular to the plume boundary.

In Chapters 3 and 4, I analyzed passive spreading caused by high and low hydraulic conductivity inclusions where the hydraulic conductivity as well as the width of the inclusion were varied. As a next step, one could study how the inclusion length as well as the location and number of inclusions affects mixing and reaction enhancement. Also, for all the passive spreading scenarios in which the inclusion had a higher hydraulic conductivity than the aquifer, the whole plume was focused through the inclusion. Thus, decreasing the inclusion width further so that only a portion of the plume is focused through the inclusion would also be beneficial.

Additionally, the heterogeneity models used in this study are simple representations of heterogeneity. Since natural systems have more complex heterogeneity patterns, the next step is to analyze the combined effect of active and passive spreading using more complicated heterogeneity models, e.g., superpositions of inclusions, facies models, smoothly-varying random fields, high connectivity of high K, etc. Of particular interest to groundwater remediation are facies models because they can generate random fields with interconnected fast paths to flow that may pose a challenge to standard in-situ remediation methods if the contaminant or amendment travels rapidly

through these paths. The redirection of flow caused by active spreading may better control the movement of the reactant in aquifers with these fast paths.

Bibliography

Bagtzoglou, A. C. and Oates, P. M. (2007). Chaotic advection and enhanced groundwater remediation. Journal of Materials in Civil Engineering, 19(1):75–83.

Bauer, R. D., Rolle, M., Bauer, S., Eberhardt, C., Grathwohl, P., Kolditz, O., Meckenstock, R. U., and Griebler, C. (2009). Enhanced biodegradation by hydraulic heterogeneities in petroleum hydrocarbon plumes. Journal of Contaminant Hydrology, 105(1-2):56–68.

Bellin, A., Severino, G., and Fiori, A. (2011). On the local concentration probability density function of solutes reacting upon mixing. Water Resources Research, 47(1):doi:10.1029/2010wr009696.

Berkowitz, B., Cortis, A., Dentz, M., and Scher, H. (2006). Modeling non-fickian transport in geological formations as a continuous time random walk. Reviews of Geophysics, 44(2):doi:10.1029/2005rg000178.

Bolster, D., Dentz, M., and Le Borgne, T. (2011). Hypermixing in linear shear flow. Water Resources Research, 47(9):doi:10.1029/2011wr010737.

Chiogna, G., Cirpka, O. A., Grathwohl, P., and Rolle, M. (2011). Transverse mixing of conservative and reactive tracers in porous media: Quantification through the concepts of flux-related and critical dilution indices. Water Resources Research, 47(2):doi:10.1029/2010wr009608.

Cirpka, O. A. (2002). Choice of dispersion coefficients in reactive transport calculations on smoothed fields. Journal of Contaminant Hydrology, 58(3-4):261–282.

Cirpka, O. A. (2005). Effects of sorption on transverse mixing in transient flows. Journal of Contaminant Hydrology, 78(3):207–229.

Cirpka, O. A. (2015). Transverse mixing in heterogeneous aquifers. Procedia Environmental Sciences, 25:66–73.

Cirpka, O. A., de Barros, F. P. J., Chiogna, G., Rolle, M., and Nowak, W. (2011). Stochastic flux-related analysis of transverse mixing in two-dimensional heterogeneous porous media. Water Resources Research, 47(6):doi:10.1029/2010wr010279.

Clifford, M. J. (1999). A gaussian model for reaction and diffusion in a lamellar structure. Chemical Engineering Science, 54(3):303–310.

Clifford, M. J., Cox, S. M., and Roberts, E. (1998). Lamellar modelling of reaction, diffusion and mixing in a two-dimensional flow. Chemical Engineering Journal, 71(1):49–56.

de Anna, P., Dentz, M., Tartakovsky, A., and Le Borgne, T. (2014). The filamentary structure of mixing fronts and its control on reaction kinetics in porous media flows. Geophysical Research Letters, 41(13):4586–4593.

de Barros, F., Fiori, A., Boso, F., and Bellin, A. (2015). A theoretical framework for modeling dilution enhancement of non-reactive solutes in heterogeneous porous media. Journal of Contaminant Hydrology, 175:72–83.

de Barros, F. P., Dentz, M., Koch, J., and Nowak, W. (2012). Flow topology and scalar mixing in spatially heterogeneous flow fields. Geophysical Research Letters, 39(8):doi:10.1029/2012gl051302.

Dentz, M. and Carrera, J. (2007). Mixing and spreading in stratified flow. Physics of Fluids, 19(1):doi:10.1063/1.2427089.

Dentz, M. and de Barros, F. (2015). Mixing-scale dependent dispersion for transport in heterogeneous flows. Journal of Fluid Mechanics, 777:178–195.

Dentz, M., Le Borgne, T., Englert, A., and Bijeljic, B. (2011). Mixing, spreading and reaction in heterogeneous media: A brief review. Journal of Contaminant Hydrology, 120:1–17.

Finn, M. D. and Thiffeault, J.-L. (2011). Topological optimization of rod-stirring devices. SIAM Review, 53(4):723–743.

Fiori, A. (2001). The lagrangian concentration approach for determining dilution in aquifer transport: Theoretical analysis and comparison with field experiments. Water Resources Research, 37(12):3105–3114.

Fu, X., Cueto-Felgueroso, L., Bolster, D., and Juanes, R. (2015). Rock dissolution patterns and geochemical shutdown of co2-brine-carbonate reactions during convective mixing in porous media. Journal of Fluid Mechanics, 764:296–315.

Harbaugh, A. W., Banta, E. R., Hill, M. C., and McDonald, M. G. (2000). MODFLOW-2000, The U.S. Geological Survey modular ground-water model - User guide to modularization concepts and the ground-water flow process. U. S. Geological Survey.

Hidalgo, J. J., Dentz, M., Cabeza, Y., and Carrera, J. (2015). Dissolution patterns and mixing dynamics in unstable reactive flow. Geophysical Research Letters, 42(15):6357–6364.

Kapoor, V. and Kitanidis, P. K. (1996). Concentration fluctuations and dilution in two-dimensionally periodic heterogeneous porous media. Transport in Porous Media, 22(1):91–119.

Kapoor, V. and Kitanidis, P. K. (1998). Concentration fluctuations and dilution in aquifers. Water Resources Research, 34(5):1181–1193.

Kitanidis, P. K. (1994). The concept of the dilution index. Water Resources Research, 30(7):2011–2026.

Le Borgne, T., Dentz, M., Bolster, D., Carrera, J., de Dreuzy, J.-R., and Davy, P. (2010). Non-fickian mixing: Temporal evolution of the scalar dissipation rate in heterogeneous porous media. Advances in Water Resources, 33(12):1468–1475.

Le Borgne, T., Dentz, M., and Carrera, J. (2008a). Lagrangian statistical model for transport in highly heterogeneous velocity fields. Physical Review Letters, 101(9):doi:10.1103/physrevlett.101.090601.

Le Borgne, T., Dentz, M., and Carrera, J. (2008b). Spatial Markov processes for modeling Lagrangian particle dynamics in heterogeneous porous media. Physical Review E, 78(2):doi:10.1103/physreve.78.026308.

Le Borgne, T., Dentz, M., and Villermaux, E. (2013). Stretching, coalescence, and mixing in porous media. Physical Review Letters, 110(20):doi:10.1103/PhysRevLett.110.204501.

Le Borgne, T., Dentz, M., and Villermaux, E. (2015). The lamellar description of mixing in porous media. Journal of Fluid Mechanics, 770:458–498.

Le Borgne, T., Ginn, T. R., and Dentz, M. (2014). Impact of fluid deformation on mixing-induced chemical reactions in heterogeneous flows. Geophysical Research Letters, 41(22):7898–7906.

Lester, D. R., Rudman, M., Metcalfe, G., Trefry, M. G., Ord, A., and Hobbs, B. (2010). Scalar dispersion in a periodically reoriented potential flow: Acceleration via lagrangian chaos. Physical Review E, 81(4):doi:10.1103/physreve.81.046319.

Loader, C. (2013). locfit: Local Regression, Likelihood and Density Estimation. R package version 1.5-9.1.

Mays, D. C. and Neupauer, R. M. (2012). Plume spreading in groundwater by stretching and folding. Water Resour. Res., 48:doi:10.1029/2011wr011567.

Meunier, P. and Villermaux, E. (2010). The diffusive strip method for scalar mixing in two dimensions. Journal of Fluid Mechanics, 662:134–172.

Moroni, M., Kleinfelter, N., and Cushman, J. H. (2007). Analysis of dispersion in porous media via matched-index particle tracking velocimetry experiments. Advances in Water Resources, 30(1):1–15.

National Research Council (2013). Alternatives for Managing the Nation's Complex Contaminated Groundwater Sites. National Academies Press, Washington, DC.

Ottino, J. (1989). The Kinematics of Mixing: Stretching, Chaos, and Transport, volume 4 of 10. Cambridge Univ. Press, Cambridge, U. K.

Ottino, J., Ranz, W. E., and Macosko, C. W. (1979). A lamellar model for analysis of liquid-liquid mixing. Chemical Engineering Science, 34(6):877–890.

Ou, J.-J. and Ranz, W. (1983a). Mixing and chemical reactions a contrast between fast and slow reactions. Chemical Engineering Science, 38(7):1005–1013.

Ou, J.-J. and Ranz, W. (1983b). Mixing and chemical reactions chemical selectivities. Chemical Engineering Science, 38(7):1015–1019.

Paster, A., Aquino, T., and Bolster, D. (2015). Incomplete mixing and reactions in laminar shear flow. Physical Review E, 92(1):doi:10.1103/physreve.92.012922.

Piscopo, A. N., Neupauer, R. M., and Mays, D. C. (2013). Engineered injection and extraction to enhance reaction for improved in situ remediation. Water Resour. Res., 49:3618–3625.

Rajaram, H. and Gelhar, L. W. (1993). Plume scale-dependent dispersion in heterogeneous aquifers: 1. lagrangian analysis in a stratified aquifer. Water Resources Research, 29(9):3249–3260.

Ranz, W. E. (1979). Applications of a stretch model to mixing, diffusion, and reaction in laminar and turbulent flows. AIChE Journal, 25(1):41–47.

Rodríguez-Escales, P., Fernàndez-Garcia, D., Drechsel, J., Folch, A., and Sanchez-Vila, X. (2017). Improving degradation of emerging organic compounds by applying chaotic advection in managed aquifer recharge in randomly heterogeneous porous media. Water Resources Research, 53(5):4376–4392.

Rolle, M., Eberhardt, C., Chiogna, G., Cirpka, O. A., and Grathwohl, P. (2009). Enhancement of dilution and transverse reactive mixing in porous media: Experiments and model-based interpretation. Journal of Contaminant Hydrology, 110(3-4):130–142.

Sahimi, M., Hughes, B. D., Scriven, L., and Davis, H. T. (1986). Dispersion in flow through porous media—i. one-phase flow. Chemical Engineering Science, 41(8):2103–2122.

Salamon, P., Fernàndez-Garcia, D., and Gómez-Hernández, J. J. (2006). Modeling mass transfer processes using random walk particle tracking. Water Resources Research, 42(11):doi:10.1029/2006wr004927.

Siegrist, R., Crimi, M., Broholm, M., McCray, J., Illangasekare, T., and Bjerg, P. (2012). Clean soil and safe water, NATO Science for Peace and Security Series C: Environmental Security. Springer.

Sposito, G. (2006). Chaotic solute advection by unsteady groundwater flow. Water Resources Research, 42(6):doi:10.1029/2005wr004518.

Stremler, M. A., Haselton, F. R., and Aref, H. (2004). Designing for chaos: applications of chaotic advection at the microscale. Philosophical Transactions of the Royal Society of London A: Mathematical, Physical and Engineering Sciences, 362(1818):1019–1036.

Tél, T., Károlyi, G., Péntek, A., Scheuring, I., Toroczkai, Z., Grebogi, C., and Kadtke, J. (2000). Chaotic advection, diffusion, and reactions in open flows. Chaos: An Interdisciplinary Journal of Nonlinear Science, 10(1):89–98.

Tél, T., Moura, A. d., Grebogi, C., and Károlyi, G. (2005). Chemical and biological activity in open flows: A dynamical system approach. Physics Reports, 413(2-3):91–196.

Trefry, M. G., Lester, D. R., Metcalfe, G., Ord, A., and Regenauer-Lieb, K. (2012). Toward enhanced subsurface intervention methods using chaotic advection. Journal of Contaminant Hydrology, 127(1-4):15–29.

Villermaux, E. (2012). Mixing by porous media. Comptes Rendus Mécanique, 340(11-12):933–943.

Villermaux, E. and Rehab, H. (2000). Mixing in coaxial jets. Journal of Fluid Mechanics, 425:161–185.

Weiss, J. B. and Provenzale, A. (2008). Transport and Mixing in Geophysical Flows. Springer-Verlag Berlin Heidelberg.

Werth, C. J., Cirpka, O. A., and Grathwohl, P. (2006). Enhanced mixing and reaction through flow focusing in heterogeneous porous media. Water Resources Research, 42(12):doi:10.1029/2005wr004511.

Ye, Y., Chiogna, G., Cirpka, O. A., Grathwohl, P., and Rolle, M. (2015). Enhancement of plume dilution in two-dimensional and three-dimensional porous media by flow focusing in high-permeability inclusions. Water Resources Research, 51(7):5582–5602.

Zhang, P., DeVries, S. L., Dathe, A., and Bagtzoglou, A. C. (2009). Enhanced mixing and plume containment in porous media under time-dependent oscillatory flow. <u>Environmental Science and Technology</u>, 43(16):6283–6288.